1996

Vuv Laser/time-of-flight Mass Spectroscopy: Valence To Ion-pair States Transitions Of Brcl And Cl(2)

Peng Wang

VUV Laser/Time-of-flight Mass spectroscopy: Valence to Ion-pair states transitions of BrCl and Cl_2

By

Peng Wang
Department of Chemistry

Submitted in Partial fulfillment
of the requirements for the degree of
Doctor of Philosophy

Faculty of Graduate Studies
The University of Western Ontario
London, Ontario
June 1996

ISBN 0-612-15088-7

Canada

Abstract

This thesis describes a newly built vacuum ultraviolet (VUV) laser/time-of-flight (TOF) mass spectrometer system in great detail. The theoretical background behind the techniques is also provided. Tunable, coherent, and monochromatic VUV "laser" radiation was generated by the nonlinear optical technique of two-photon resonantly enhanced four-wave difference-mixing (FWDM) in Kr gas. The frequency resolution of the recorded spectra is estimated to be ≤ 0.2 cm^{-1}. The mass resolution, m/Δm, of the linear TOF mass spectrometer ≥ 500, which was sufficient to obtain single isotopomer data.

With this instrument, vibrationally and rotationally resolved spectra of the $E0^+$ (v' = 173 - 203) ion-pair state $\leftarrow$ $X0^+$ (v'' = 0) ground state transition of jet-cooled BrCl near 145 nm was recorded and analyzed for the first time. J-numbering for all the rotationally resolved isotopomer bands were determined from ground state combination differences, and molecular constants were derived. The relative vibrational numbering of the isotopic features for BrCl was established by fitting the band origins and band heads to an appropriate mass-reduced Dunham expansion. The absolute vibrational numbering chosen was that which yielded a minimum standard deviation.

Mass-resolved spectra of the $2\,^1\Sigma_u^+$(v'= 1-3) $\leftarrow$ $X\,^1\Sigma_g^+$(v'' = 0) transition of jet-cooled Cl_2 between 78000 and 80100 cm^{-1} were also recorded and rotationally analyzed. Unambiguous isotopomer assignments for the numerous features associated with each vibrational band in this spectral region were made for the first time. Although the system appears to be perturbed, measured vibrational isotope shifts strongly support a change of + 1 in the accepted 2-state v' numbering.

To my mom and dad

Acknowledgments

It gives me great pleasure to acknowledge the help I have received during the past five years. First of all, I would like to give my sincere thanks to my research supervisor, Professor Robert H. Lipson, for his guidance, patience, and endless support throughout the years. I consider myself extremely fortunate to have Rob as my supervisor since I have learned so much from him and, without his generous aid, I could never reach this point.

I am very grateful to Dr. Stamen S. Dimov, who helped me tremendously whenever I had trouble with my experiments. He is so experienced, resourceful, and responsible. I am very lucky to have the chance to learn from such a great scientist.

A great deal of thanks is given to the group of people who work in the Machine Shop of Physics department for their technical help at early stage of my experiment. Also, I like to express my special thanks to Mr. John A. Vanstone, for building the Sequencer and many other "necessities" of my experiments.

I am incredibly thankful to Xiaokun Hu, Dunmir Mao, Hafed A. Bascal, and many other friends in this department, for the support I received whenever I needed. In addition, I like to give my thanks to the staff members in this department, for their assistance in many matters during my studying.

I would like to express my gratitude to Professor Jiyie Cai, for his assistance in recording the spectra of Cl_2.

Many thanks also go to Mrs. Tammy Lipson, for those beautiful drawings she made for this thesis.

Finally, I am greatly indebted to my husband, Dr. Qingyu Zhuang, and to my mother and father, for their everlasting love and encouragement.

TABLE OF CONTENTS

LIST OF TABLES

LIST OF FIGURES

Chapter 1

Introduction

1.1 Background of the thesis work

Molecular spectroscopy is one of the most important means of determining molecular structure. During the past two decades, the availability of high brightness excitation sources, such as tunable narrow band lasers and monochromatized synchrotron radiation, has advanced atomic and molecular spectroscopy into short wavelength regions at high resolution.

Completely, rotationally resolved molecular spectra, however, can not be obtained with synchrotron radiation except for perhaps the lightest molecules such as H_2 or hydrides. This has certainly been the case for BrCl and Cl_2, both of which have strong absorptions in the vacuum ultraviolet (VUV, 100 nm $\leq \lambda \leq$ 200 nm) region. With the development of nonlinear optical techniques such as four-wave frequency-mixing, tunable, coherent, and most importantly, monochromatic radiation covering the entire VUV and parts of extreme ultraviolet (XUV, $\lambda <$ 100 nm) region can be generated, and studies of heavier molecules at rotational resolution can be contemplated.

At room temperature, molecular spectra are usually congested due to the large number vibrational and rotational levels populated in their ground states, and the possible presence of naturally occurring isotopomers. Supersonic jet cooling, can reduce this source of complexity considerably, resulting in spectra which are amenable to detailed analysis.

Each isotopomer, however, has a different set of vibrational and rotational energy levels due to isotope effects. As a result, the vibrational bands belonging to different isotopomers can overlap with one another, making isotopomer identification difficult from the laser-induced fluorescence excitation spectra, especially if the transitions are perturbed. Although in principle this problem can be alleviated by using isotopically

enriched samples, the costs are prohibitive compared to the use of a time-of-flight (TOF) mass spectrometer. Detailed explanations of four-wave mixing, supersonic jets, and TOF mass spectrometry are given in Chapter 2.

The union of VUV/XUV laser sources, supersonic jet cooling, and TOF mass spectroscopic methods for this thesis project proved to be extremely powerful tool for dealing with isotopic samples such as BrCl and Cl_2. The complete experimental work is described in Chapter 3.

1.2 Orbitals and states of halogens and interhalogens

The UV and VUV absorption and fluorescence excitation spectra, and the corresponding dispersed emission spectra of the halogens and interhalogens are rich in structure. Spectral features are due to transitions between the ground state and higher energy Rydberg, ion-pair, and for the most part, repulsive electronically excited valence states [1]. All electronic states here will be denoted by those molecular orbital (MO) electron configurations possibly starting with two np^5 halogen atoms, n = 3, 4, 5 for Cl, Br, and I, respectively. The dominant MO configuration is given by $\sigma_g^m \pi_u^p \pi_g^{*q} \sigma_u^{*n}$ where $m + p + q + n = 10$. The g/u labels pertain only to the homonuclear species. Generally, the electron configurations are denoted by the values of the (m, p, q, n) sequence only for simplicity. For example, the ground state electron configuration is written as 2440 [2].

The excited states can be arranged into three groups: valence, Rydberg, and ion-pair, respectively, according to their dissociation products. Valence states correlate at dissociation with two ground state atoms having $^2P_j^o$ configurations, J = 1/2 and/or 3/2. Here the $^2P_{3/2}^o$ and $^2P_{1/2}^o$ ground state levels are spin-orbit split (882 cm^{-1} for Cl, 3685 cm^{-1} for Br, 7603 cm^{-1} for I_2, Ref. 3). Rydberg states dissociate to one ground state atom and one electronically excited atom, while ion-pair states produce two oppositely charged ions at dissociation. Typically the dissociation limits of the states in order of increasing energy are valence < Rydberg < ion-pair.

There are a total of 23 near Hund's case (c) valence states for the halogens and

interhalogens. The difference in state labeling for the halogens and interhalogens is that for the former the g/u parity designations are required whereas for the latter, they are not. The distribution of the valence states for an XY molecule is as following, $^2P^o_{1/2} + {}^2P^o_{1/2}$ (3 states), $^2P^o_{1/2} + {}^2P^o_{3/2}$ (5 states), $^2P^o_{3/2} + {}^2P^o_{1/2}$ (5 states), and $^2P^o_{3/2} + {}^2P^o_{3/2}$ (10 states), whereas for an X_2 species, they are, $^2P^o_{1/2} + {}^2P^o_{1/2}$ (3 states), $^2P^o_{3/2} + {}^2P^o_{1/2}$ (10 states), and $^2P^o_{3/2} + {}^2P^o_{3/2}$ (10 states). Qualitatively, the valence states account for all states having electron configurations 2440, 2431, 2341, and 2422.

The dominant MO nature of the ion-pair states is antibonding, as evidenced by the electron configurations 1441, 2332, 1432, and so on. Due to the strong Coulombic interaction governing the interaction between oppositely charged ions, the outer wing is approximately described by a 1/R potential, while the inner wing is determined by the steep rise in electronic antibonding. A more detailed description for the potential function is provided by the "truncated-Rittner" function [4]:

$$V(r) = D + A \exp(-br) - e^2/r - C_3/r^3 - C_4/r^4 - C_6/r^6 - \ldots \qquad (1.1)$$

where D is the dissociation energy, the second term accounts for the repulsion of two electron clouds at a small nuclear separation r (A and b are constants), and $\{C_n\}$ are the long-range coefficients. Typically, the long-range terms cancel the repulsion term which leads to a dissociation energy, $D_e = D - V(r_e)$, is approximately equal to e^2/r_e. Consequently, the dissociation energies for states with the same r_e are nearly constant.

Ion-pair states tend to arrange themselves in tiers, where each tier is composed of states of approximately the same T_e, which extrapolate at dissociation to the same state of $X^+ (+ Y^- ({}^1S_0))$ as follows (if ionization potential (IP) (X) ≤ IP (Y)) [2]:

Dissociation Limit			Molecular States	Tier
	Y^-	X^+		
	...	...		
↑	$^1S_0$	$^1S_0$	$\Omega = 0^+_{g/u}$	4
E	$^1S_0$	$^1D_2$	$\Omega = 2_{g/u}, 1_{g/u}, 0^+_{g/u}$	3
|	$^1S_0$	$^3P_{1,0}$	$\Omega = 1_{g/u}\, 0^-_{g/u}, 0^+_{g/u}$	2
	$^1S_0$	$^3P_2$	$\Omega = 2_{g/u}, 1_{g/u}, 0^+_{g/u}$	1

Here, Ω corresponds to the component of total angular momentum along the bond axis, and again, the parity labels are only important when X = Y. There are a total of 20 possible states in this category for a symmetrical halogen. The same total number of ion-pair states exist for the interhalogens, except that 10 of them dissociate to the higher energy $Y^+ + X^-$ set of limits. These latter states of the interhalogens remain virtually unknown.

Experimentally, this tiered arrangement simplifies the search for unknown states enormously on the basis of energy. In practice, the $^3P_0$ and $^3P_1$ states of the halogen cations are never far apart energetically. Therefore, it is convenient to group these ion-pair states derived from the two asymptotes together into one (the second tier).

The strongest ground state to ion-pair state transitions for the I and Br containing interhalogen spectra are the $\sigma^* \leftarrow \sigma$ type involving the first tier. It was demonstrated by R. N. Zare and D. R. Herschbach [5] using a charge transfer model that the valence to ion-pair state transition moments are large for parallel transitions ($\Delta\Omega = 0$), while perpendicular transitions ($\Delta\Omega = \pm 1$) are weak. This explains the overriding propensity for $\Delta\Omega = 0$ transitions observed in halogen and interhalogen spectra, even though the single-photon selection rule states that $\Delta\Omega = \pm 1$ are allowed.

Historically, the state names for the ion-pair states have been confusing. For I and Br containing interhalogens, the strongest transition is to $E0^+$ of the first tier, while for I_2 and Br_2 is the ion-pair state $D0^+_u$. Unfortunately, Cl_2 remains an exception both in its state names and by the fact that the strongest ground state to ion-pair state transition involves a third tier excited level.

Diatomic halogen and interhalogen molecules have attracted a great deal of interest for their importance in photochemical systems, their use in rare-gas halide lasers, and their potential value as laser media in their own right. Consequently, their low- and higher-lying electronic states need to be well-characterized [6, 7]. In this work, the $E0^+$ state of BrCl and the $2^1\Sigma^+_u$ state of Cl_2 were chosen for detailed studies.

1.3 The $E0^+$ State of BrCl

Although BrCl is one of the less well-documented unsymmetrical halogens, its electronic structure was expected to follow the pattern now well established for the iodine containing molecules. The first investigation on bromine monochloride was made by Cordes and Sponer [8]. Despite the fact that a number of spectroscopic and kinetic studies on this molecule soon followed [9-13], the electronic structure of BrCl is only known in fragments. J. A. Coxon photographed 24 bands of the $B^3\Pi\ (0^+) \leftarrow X^1\Sigma^+$ system of $^{79}Br^{35}Cl$ and $^{81}Br^{35}Cl$ at high resolution [14], from which rotational and vibrational molecular constants for excited B state and ground state were derived. The He I photoelectron spectrum of BrCl has also been recorded, and the spin-orbit splitting for the ground state of $BrCl^+$ was determined to be $2070 \pm 30\ cm^{-1}$ [15]. BrCl emission spectra have been obtained in the wavelength range between 140 - 400 nm [10, 16]. The $D'2 \rightarrow A'2$ and $E0^+ \rightarrow B0^+$ systems have been analyzed [17, 18].

More importantly with respect to this thesis is that limited work has been done on the VUV spectroscopy of BrCl. Most of what is known has been obtained from low resolution fluorescence excitation spectra recorded using synchrotron radiation [16, 19]. The strongest VUV absorption from the $X0^+$ ground state involves a transition to the first tier, which contains the triad of ion-pair states $E0^+$, $\beta 1$ and $D'2$. As noted above, the strong $\Delta\Omega = 0$ "propensity rule" limits the strongest absorption to $E0^+$ [2, 5]. Near 145 nm, VUV absorption spectra are dominated by both Rydberg state $\leftarrow$ ground state transitions and the E - X band system. In fluorescence excitation, however, only the ion-pair state absorption is apparent, presumably because the Rydberg states are strongly predissociated. Despite the fact that the ion-pair absorption was not vibrationally resolved, its overall intensity appeared strongly modulated as a function of excitation frequency. This observation has been attributed to interactions between $E0^+$ and isoenergetic Rydberg states [16, 19]. Although the synchrotron work was useful for providing a spectral overview, the resultant interpretation of the ion-pair spectrum was actually based on theoretical expectations, and not on direct spectroscopic analysis.

Four naturally occurring isotopomers exist for BrCl: $^{79}Br^{35}Cl$, $^{81}Br^{35}Cl$, $^{79}Br^{37}Cl$, and $^{81}Br^{37}Cl$. The relative intensity of each isotopomer band in a fluorescence excitation spectrum is expected to reflect the normalized natural abundance ratios: $^{79}Br^{35}Cl$:$^{81}Br^{35}Cl$: $^{79}Br^{37}Cl$:$^{81}Br^{37}Cl$ = 1.00:0.97:0.32:0.31 [20]. However, early VUV laser fluorescence excitation spectra of jet-cooled BrCl recorded in our lab before the time-of-flight mass spectrometer was built showed this was not the case [21] even though rotationally resolved vibronic bands were obtained at that time. The isotopomer identity for each feature was uncertain due to the strong intensity perturbations which made assignments nearly impossible on the basis of natural isotopomer abundances above. However, that problem was easily solved by employing the VUV laser/TOF methods described in Chapter 3 of this thesis.

The electronic configuration of the $E0^+$ ion-pair state is 1441. Quantitative data about this excited ion-pair state has only become available recently. Tellinghuisen and co-workers recorded emission spectra of the $E0^+ \rightarrow B0^+$ band system by exciting $^{81}Br^{37}Cl$ isotopomer samples in a mild Tesla discharge [18]. The E-state equilibrium bond length was found to be 3.042 Å based on a deperturbation analysis involving β1 [22]. Due to the strong antibonding character associated with a $\sigma \leftrightarrow \sigma^*$ transition, the excited state equilibrium bond length is substantially longer than that for $X0^+$ ($\Delta r_e = r'_e - r''_e \approx 0.64$ Å), and its vibrational and rotational constants are smaller. On the other hand, the $E0^+$ state dissociation energy is much larger than that for the ground state due to the strong Coulombic interaction binding the ion-pair together at long range [23]. As a result, VUV transitions from the lowest vibrational level of $X0^+$ are expected to probe the inner wall of the $E0^+$ potential energy curve, exciting high, closely spaced vibrational states. The relevant potential energy curves for this work are shown schematically in Fig. 1.1.

A. Kvaran *et al* have modeled the E state potential energy curve using a Rittner potential [19] based on spectroscopic parameters derived from low resolution synchrotron spectra obtained by Chakraborty *et al* [18]:

$$U_E(r) = 3.3930 \times 10^7 \exp(-r/0.339606) - 116900/r + 82820/\text{cm}^{-1}, \qquad (1.2)$$

where $r_e = 3.05$ Å, $T_e = 48758.8\ \text{cm}^{-1}$, $\omega_e \approx 197.5\ \text{cm}^{-1}$.

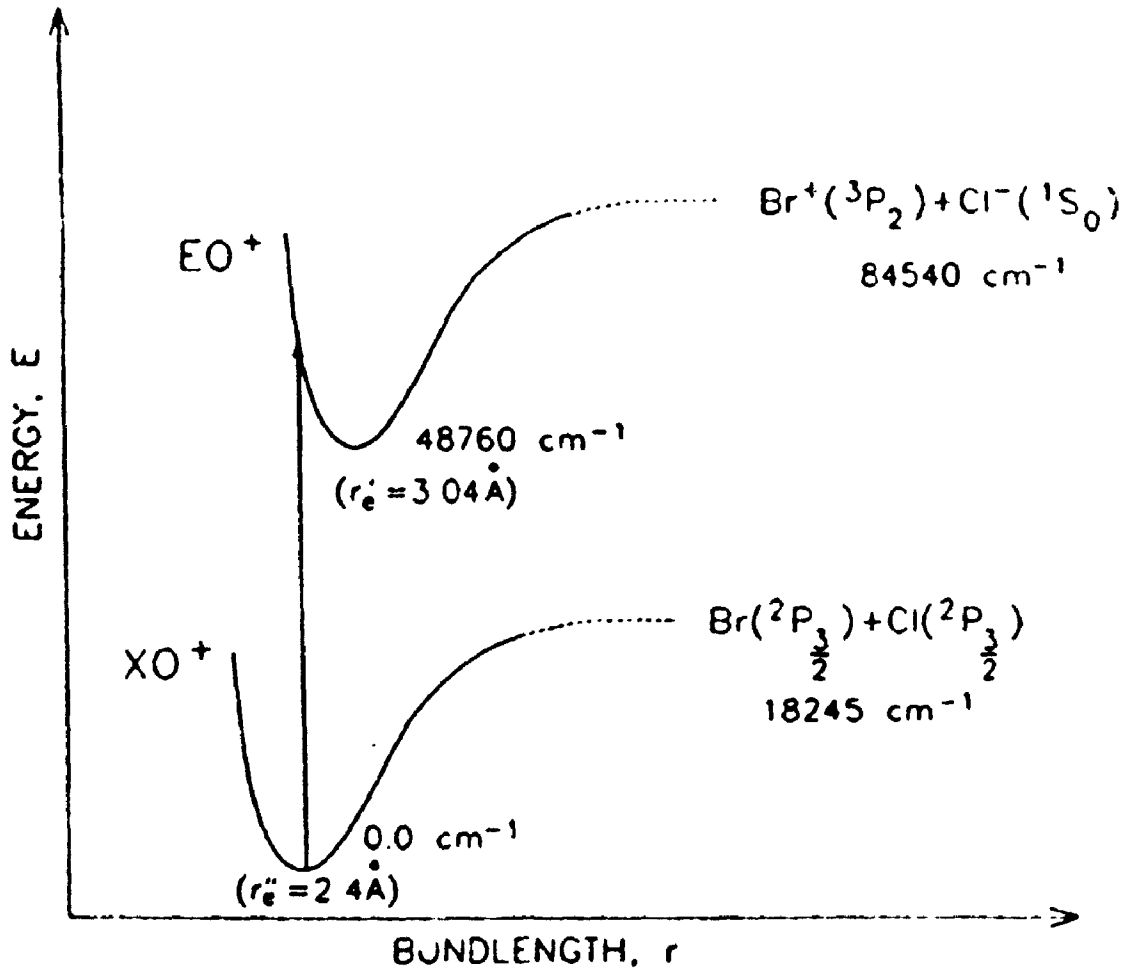

Fig. 1.1. A schematic of the potential energy curves of BrCl relevant to this work Dissociation products, potential minima, and dissociation limits [referenced to the bottom of the electronic ground state (in cm^{-1})], and equilibrium bond lengths (in Ångstrom units) are indicated

In this work, the vibrationally and rotationally resolved spectra of the $E0^+$ ion-pair state $\leftarrow X0^+$ ground state transition of jet-cooled BrCl near 145 nm were recorded for the first time. A complete rotational and vibrational analysis of the spectra observed can be found in Chapter 4.

1.4 The $2^1\Sigma_u^+$ State of Cl_2

The electronic structure of elemental chlorine has received a great deal of attention recently. Cl_2 plays a significant role in rare-gas monohalide laser systems and may even be a candidate on its own for high-power lasers [24]. The absorption spectrum of Cl_2 in the vacuum ultraviolet was first investigated by Lee and Walsh using a low dispersion spectrograph [25]. The vibrational structure evident in their spectra indicated the existence of bound excited states, and an intense but irregularly spaced band system below 145 nm was observed. Early dispersed VUV fluorescence studies provided only a precise determination of the ground state [26, 27]. This disappointing situation was partly due to experimental difficulties of working in the VUV region. Of course, additional complexity was due to the existence of three naturally occurring Cl_2 isotopomers, having a normalized abundance ratio of $^{35}Cl_2$:$^{35}Cl^{37}Cl$:$^{37}Cl_2 \approx 1$:0.64:0.10 [20].

More recently, high resolution spectroscopic studies by Le Calvé *et al* [28] and Douglas [29] have improved our knowledge considerably. Douglas was able to rotationally analyze 43 bands of isotopicallly pure $^{35}Cl_2$ photographed in absorption between 133 and 145 nm. These were assigned to an ionic state dissociating to $Cl^+ + Cl^-$. However, he was unable to provide a convincing vibrational analysis due to extensive perturbations.

For Cl_2, the ion-pair block lies above the valence states and penetrates the range of Rydberg states. The large well depth characteristic of all ion-pair states due to strong Coulombic interaction at long range pulls their electronic origins, T_e, below that of less strongly bound Rydberg states. This results in strong avoided crossings between the ion-pair and Rydberg potential energy curves. However, the true nature of the perturbed

excited states was not revealed until the advent of the *ab initio* calculations by Peyerimhoff and Buenker [30]. They showed that strong Rydberg-valence configuration mixing leads to avoided crossings between the excited state potential energy curves, resulting in double-well potentials with irregular vibrational progressions which cannot be analyzed in a simple way. It was deduced that the excited state studied by Douglas was a third tier $^1\Sigma_u^+$ ion-pair valence state ($\sigma_g \rightarrow \sigma_u$, electron configuration 1441) which dissociates to Cl^+ (^1D_g) + Cl^- (^1S_g). They predicted that strong interactions between this ionic state and the near isoenergetic $\pi_g \rightarrow 4p\pi$ ($^1\Sigma_u^+$) Rydberg state, produced a double-well potential energy curve which they labelled $1\,^1\Sigma_u^+$ (Fig. 2, Ref. 30). Some of the strongest features in the VUV spectrum of Cl_2 involve transitions to the ion-pair portion of the $1\,^1\Sigma_u^+$ state.

A detailed investigation of $1\,^1\Sigma_u^+$ in absorption, fluorescence excitation, and dispersed emission has been made using synchrotron radiation [31-33]. Although the spectra were not rotationally resolved, the shape and the position of the double-well was refined by modeling the bound-free emission profiles excited in the molecule, and by Franck-Condon calculations. The Rydberg portion of the double-well potential energy curve has been studied by our group and others using VUV laser/TOF methods [34, 35]. Consequently, at this time, the $1\,^1\Sigma_u^+$ state of Cl_2 is well characterized.

The higher-lying $2\,^1\Sigma_u^+$ excited state is also predicted to have double minima (Figs. 1.2 and 1.3). In the diabatic picture, the inner wing of the 2-state belongs to the third tier ion-pair state involved in the formation of the $1\,^1\Sigma_u^+$ state, while the outer wing belongs to the $4p\pi$ Rydberg state. As a consequence, the equilibrium internuclear separation of the 2-state is expected to be approximately equal to that associated with the top of the hump separating the Rydberg and ion-pair portions of the 1-state potential curve (~ 2.1 Å). Diabatically, double-well formation for the 2-state occurs at longer bond lengths (~ 2.4 Å), and is a result of an additional avoided crossing between the outer wing of the $4p\pi$ Rydberg state and the inner wing of a fourth tier ion-pair state ($\pi_u\pi_g$

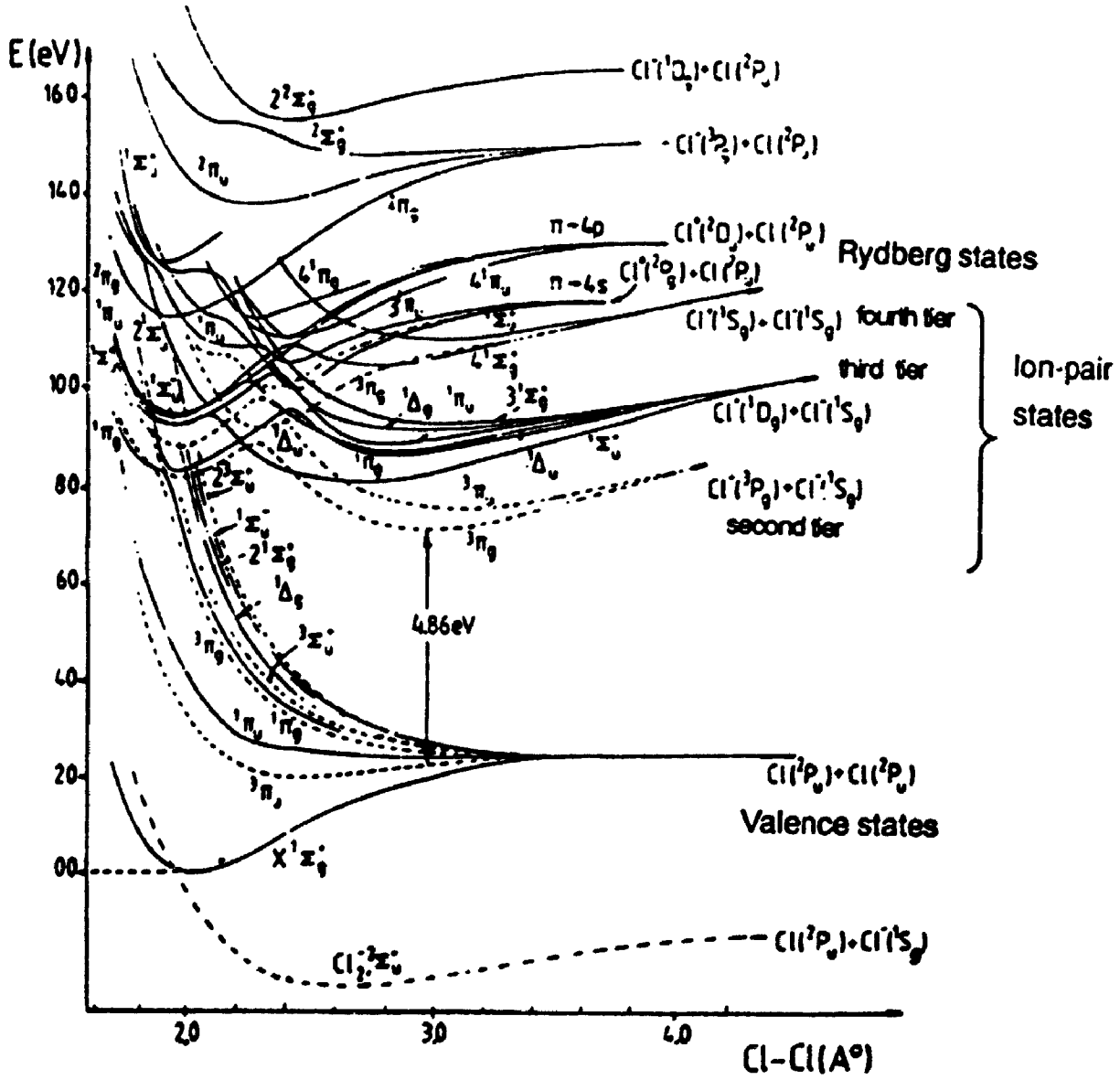

Fig. 1.2. The potential energy curves of most states of Cl_2 treated by the *ab initio* calculation [30].

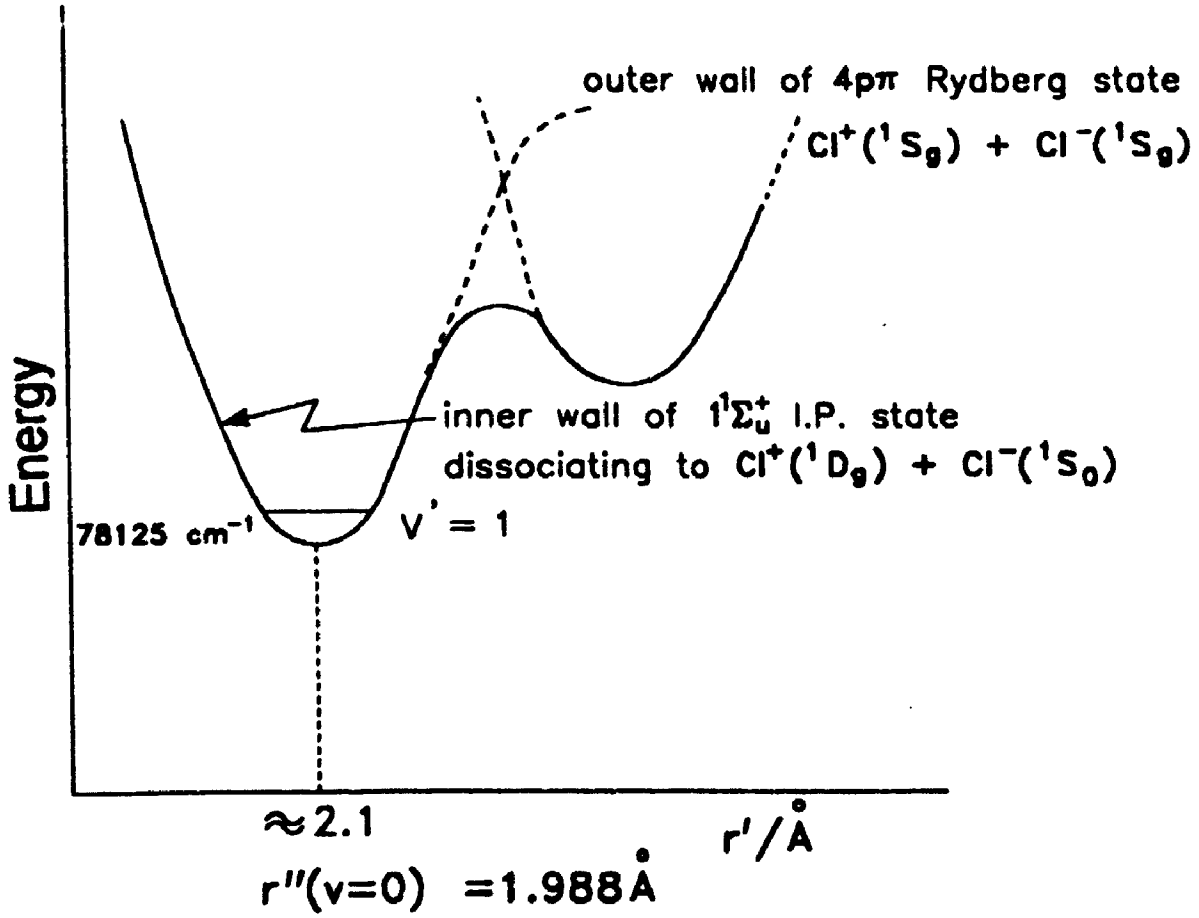

Fig. 1.3. Schematic of the excited $2\,^1\Sigma_u^+$ state potential energy curve of Cl_2 whose Rydberg well is a result of a strong adiabatic interaction between the 4pπ Rydberg state and a third tier ion-pair state dissociating to Cl^+ (^1D_g) + Cl^- (^1S_g). Double-well formation is due to an additional avoided crossing between the outer wing of the 4pπ Rydberg state and a fourth tier ion-pair state dissociating to Cl^+ (^1S_g) + Cl^- (^1S_g). The noted frequency (in cm^{-1}) is the approximate transition wavenumber for what has now been reassigned to the (1, 0) band of the 2-X band system.

$\rightarrow\sigma_u^2$, electron configuration 2332) dissociating to Cl^+ (^1S_g) + Cl^- (^1S_g) [36]. The 2-X spectrum has been studied before. The absorption spectrum in the 107 - 130 nm region was first photographed by Douglas [29] who presented rough frequency measurements for a number of complex red-shaded bands between 78138 and 81763 cm^{-1}, but no analysis was offered. Later, Moeller *et al* studied the absorption spectrum of Cl_2 in the 120 - 140 nm region using synchrotron radiation [31]. They made vibrational and isotopic assignments and estimated the vibrational frequency, $\omega_e \approx 1040$ cm^{-1}, and first anharmonicity constant, $\omega_e x_e \approx 42$ cm^{-1}, for the excited 2-state. The strong feature at 78135 cm^{-1} was taken to be the (v', v'') = (0, 0) transition since that agreed well with theoretical prediction which placed (0, 0) at 78250 cm^{-1} [30]. On the other hand, attention should be paid to the accuracy of the calculations which was stated to be only in the 0.1 - 0.2 eV range, corresponding to an ~ 800 - 1600 cm^{-1} uncertainty. Nevertheless, that has remained the accepted vibrational numbering until this work.

Lee *et al.* extended the VUV spectroscopic studies to even shorter wavelengths by synchrotron light [37]. They identified vibrational levels of excited 2-state up to v' = 15 in fluorescence excitation. Their (0, 0) band was assigned to a feature at 78119 cm^{-1}, which is consistent with the previous determination of Moeller *et al* [31]. As well, the fluorescence yield for the 2-state was found to be less than unity indicating that the 2-state is partially dissociative.

Recently, Tsukiyama and co-workers recorded fluorescence excitation spectra of bands they assigned to the 2-X (v', v") = (1, 0) and (2, 0) bands by exciting jet-cooled Cl_2 with a tunable VUV light source generated by four-wave sum mixing in Hg vapor [35]. Fluorescence lifetime measurements for 16 bands between 78993.4 and 80089.2 cm^{-1} were tabulated. Features with lifetimes in the 3 ns range were ascribed to the $2^1\Sigma_u^+ \leftarrow X^1\Sigma_g^+$ transition, and some isotopic identities were suggested. Bands with lifetime longer than 10 ns were tentatively assigned to members of the $2^3\Pi_u \leftarrow X^1\Sigma_g^+$ band system.

For this thesis, single isotopomer spectra of the $2^1\Sigma_u^+$ (v') $\leftarrow X^1\Sigma_g^+$ (v'' = 0) transition of Cl_2 were recorded between ~ 78000 and 80100 cm^{-1} using a VUV laser/TOF

mass spectrometer. Isotopomer assignments for numerous features associated with each vibrational band in this spectral region have been established unambiguously for the first time. Measured vibrational isotope shifts strongly support a change of +1 in the accepted 2-state vibrational numbering. The results of the first rotational analysis of the 2-state spectra are also presented in Chapter 4.

1.5 References

[1]. R. S. Mulliken, *J. Chem. Phys.*, **55**, 288 (1971).

[2]. J. C. D. Brand and A. R. Hoy, *Appl. Spectrosc. Rev.*, **23**, 285 (1987).

[3]. C. Moore, *Natl. Bur. Std.*, (US) **3**, Circ. No. 467 (1958).

[4]. P. Brumer and M. Karplus, *J. Chem. Phys.*, **58**, 3903 (1973).

[5]. R. N. Zare and D. R. Herschbach, *J. Mol. Spectrosc.*, **15**, 462 (1965).

[6]. Ch. A. Brau, **Excimer Lasers**, 2nd ed. (Ch. K. Rhodes, ed.), Springer, Berlin, 1984, J. Tellinghuisen, **Applied Atomic Collision Physics**, Vol. 3 (H. S. Massey, E. W. McDaniel, and W. L. Nighau, eds.), Academic, New York, 1982.

[7]. M. J. Shaw, C. B. Edwards, F. O'Neill, C. Fotakis, and R. J. Donovan, *Appl. Phys. Lett.*, **37**, 346 (1980).

[8]. H. Cordes and H. Sponer, *Z. Physik*, **79**, 170 (1932).

[9]. J. A. Coxon, *Chemical Society Special Report on Molecular Spectroscopy*, Vol. 1, Chemical Society, London, 177 (1972).

[10]. M. A. A. Clyne and H. W. Cruse, *J. Chem. Soc. Faraday Trans. II*, **68**, 1377 (1972); P. B. V. Haranath and P. T. Rao, *Indian J. Phys.*, **31**, 368 (1957).

[11]. M. A. A. Clyne and J. *A. Coxon, J. Phys. B.* **3**, L9 (1970); M. A. A. Clyne and J. A. Coxon, *Proc. Roy. Soc., Ser. A*, **298**, 424 (1967).

[12]. W. Holzer, W. F. Murphy, and H. J. Bernstein, *J. Chem. Phys.*, **52**, 399 (1970).

[13]. R. J. Donovan and D. Husain, *Trans. Faraday Soc.*, **64**, 2325 (1968).

[14]. J. A. Coxon, *J. Mol. Spectrosc.* **50**, 142 (1974).

[15]. S. J. Dunlavey, J. M. Dyke, and A. Morris, *J. Electron. Spectrosc. Relat. Phenom.*, **12**, 259 (1977).

[16]. A. Hopkirk, D. Shaw, R. J. Donovan, K. P. Lawley, and A. J. Yencha, *J. Phys. Chem.*, **93**, 7338 (1989).

[17]. M. Diegelmann, K. Hohla, F. Regentrost, and K. L. Kompa, *J. Chem. Phys.*, **76**, 1233 (1982).

[18]. D. K. Chakraborty, P. C. Tellinghuisen, and J. Tellinghuisen, *Chem. Phys. Lett.*, **141**, 36, (1987).

[19]. A. Kvaran, A. J. Yencha, K. P. Lawley, and R. J. Donovan, *Mol. Phys.*, **75**, 197 (1992).

[20]. P. Debiévre, M. Gallent, N. E. Holden, and I. L. Barnes, *J. Phys. Chem.* Ref. Data **13**, 809 (1984).

[21]. R. H. Lipson, N. A. McDonald, and A. R. Hoy, unpublished results.

[22]. S. W. Brown, C. J. Dowd, Jr. and J. Tellinghuisen, *J. Mol. Spectrosc.*, **132**, 178 (1988).

[23]. J. Tellinghuisen, *J. Chem. Phys.*, **89**, 6150 (1988).

[24]. C. H. Chen and M. G. Payne, *Appl. Phys. Lett.*, **28**, 219 (1976).

[25]. J. Lee and A. D. Walsh, *Trans. Faraday Soc.* **55**, 1281 (1959).

[26]. R. H. Asundi and P. Venkateswarlu, *Indian J. Phys.* **21**, 76 (1947).

[27]. A. E. Douglas and A. R. Hoy, *Can. J. Phys.*, **53**, 1965 (1975).

[28]. J. Le Calvé, M. C. Castex, E. Boursey, and Y. Le Duff, *European Conference on Atomic Physics*, Heidelberg, EPS Abstracts **5 A**, Part I, 319 (1981).

[29]. A. E. Douglas, *Can. J. Phys.*, **59**, 835 (1981).

[30]. S. D. Peyerimhoff, R. J. Buenker, *Chem. Phys.*, **57**, 279 (1981).

[31]. T. Moeller, B. Jordan, P. Gürtler, G. Zimmerer, D. Haaks, J. LeCalvé, and M. C. Castex, *Chem. Phys.*, **76**, 295 (1983).

[32]. T. Moeller, B. Jordan, P. Gürtler, D. Haaks, J. LeCalvé, and M C. Castex, *Spectral Line Shapes* **2**, 597 (1983).

[33]. J. Wörmer, T. Möller, J. Stapelfeldt, G. Zimmerer, D. Haaks, S. Kampf, J. LeCalvé, and M. C. Castex, *Z. Physik D* **7**, 383 (1988).

[34]. P. Wang, I. V. Okuda, S. S. Dimov, and R. H. Lipson, *Chem. Phys. Lett.*, **229**, 370 (1994).

[35]. K. Tsukiyama, Y. Kurematsu, M. Tsukakoshi, A. Misu, T. Kasuya, *Chem. Phys. Lett.*, **152**, 523 (1988).

[36]. J. Wörmer, T. Möller, G. Zimmerer, J. Le Calvé, and M. C. Castex, *Chem. Phys. Lett.*, **170**, 419 (1990).

[37]. L. C. Lee, M. Suto, K. Y. Tang, *J. Chem. Phys.*, **84**, 5277 (1986).

Chapter 2

Theoretical Background

In this chapter, an overview of the general principles of the nonlinear optical technique of four-wave mixing, supersonic jet cooling, and linear time-of-flight mass spectrometry are given. Selected aspects of spectroscopy are also presented with emphasis on electronic transition selection rules.

2.1 Four-wave Frequency Mixing

With the rapid development of laser technology, continuously tunable, coherent, and monochromatic radiation is now commercially available from the near infrared to the ultraviolet. However, vacuum ultraviolet (VUV) lasers with outputs between 100nm - 200nm have not been developed and, yet would be of great value for the type of work described in this thesis. A general solution to this problem is to generate coherent VUV light by third-harmonic generation or frequency mixing in gaseous nonlinear media. Nonlinear gases are required for VUV generation because almost all solids become opaque in that spectral region. Four-wave frequency mixing, in particular, is a powerful technique for extending high resolution laser spectroscopy into the VUV, and part of extreme ultraviolet (XUV) region (λ < 100nm) as well, where many atoms and molecules have some of their most prominent absorption features. In my work, two-photon resonantly enhanced four-wave difference mixing in Kr gas was used to generate the wavelengths necessary to excite ground state to ion-pair state transitions of BrCl and Cl_2.

Historically, it was the initial observation of second harmonic generation (SHG) in noncentrosymmetric crystals by Franken et al in 1961 [1] that ultimately led to coherent VUV light generation by four-wave mixing. Their work was soon followed by the

demonstration of third harmonic generation (THG) in 1964 [2] by Maker et al who used glasses, and liquids as well as crystals as nonlinear media. As noted above, the major challenge of extending this result to the VUV region was the limited transparency of many nonlinear solids in this spectral region. This difficulty was overcome by New and Ward who successfully produced third harmonic generation light using a number of gases as nonlinear media [3]. In 1971 Harris and Miles [4] were able to obtain large harmonic outputs by using phase-matched metal vapors as the nonlinear media, and by the technique of resonance enhancement [5]. The four-wave mixing technique, first introduced by Hodgson, Sorokin and Wynne in 1974 [6], and used extensively in this thesis, is described below.

The name "four-wave mixing" is appropriate because there are a total of four waves involved in the nonlinear optical process. Three of these are input waves, while the fourth is the resultant output. Experimentally, only two fundamental electromagnetic waves in the scheme, hereafter called ω_1 and ω_2, are used. The frequency of the generated VUV light can either be $2\omega_1 + \omega_2$ (four-wave *sum*-mixing), or $2\omega_1 - \omega_2$ (four-wave *difference*-mixing). Third harmonic light at $3\omega_1$ is also possible in the process, but under our experimental conditions it has a fixed frequency which makes it a less attractive source for spectroscopy.

Coherent generation is based on the nonlinear response of materials to intense electromagnetic fields such as strong lasers. The process of frequency mixing is best understood by considering the nonlinear susceptibility of an atomic medium.

If matter is exposed to an electric field, the bound electrons of the atoms or molecules are displaced from their equilibrium positions under the influence of the applied electric field, giving rise to a net polarization in the medium. For small electric fields E, the polarization P of any material can be expressed by the following well-known linear relationship [7]:

$$P = N\chi^{(1)}E \qquad (2.1)$$

where N is the number density of atoms or molecules, and the proportionality constant, $\chi^{(1)}$, is the complex linear susceptibility

$$\chi^{(1)} = \bar{\chi}^{(1)} + i\,\tilde{\chi}^{(1)} = \frac{1}{\hbar}\sum_{a}\frac{|\mu_{ag}|^2}{(\Omega_{ag} - \omega)}, \tag{2.2}$$

where μ_{ag} is the electric dipole matrix element for the transition between state $|g\rangle$ and state $|a\rangle$. The denominator in Eq. 2.2,

$$\Omega_{ag} = \omega_{ag} - i\Gamma_{ag} \tag{2.3}$$

is the corresponding complex transition frequency containing the damping constant Γ_{ag} which results in a finite linewidth for the transition. It should be noted that the real part of the linear susceptibility gives the refractive index n according to

$$1 + 4\pi N\,\bar{\chi}^{(1)} = \varepsilon_r = n^2 \tag{2.4}$$

whereas the imaginary part defines the absorption coefficient κ according to

$$4\pi N\tilde{\chi}^{(1)} = \varepsilon_i = \frac{cn\kappa}{\omega} \tag{2.5}$$

For strong laser fields, however, the linear relation 2.1 no longer holds, and higher-order terms for P which are nonlinear in E become significant. The corresponding polarization can be expressed as a power series expansion [8]

$$P = N(\chi^{(1)}\cdot E + \chi^{(2)}:EE + \chi^{(3)}\vdots EEE + \cdots) = \sum_{n=1}^{\infty} P^{(n)} \tag{2.6}$$

where $\chi^{(1)}$ again is the linear susceptibility, while $\chi^{(n)}, n \geq 2$ are the n-th order nonlinear susceptibilities of the medium. The higher order terms clearly become more significant with increasing electric field strength. In a definition sense any medium which obeys Eq. 2.6 is termed a "nonlinear medium" [9]. When there are only a finite number of frequency components (ω_j) in the incident radiation, the electric field $E(r, t)$ can be written as a Fourier sum

$$E(r, t) = \frac{1}{2}\sum_{j}\ [E^{\omega_j}(r)e^{-i\omega_j t} + E^{\omega_j^*}(r)e^{i\omega_j t}]. \tag{2.7}$$

The induced polarization $P(r)$ in the medium is also time-dependent, and can be expressed as

$$P(r,t)=\frac{1}{2}\sum_{j}\left[P^{(\omega_j)}(r)e^{-i\omega_j t}+P^{(\omega_j)^*}(r)e^{i\omega_j t}\right]. \tag{2.8}$$

In the relation 2.6, electric field product E^n can involve a single ω_j component, or can be a result of the interaction of individual fields with different frequencies. The latter scenario is the case of four-wave mixing.

The n-th order induced polarization, $P^{(n)}$, in Eq. 2.6 can be shown to be

$$P_{\alpha_s}^{(n)}(r,\omega_s)=\frac{n!N}{2^{n-1}}\sum_{\alpha_1\cdots\alpha_n}\chi^{(n)}_{\alpha_s\alpha_1\cdots\alpha_n}(-\omega_s;\omega_1\cdots\omega_n)\times E_{\alpha_1}(r,\omega_1)\cdots E_{\alpha_n}(r,\omega_n), \tag{2.9}$$

where N is the number density of atoms or molecules in the medium. The factor n! accounts for the number of intrinsic permutations possible for $P^{(n)}$ if all input frequencies $\omega_1,\omega_2\cdots\omega_s$ are nonzero and different, and the indices $\alpha_1,\alpha_2\cdots\alpha_s$ in the summation refer to the three Cartesian coordinates: x, y, and z.

Nonlinear optical susceptibility tensors $\chi^{(n)}$, defined by the equation 2.9, are the key quantities in nonlinear optics since they characterize the nonlinear response of the medium to the strong electromagnetic fields. In general, by using a quantum mechanical description for the medium, an expression for the n-th order nonlinear susceptibility can be derived:

$$\chi^{(n)}(-\omega_s;\omega_1\cdots\omega_n)$$
$$=\frac{\hat{P}_T}{n!\hbar}\sum_{gb_1\cdots b_n}\partial(g)\frac{\langle g|e_s\mu|b_1\rangle\langle b_1|e_1\mu|b_2\rangle\cdots\langle b_n|e_n\mu|g\rangle}{(\Omega_{b_1g}-\omega_1-\cdots-\omega_n)(\Omega_{b_2g}-\omega_2-\cdots-\omega_n)\cdots(\Omega_{b_ng}-\omega_n)}. \tag{2.10}$$

The summation in Eq. 2.10 is over all atomic or molecular states $b_1,b_2\cdots b_n$, and the permutation operator $\hat{P}_T$ requires the sum to be taken over all possible permutations of the n+1 interacting waves specified by the individual directions of the electric field vectors e_k and associated frequencies ω_k. The factor $\partial(g)$ implies that a weighted average for $\chi^{(n)}$ is required if there is an equilibrium distribution of initial states. For a single atomic ground state level, $\partial(g)$ can be ignored.

The susceptibility, $\chi^{(2)}$, is responsible for the lowest order nonlinear effect, SHG. However, $\chi^{(2)}$ is identically zero for isotropic media such as gases. Consequently, the

leading term which can lead to nonlinear effects in gases, including four-wave mixing, involves the third-order nonlinear susceptibility $\chi^{(3)}$.

There are many possible four-wave mixing processes which can be considered. The scheme employed in this thesis, and illustrated in Fig. 2.1, is two-photon resonantly enhanced four-wave difference mixing. Here, the two fundamental beams at angular frequencies ω_1 and ω_2 are used to produce resultant wave ω_4 at frequency $2\omega_1-\omega_2$. This is accomplished by tuning ω_1 to a two-photon allowed transition in the medium, while ω_2 is freely variable. In this case, the dominant term of $\chi^{(3)}$ reduces to

$$\chi^{(3)}(2\omega_1-\omega_2;\omega_1\omega_1-\omega_2) = \hbar^{-3}\sum_{abc}\frac{\langle g|e_4\mu|a\rangle\langle a|e_1\mu|b\rangle\langle b|e_2\mu|c\rangle\langle c|e_3\mu|g\rangle}{(\Omega_{ag}-\omega_1)(\Omega_{bg}-2\omega_1)(\Omega_{cg}-2\omega_1+\omega_2)} \qquad (2.11)$$

where e_i is the unit vector identifying the polarization of wavevector k, and μ is the electric dipole moment operator. The nonlinear susceptibility $\chi^{(3)}$ in equation 2.11, can be made larger by minimizing the denominator. In principle, this resonance enhancement can be achieved by tuning the incident radiation frequencies, ω_1 and ω_2, to either a one-, two-, or VUV allowed transition Ω_{ag}, Ω_{bg}, or Ω_{cg}, respectively, in the medium. A single photon allowed resonance enhancement is almost never chosen since it can also lead to strong linear absorption of the fundamental wave, which is a loss mechanism for VUV generation. While the VUV output could also produce additional enhancement, primarily through autoionization structure, often the VUV energies generated are in resonance with the continuum associated above the ionization limit for single-photon allowed transitions. There the oscillator strength is so small at the given frequency that the enhancement effect is negligible. Overall, a two-photon resonance enhancement is most preferable since it can increase the nonlinear susceptibility by a factor of $\approx 10^4$ without substantial strong two-photon absorption in the medium due to the fact that the fundamental pulse durations are reasonably short ($\leq$ 10 ns). In my experiment, the output of one dye laser (ω_1) is tuned to be in resonance with a two-photon allowed transition in Kr gas while that for a second dye laser can oscillate at any desired frequency (ω_2). The result is VUV light at the

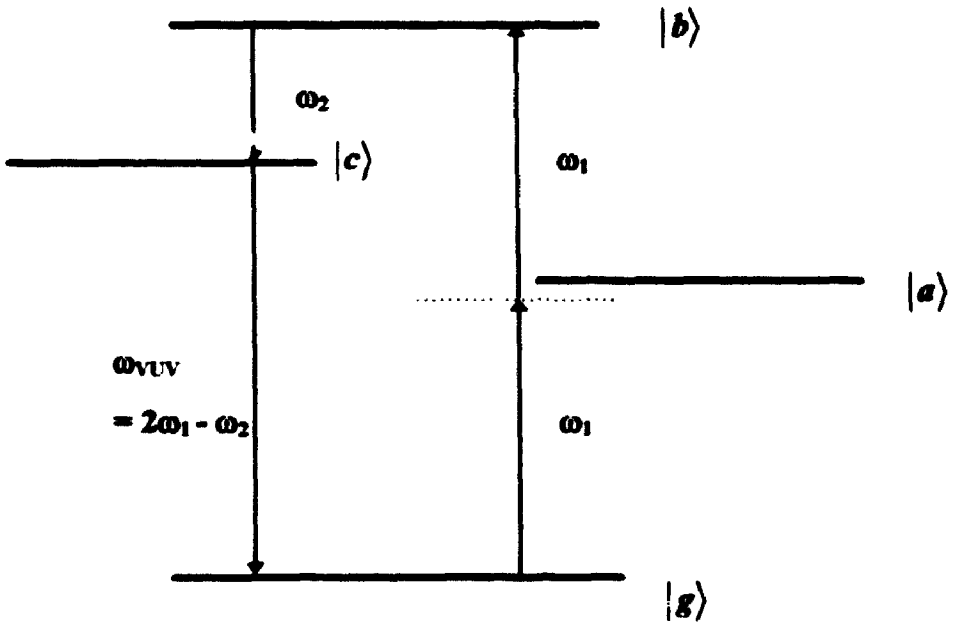

Fig. 2.1. Schematic of two-photon resonantly enhanced four-wave difference mixing in a nonlinear mediur

generated frequency $\omega_{VUV} = 2\omega_1 - \omega_2$. Since ω_2 is unrestricted, the output at $2\omega_1 - \omega_2$ is tunable, and intense due to a constant two-photon resonance enhancement.

As shown in relation 2.11, the magnitude of $\chi^{(3)}$ also depends on the electric dipole matrix elements, and therefore, electric dipole selection rules must be satisfied. For two-photon transitions in atoms:

$$\Delta L = 0,\pm 2; \qquad \Delta S = 0; \qquad \Delta J = 0,\pm 2 \tag{2.12}$$

where L, S, and J are the quantum numbers of the total orbital angular momentum, total spin angular momentum, and total electronic angular momentum, respectively.

The efficiency of the four-wave mixing process, which is also classified as an optical parametric process, depends in part on phase-matching. An expression for the total output power generated by two-photon resonant enhanced four-wave difference mixing, can be deduced by performing a Fourier decomposition of the driving polarization into plane-wave components, and then calculating the produced radiation field which arises from each term. The total output power is then found from the total generated field which can be obtained by adding all component's contributions together [10]. For the process $\omega_1 + \omega_2 - \omega_3 \rightarrow \omega_4$, the total output power P_4 can be written as

$$P_4 \propto P_1 P_2 P_3 N^2 \chi^{(3)^2} F(b\Delta k, b/L, f/L, k''/k'). \tag{2.13}$$

Here, k', the wave vector of the driving polarization, and k'' are defined as: $k' = k_1 + k_2 - k_3$, $k'' = k_1 + k_2 + k_3$; where k_n is the wave vector of the n-th labeled wave having frequency ω_n, n = 1 to 4. $\{P_1, P_2, P_3\}$ and P_4 are the total powers of the fundamental beams and the generated wave, respectively, b is confocal beam parameter, f is the position of the beam waist along the z propagation axis, and L is the length of the nonlinear medium cell. The wave-vector mismatch, Δk, is defined as the difference between the wave vector of the generated radiation and the wave vector of the driving poiarization, that is, $\Delta k = k_4 - k'$. The phase-matching factor, F, in Eq. 2.13, depends only on the dimensionless parameters $b\Delta k$, b/L, f/L, and k''/k'. To achieve the highest possible VUV output power, the phase-matching factor needs to be maximized. The optimum wave-vector mismatch is a function of the tightness and location of the laser

beam focus. In order to achieve the high-power densities required without damaging the window of the cell containing the nonlinear medium, it is often necessary to focus the fundamental beams tightly enough to produce a depth of focus, b, which is small in comparison to the cell length, L. The opposite case is loose focusing where $b >> L$. For the sum-mixing process, $\omega_1 + \omega_2 + \omega_3 \rightarrow \omega_4$, under the tight-focusing condition,

$$F(b\Delta k,0,0.5,1) = \begin{cases} \pi^2 (b\Delta k)^2 \exp[b\Delta k / 2], & \Delta k < 0 \\ 0, & \Delta k \geq 0. \end{cases} \qquad (2.14)$$

This implies that four-wave sum mixing can only be carried out in negatively dispersive nonlinear media. The optimum value of Δk, Δk_{opt}, equals to -2.2/b in this case.

For the difference mixing process, $\omega_1 + \omega_2 - \omega_3 \rightarrow \omega_4$, in the tight-focusing limit and in the case where $k'' = k'$

$$F(b\Delta k,0,0.5,1) = \pi^2 \exp[-b|\Delta k|]. \qquad (2.15)$$

The optimum value of Δk, Δk_{opt}, always equals to zero in either a tight-focusing or loose focusing condition. It follows that for four-wave difference mixing, the nonlinear medium can be both positively and negatively dispersive. For this reason difference mixing processes are generally easier to handle than sum mixing.

From the practical point of view, the power conversion efficiency, η, which is defined as $\eta = P_4/P_1$, is the most important factor under consideration. For the process $2\omega_1 - \omega_2 \rightarrow \omega_{VUV}$,

$$\eta \propto P_1 P_2 N^2 (\chi^{(3)})^2 F(b\Delta k, b / L, f / L, k''/k'), \qquad (2.16)$$

where each symbol retains same meaning as for Eq. 2.13. The use of two-photon resonant enhancement in four-wave mixing processes can increase the power conversion efficiency by several orders of magnitude. Conversion efficiencies as high as 0.4% at 162 nm (corresponding to an output power of 360 W) by two-photon resonantly enhanced difference frequency mixing in Xe gas, were obtained in 1982 by Hager and Wallace [11]. In comparison, the conversion efficiency for nonresonant frequency mixing experiments was reported to be $\approx 10^{-6}$ [12].

The choice of a suitable nonlinear medium is very important since their available two-photon resonances determine the VUV wavelength range that can be generated with commercial dye laser systems. Metal vapors such as Mg, Hg [13], or Zn, or rare gases such as Xe and Kr have all been used effectively for VUV generation. In this thesis, Kr was used primarily for the reason stated above, and due to its ease in handling.

The intensity of the generated harmonic radiation may be seriously limited by various effects including Doppler broadening, absorption, and saturation. Doppler broadening, which results from random thermal motions of the atoms, plays an important role in the two-photon resonance enhancement because it broadens the linewidth of the chosen two-photon resonance transition. Two-photon absorption at resonance can lead to a depletion of fundamental wave and to changes in the initial level populations. This changes the refractive index of the medium at the fundamental and harmonic frequencies which can destroy the phase matching condition. For very intense input fundamentals, higher order non-linear effect (such as 5-th harmonic generation) can also compete with four-wave mixing, thereby reducing the efficiency of the VUV generation. Many of these problems can be eliminated by using moderate input laser intensities. Overall, the utility and understanding of four-wave frequency mixing in gases has reached the point where the process is rarely viewed as a serious research topic, but instead as an extremely useful and compact light source for spectroscopy.

The laser-like VUV four-wave mixing output is intense, coherent, directional, and monochromatic. The frequency bandwidth of generated light, $\Delta\upsilon_{VUV}$, depends on the linewidth of the input dye laser fundamentals. Under our experimental conditions, $\Delta\upsilon_{VUV}$ is estimated to be $< 0.2\ cm^{-1}$. This corresponds to a resolving power, $\upsilon / \Delta\upsilon$, $\geq 250{,}000$. The most competitive VUV light source, synchrotron radiation, however, despite being a reasonably high resolution and monochromatic VUV light, has a typical linewidth of $\approx 80\ cm^{-1}$ which prevents it from being used to pursue any spectroscopy with complete rotational resolution.

2.2 Supersonic Jets

At .oom temperature, many rotational levels of even small molecules are populated, and each populated rotational level can be associated with a number of different transitions upon excitation. Hence, the spectroscopy of samples at room temperature can be very complex. In the 1970's, the introduction of supersonic jet techniques together with powerful lasers revolutionized the field of spectroscopy when it was realized that this type of gas sample produces molecules having low internal energies in a near collision free environment.

Consider the properties of a supersonic jet composed of rare gas atoms such as He. The jet is produced when the gas is expanded adiabatically from a region of high pressure into vacuum through the small nozzle orifice. If the diameter of the orifice is larger than the mean free path for collision between atoms in the high pressure reservoir, there will be many collisions between the atoms as they expand into vacuum. The collisions near the pinhole produce a sample downstream where all atoms move with almost the same velocity, and where there are no more collisions. Thermodynamically, an adiabatic jet expansion converts the enthalpy associated with random atomic motion in the high pressure region into a directed mass flow, with a subsequent increase in the average mass flow velocity, u. On the other hand, the jet sample is characterized by a low translational temperature which decreases with increasing distance from the pinhole. The classical speed of sound, a, is defined as:

$$a = (\gamma kT_{trans}/m)^{1/2} \tag{2.17}$$

where γ is the heat-capacity ratio, C_p/C_v, k is the Boltzmann constant, m is the mass of the molecule, and T_{trans} is the local translational temperature of the medium. The Mach number, M, is defined as:

$$M = u/a \tag{2.18}$$

where u is the mass flow velocity of the gas, and a is the speed of the sound defined by Eq. 2.17. As the gas expands and the translational temperature drops, the local speed of sound decreases relative to the average mass flow velocity. When the resultant Mach number exceeds unity, u is larger than the local speed of sound. For this reason the

expansion described above is termed supersonic. It should be appreciated, however, that u itself is never much greater than the value expected for a room temperature distribution because the enthalpy of the sample in the high pressure region is finite (on the order of RT).

As shown in Fig. 2.2, the much narrower velocity distribution in the jet is indicative of a very low translational temperature since that parameter is determined by the width of the distribution and not by the peak position [14] [15]. Therefore, it is reasonable to conclude that the major process going on in the supersonic expansion is a cooling of the translational degrees of freedom. A supersonic jet is called a free jet when no attempt is made to control the flow pattern downstream with apertures (skimmers).

Next, consider the effect of seeding molecules into the cold expansions. The molecules will attempt to equilibrate with the translationally cold bath by converting energy stored in vibration and rotation into forward motion. In general, the rate of equilibration between translation and rotations is faster than that between translation and vibrations since vibrational level spacings are usually larger than those for rotations. Consequently, a nonequilibrium situation can result because efficient rotational cooling can take place before the vibrational degrees of freedom are relaxed. Rotational temperatures of < 10K are readily achieved. Vibrational temperatures are usually somewhat higher.

In addition, phase equilibration is slow since the number of three body collisions or higher is small As a result, the seeded molecules in the gas phase achieve internal temperatures which are far lower than those necessary to freeze a bulk system.

A quantitative model describing the properties of a supersonic jet is well established. An analysis begins with the adiabatic equation of state for ideal gas which relate the system temperature T, pressure P, and volume V:

$$PV^{\gamma} = nRT \tag{2.19}$$

Specifically, the volume and temperature on both sides of the pinhole producing the jet are related by

$$\left\{\frac{T}{T_0}\right\} = \left\{\frac{V_0}{V}\right\}^{\gamma-1} \tag{2.20}$$

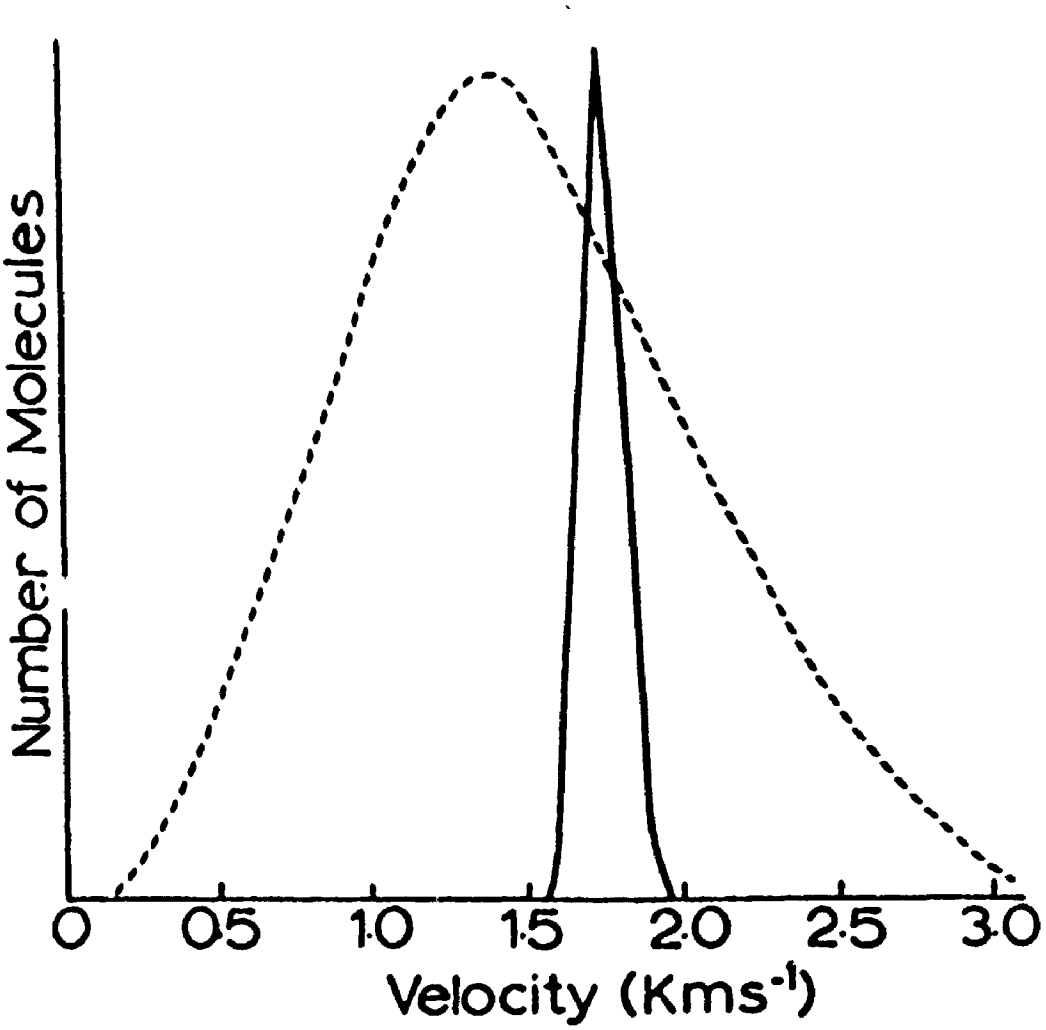

Fig. 2.2. Velocity distribution in effusive molecular beam (dashed curve) and supersonic molecular beam (solid curve). both curves are normalized to unity at the most probable velocity and are for helium at a reservoir temperature of 300 K. The curve for the supersonic molecular beam assumes the gas has been expanded to Mach 30 Noticed shift of the peak of the distribution to higher velocity is due to the increase in mass flow velocity of supersonic expansion [15]

where T_0, V_0 refer to the temperature and volume in the high-pressure reservoir, and T, V refer to the temperature and volume in the expansion. Since in an expansion $V >> V_0$, and $\gamma > 1$, it follows that $T << T_0$. The thermodynamic parameters of T, P, and ρ can be related to the Mach number, M, as follows:

$$\frac{T}{T_0} = \left\{\frac{P}{P_0}\right\}^{\frac{\gamma-1}{\gamma}} = \left\{\frac{\rho}{\rho_0}\right\}^{\gamma-1} = \frac{1}{1+\frac{(\gamma-1)}{\gamma}M^2} \tag{2.21}$$

where T_0, P_0, and ρ_0 refer to the temperature, pressure, and density, respectively, in the high-pressure reservoir, and T, P, and ρ refer to the same quantities in the expanding gas. By treating the expanding gas as a continuous medium, the Mach number can be expressed as a function of distance (X) away from the orifice of diameter (D) of the nozzle in the following way:

$$M = A(X/D)^{\gamma-1} \tag{2.22}$$

A is a constant which depends on γ and is equal to 3.26 for a monatomic gas. As expected the Mach number according to Eq. 2.22 increases as the gas expands, and if the nozzle diameter is increased, molecules have to travel farther to achieve a given Mach number. However, the flow velocity is almost a constant for most of the expansion. Combining equations (2.21) and (2.22) yields following equations for a monatomic gas[17]:

$$\frac{T}{T_0} = 0.25\left\{\frac{X}{D}\right\}^{-1.3} \tag{2.23}$$

$$\frac{P}{P_0} = 0.04\left\{\frac{X}{D}\right\}^{-3.5} \tag{2.24}$$

$$\frac{\rho}{\rho_0} = 0.16\left\{\frac{X}{D}\right\}^{-2.0} \tag{2.25}$$

It can be readily concluded from the equations above that as the gas expands, the temperature, pressure, and density drop as a function of X. Still, this reduction does not continue indefinitely. Relation 2.20 was derived upon the assumption that the gas is continuous, and not made up of discrete atoms and molecules. Eventually, the density

becomes sufficiently low that at certain point the beam becomes collision-free. Here, the Mach number and temperature reach their terminal values. By modeling the particles in expanding gas as classical hard spheres, the terminal Mach number can be expressed as:

$$M_T = 2.05\varepsilon^{(1.\gamma)/\gamma}(\lambda_0 / D)^{(1.\gamma)/\gamma} \tag{2.26}$$

where ε is the collisional effectiveness constant, and λ_0 is the mean free path of the expanding gas [18]. For Argon, Eq. 2.26 reduces to

$$M_T = 133(P_0 D)^{0.4}. \tag{2.27}$$

when P_0 and D are expressed in units of atmospheres and centimeters, respectively. The quantity P_0D is proportional to the total number of binary collisions a molecule makes in the expansion. Thus, the terminal Mach number is determined by the total number of binary collisions molecule undergoes on average.

While the core of the expansion is isentropic [19], the jet is isolated from background gases by nonisentropic barrel shock boundaries (Fig. 2.3). At a certain location downstream in the jet where the pressure in the expansion equals that of the background gas, the jet starts to interact with the background gas through collisions producing a subsonic flow ($M < 1$). This point in the expansion is called the Mach disk, and corresponds to the distance, X_M, from the nozzle throat. It was found experimentally by Ashkenas and Sherman [20] that the location of Mach disk is simply related to the nozzle diameter D, the nozzle stagnation gas pressure P_0, and the background gas pressure in the vacuum chamber, P_1, by:

$$\frac{X_M}{D} = 0.67\left(\frac{P_0}{P_1}\right)^{1/2}. \tag{2.28}$$

As a result, it is desirable to use vacuum pumps with large mass throughputs to maintain a low background gas pressure. Alternatively, pulsed jets with a low duty cycle can be used to deliver gas samples inside a vacuum chamber without the use of a large pump. In this experiment, the latter scenario was employed.

Cluster formation is another factor which can limit cooling in the jet. Although condensation is slow, as noted above, atoms and molecules do associate together. When the resultant binding energy is released, it reheats the jet, thereby increasing the

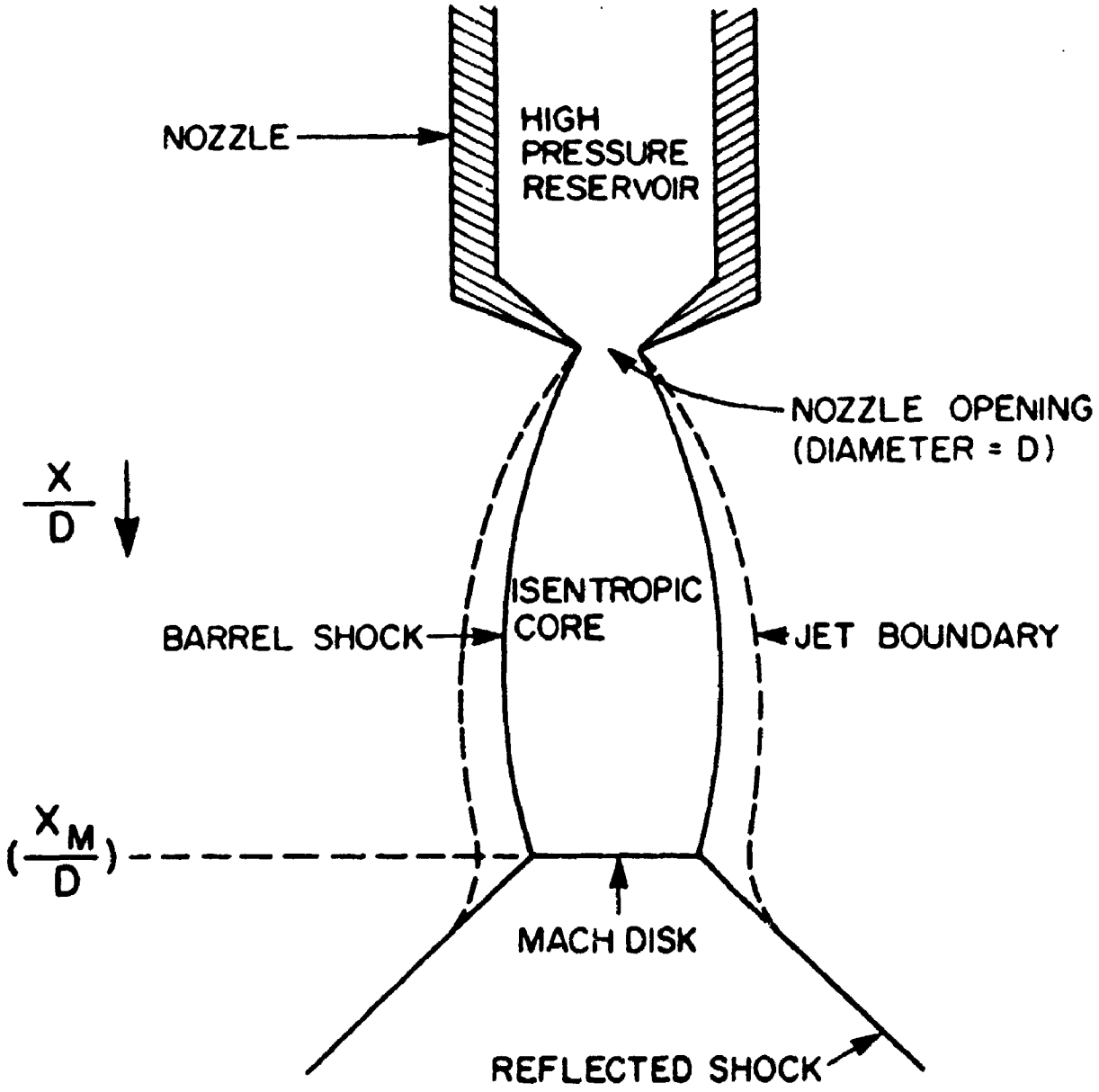

Fig. 2.3. Schematic of the Structure of a free jet [16]

translational temperature. Condensation of the carrier atoms can be minimized by using helium since He_2 is not bound. The formation of complexes requires three-body collisions as a minimum, whereas cooling requires only two-body collisions. The ratio of three-body collisions to two-body collisions is proportional to the number density of atoms, and hence, the stagnation gas pressure. Therefore, for a given terminal temperature, complex formation can be averted by decreasing P_0 and increasing D while keeping P_0D constant. However, an increase in the nozzle pinhole diameter must be accompanied by a larger pump to maintain a good vacuum. For this reason, pulsed expansions are used to reduce the gas load of the pump. Practically, the choice of D and P_0 is usually a compromise between temperature requirements and the desirability of cluster formation. In those cases where clusters are of interest, higher stagnation pressures are generally used to optimize their concentration in the jet.

2.3 Time-of-Flight Mass Spectrometers

Time-of-flight mass spectrometry (TOFMS) was developed more than 40 years ago, and is characterized by many positive features including high collection efficiency, unlimited mass range, and the capability of studying metastable and short-lived ionic species. In particular, TOFMS has found its great utility in experiments involving pulsed laser sources.

The basic operating principle of a conventional linear time-of-flight mass spectrometer is straightforward. Charged particles, once accelerated in an electric field, move at a constant velocity in a field free region. Ions with the same total kinetic energy but having different masses, have different velocities. Consequently, they will reach the end of field-free region at different time of flights. In other words, they will separate according to their masses where the lighter ions arrive before the heavier ones.

Fundamentally, a time-of-flight mass spectrometer is used to determine the mass (M) of a charged particle with known energy (E) by measuring the time-of-flight (TOF) required to travel a predetermined path length (L).

$$E = \frac{1}{2}Mv^2 = \frac{1}{2}M\left\{\frac{L}{T}\right\}^2 = \frac{1}{2}M\frac{L^2}{T^2}, \tag{2.29}$$

therefore,

$$T^2 = ML^2 / 2E ; \tag{2.30}$$

and hence,

$$M = 2ET^2 / L^2 . \tag{2.31}$$

Eq. 2.31 shows that the mass of an ion is proportional to the square of its time-of-flight. By taking the first derivative of Eq. 2.31, one obtains:

$$dM = \frac{4E}{L^2} TdT = 2\frac{2ET^2}{L^2} T^{-1}dT = 2M\frac{dT}{T}. \tag{2.32}$$

Hence, the relationship between the mass resolution ($M / \Delta M$) and time resolution ($T / \Delta T$) becomes

$$\frac{M}{\Delta M} = \frac{T}{2\Delta T} \tag{2.33}$$

For a fixed E and L, the mass resolution is then determined by how accurately both T and ΔT can be measured. If all of the ions were produced from neutrals at rest in one location in the ion source region, then the TOF should be identical for all ions with the same mass to charge ratio. In reality, however, the initial spread in the velocities of the ions produced must be considered. In fact, it is the initial spread in the velocity distribution of the ions that primarily limits the mass resolution for these types of spectrometers.

Generally, the initial ion kinetic energy is determined by the initial kinetic energy of the molecule from which the ion is produced, and the method of ionization. The ions will exhibit a spread in TOFs which reflect this energy and velocity distributions of the parent neutrals. Typically, for a room temperature gas sample the energy spread is on the order of 0.025 eV. This represents one of the major factors which degrades the mass resolution of the instrument, even though it may be quite small compared to the final accelerated ion energy. In addition, if the ions are produced by dissociative ionization; that is,

$$e^- + AB \rightarrow A + B^+ + 2e^- + \text{kinetic energy} \tag{2.34}$$

or

$$\rightarrow A + B^- + \text{kinetic energy}$$

$$h\upsilon + AB \rightarrow A^+ + B + e^- + \text{kinetic energy}$$

$$\rightarrow A^- + B^+ + \text{kinetic energy}$$

then kinetic energy spreads between a few electron volts and tens of electron volts are possible.

One method to reduce the initial ion energy spread is to employ an electrostatic energy analyzer which can select a certain ion kinetic energy for TOF mass analysis. However, here a reduction in the ion collection efficiency is the major drawback. Alternatively, a supersonic nozzle jet can be utilized. There, the velocity spread of the molecules in the expansion is minimized because their velocity vector points primarily in the flow direction. Since ionization usually takes place at one location in the supersonic jet, the initial ion energy spread is greatly reduced, resulting in dramatically improved TOF mass resolution. However, if ions are produced over a large spatial region, the mass resolution will also be adversely affected. Wiley and Mclaren [21] have derived the so-called space focusing conditions for a TOFMS to treat this initial volume problem.

As shown in Fig. 2.4, the source region of a linear TOFMS can be divided into an ionization region I, an acceleration II, and drift region III. If two ions of the same mass, each initially with zero kinetic energy are produced at different locations, $S_0 \pm \delta$, in region I, the mass starting at $S_0 + \delta$ will acquire more energy than the mass starting at $S_0 - \delta$ since the former travels a longer distance than the latter in the ionization region. Accordingly, at some point down the field-free flight tube, the faster ion will surpass the slower one despite the fact that the slower one was initially 2δ ahead. The peak resolution will be achieved if the detector is placed right at the take-over position. This is the basic idea behind the space-focusing condition. Suppose the electric field in region I is E_s, and E_d in region II, the total time of flight of an ion at position $S = S_0$ with initial kinetic energy $U_0 = 0$ through all three regions can then be derived as follows:

$$T(U_0, S_0) = 1.02 \frac{(M)^{1/2}}{(2U_t)^{1/2}} \left[2k_0^{1/2} + \frac{2k_0^{1/2}}{k_0^{1/2} + 1} d + D \right] \qquad (2.35)$$

where M is mass of the ion, D is the length of the drift tube, d is the length of acceleration region, U_t is the gained kinetic energy of the ion which is equal to:

$$U_t = qS_0E_S + qdE_d \qquad (2.36)$$

and

$$k_0 = (S_0E_S + dE_d) / S_0E_S \ . \qquad (2.37)$$

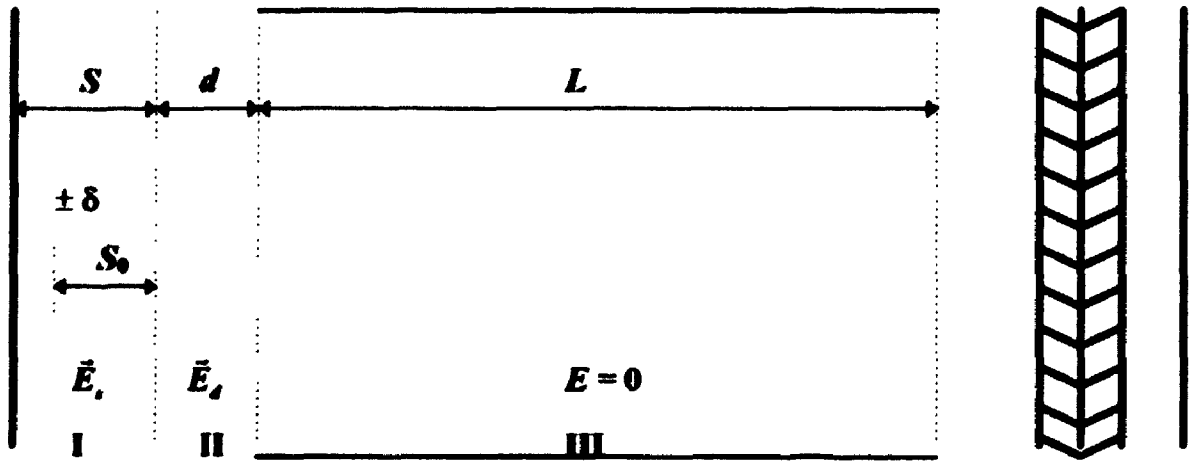

Fig. 2.4. Basic TOF geometry showing two ions initially formed at $S_0 \pm \delta$.

By taking the first derivative of Eq. 2.35; that is, dT/dS, and setting $(dT/dS)_{0,S_0} = 0$, an expression for the position at which the ion starting at $S_0 + \delta$ catches up with the ion starting at $S_0 - \delta$, can be deduced:

$$D = 2S_0 k_0^{3/2}\left(1 - \frac{1}{k_0 + k_0^{1/2}}\frac{d}{S_0}\right) \qquad (2.38)$$

This represents the space-focusing condition which should be satisfied to achieve the maximum mass resolution. In a real system the length of flight tube D is fixed. However, by varying the electric fields E_S and E_d, relation 2.38 can be fulfilled to attain the ideal resolution. In practice, this is done by monitoring the output of a detector at the end of the flight tube with a digital oscilloscope and adjusting the different voltages until the narrowest peak is obtained for a given mass.

As mentioned earlier, the energy spread of the ions inside the flight tube can be fairly small when the parent neutral molecules are delivered by a supersonic nozzle whose direction is perpendicular to the flight tube. As a result, a great improvement in resolution can be achieved using supersonic jets. However, since the ions essentially only have a velocity component perpendicular to the TOF axis, it is necessary to employ the X-Y deflection plates to direct the ions back on axis toward the detector.

The combined techniques of time-of-flight mass spectrometry, supersonic beam sources, together with the use of high power pulsed lasers, have great potential for high resolution spectroscopy, as demonstrated by the experiments detailed in this thesis.

2.4 Basic Electronic Spectroscopy

Spectroscopy is a very broad field involving the interaction of light with matter. At a basic level, the information which can be derived from molecular spectra includes molecular structure and molecular energy level spacings. Quantum mechanics forms the foundation for understanding spectroscopy, and selection rules are extremely important since they govern which spectroscopic transitions are allowed [22].

The types of molecular motions that accompany the absorption of electromagnetic radiation depend on the energy of the photons used for excitation. In the microwave region ($\lambda \approx (3\text{-}300)\times 10^6$ nm) transitions can be induced between rotational energy levels of a vibrational state. In the infrared region ($\lambda \approx 770\text{-}5\times 10^5$ nm) light absorption leads to changes in vibrational energy accompanied by changes in rotational energy. Typically, transitions occur between electronic levels of molecules when they are excited by visible, ultraviolet, or vacuum ultraviolet radiation. Electronic spectra may contain many lines because molecules may also change their vibrational and rotational states. The analyses of rotational spectra yield moments of inertia and interatomic distances and for polyatomics, bond angles. The investigation of vibrational spectra provides fundamental vibrational frequencies and force constants. Finally, electronic spectra can supply information about electronic excited state geometry and potential energy curve dissociation energies.

2.4.1 Born-Oppenheimer Approximation

It is nearly impossible to establish an exact quantum-mechanical solution for most molecular systems since they are composed of interacting electrons as well as nuclei which viorate even in the lowest vibrational energy state. However, since the electrons are much lighter and move much faster than the nuclei, it is reasonable to treat the electronic motion with the nuclei fixed in position. This is the basic premise of the Born-Oppenheimer approximation proposed in 1927 [23].

Just as for an atom, the Hamiltonian operator, $\hat{H}$, for a diatomic molecule is the sum of those for the kinetic energy, $\hat{\mathrm{T}}$, and the potential energy, $\hat{\mathrm{V}}$. In a molecule, the kinetic energy contains contributions from the motions of the electrons, $\hat{T}_e$, and nuclei, $\hat{T}_n$, respectively. The potential energy can be divided into two terms, $\hat{V}_{ee}$ and $\hat{V}_{nn}$, due to Coulombic repulsions between the electrons and nuclei, respectively, and a third term $\hat{V}_{en}$ due to the attractive forces between the electrons and nuclei. In total, $\hat{H}$ is given by [24]:

$$\hat{\mathrm{H}} = \hat{\mathrm{T}}_e + \hat{\mathrm{T}}_n + \hat{\mathrm{V}}_{en} + \hat{\mathrm{V}}_{ee} + \hat{\mathrm{V}}_{nn} \qquad (2.39)$$

For fixed nuclei $\hat{\mathrm{T}}_n$ is zero and $\hat{V}_{nn}$ is a constant. Hence, $\hat{H}_e = \hat{T}_e + \hat{V}_{en} + \hat{V}_{ee}$.

There is a set of electronic wave functions, $\{\psi_e\}$, which satisfy the Schrödinger equation

$$\hat{H}_e\psi_e = E_e\psi_e \tag{2.40}$$

Since $\hat{H}_e$ depends on the nuclear coordinates due to the term $\hat{V}_{en}$, then so does the set $\{\psi_e\}$ and eigenvalues, $\{E_e\}$. As mentioned earlier, Born and Oppenheimer introduced an approximation based on the fact that the nuclei are so much more massive than the electrons, that the nuclei can be assumed to be stationary during an electronic transition. One can therefore, choose the nuclei to have a definite separation, r, and solve Eq. 2.40 for the electron distribution alone. The molecule will have well defined electronic potential energy, V, for any relative position. The potential energy of the molecule at the selected separation is the sum of E_e and the internuclear repulsion, $e^2 / 4\pi\varepsilon_0 r$. As this calculation can be repeated for all separations, the variation of the energy of the molecule with bond length within any electronic state can be determined.

A typical molecular potential energy curve is shown in Fig. 2.5. There is a decrease in electronic potential energy as the two nuclei approach each other from a large distance. A minimum energy is reached because of bonding at r_e, the equilibrium internuclear distance. As the nuclei approach more closely, however, the energy rises rapidly due to internuclear repulsion. The equilibrium dissociation energy, D_e, corresponds to the energy required to dissociate the diatomic starting from the potential minimum, while the spectroscopic dissociation energy, D_0, is the energy required to dissociate a molecule in its lowest vibrational state, v = 0. [22]

Again, since the electronic motion is fast compared with that for the nuclei, at any instant the electronic energy can be deemed to have reached its equilibrium value corresponding to that internuclear distance. For this reason the vibrations and rotations of the nuclei can be treated separately from the electronic motion. In other words, E_e can be considered part of the potential field in which the nuclei move. Thus [24]

$$\hat{H}_n = \hat{T}_n + \hat{V}_{nn} + \hat{E}_e \tag{2.41}$$

The Schrödinger equation for nuclear motion is

$$\hat{H}_n\psi_n = E_n\psi_n \ . \tag{2.42}$$

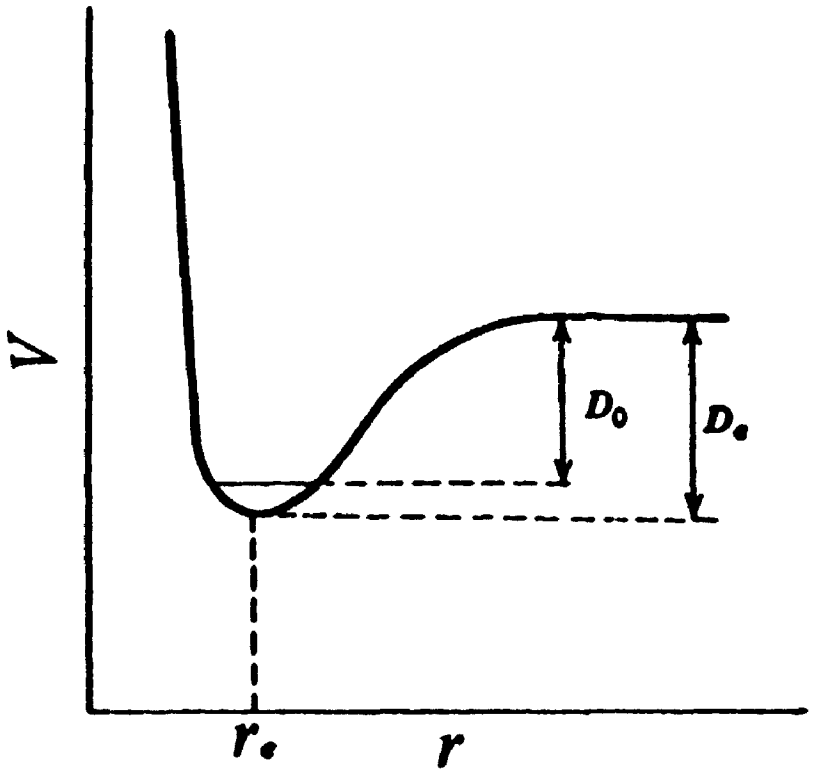

Fig. 2.5. Potential energy V for a diatomic molecule as a function of internuclear distance r [24].

It follows that the total wave function for the molecular system, ψ, can be factorized

$$\psi = \psi_e \psi_n \tag{2.43}$$

which leads to $E = E_e + E_n$. Since, the wavefunction for the nuclear motion, ψ_n, can be further factorized into a vibrational component, ψ_v, and a rotational part, ψ_r, where

$$\psi_n = \psi_v \psi_r \tag{2.44}$$

$E_n = E_v + E_r$. It follows that

$$\psi = \psi_e \psi_v \psi_r \tag{2.45}$$

and

$$E = E_e + E_v + E_r. \tag{2.46}$$

Here, spectroscopists generally use wavenumber units, υ, instead of energy. In this case,

$$\upsilon = \upsilon_e + \upsilon_v + \upsilon_r \tag{2.47}$$

and each component, υ_i, can be calculated from E_i/hc.

2.4.2 Electronic Transition Selection Rules

There are restrictions on which spectroscopic transitions can occur between energy levels of molecules by absorption (or emission) of electromagnetic radiation, called selection rules. Generally, the interaction of a molecular electric-dipole with radiation is strongest. Since both magnetic dipole and quadropole transitions are $\geq 10^5$ times weaker than electric dipole transitions, the discussion here will concentrate only on the latter.

It is instructive to begin with an introduction to the classification of electronic states of diatomic molecules. This is accomplished by the use of molecular term symbols. There are a total of 5 ideal coupling cases defined by Hund to describe the interaction of the different angular momenta in a diatomic molecule. However, only Hund's case (a) and (c) were used in this thesis and are to be explained in the following section [25]

(1) Hund's Case (a)

Hund's case (a) is the most common case, especially for light molecules. In this coupling scheme, the electronic spin-orbit interaction is weaker than the interaction of the electrons with the electrostatic field along the internuclear axis. In a diatomic molecule the orbital angular momenta of the individual electrons couple to give a resultant total

orbital angular momentum L, while the individual electron spin momenta combine to give a resultant total spin angular momentum S. The components of the orbital angular momentum along the internuclear axis of the diatomic molecule are given by

$$M_L = L, L\text{-}1, L\text{-}2, \ldots, -L \tag{2.48}$$

The quantum number Λ corresponds to a particular component of electronic orbital angular momentum along the internuclear axis, and is defined as the absolute value of M_L; that is,

$$\Lambda = |M_L| \tag{2.49}$$

States are labeled by the Greek letters, Σ, Π, Δ, Φ, Γ,... when Λ = 0, 1, 2, 3, 4, ..., respectively. In accordance with Eq. 2.49 molecular states with $\Lambda > 0$ are doubly degenerate because a positive Λ can have either a $+M_L$ or $-M_L$ component corresponding to electrons rotating about bond axis in a clockwise or counter clockwise direction. On the other hand, Σ states are non-degenerate since $M_L = 0$ and there is no orbital angular momentum.

The component of the spin angular momentum along the internuclear axis is labeled by Σ which is analogous to M_S in atoms. Σ can take the values

$$\Sigma = S, S\text{-}1, S\text{-}2, \ldots, -S \tag{2.50}$$

and should not be confused with the $\Lambda = 0$ term symbol. Like atoms, the spin multiplicity of a molecular electronic state is given by $2S + 1$. The complete term symbol of a molecule in Hund's case (a) representation is given by

$$^{2S+1}\Lambda_{\Omega} \tag{2.51}$$

where $\Omega (= \Lambda + \Sigma)$ is the quantum number characterizing the component of the total angular momentum along the direction of the bond.

In addition to the quantum numbers discussed above, the symmetry properties of the electronic eigenfunctions need to be considered. These symmetry properties depend on the electrostatic field produced by the two nuclei, and in which the electrons move [25]. In a diatomic molecule, the plane passing through the internuclear axis is a plane of symmetry. When the electronic wavefunction of a Σ state is reflected through the plane containing both nuclei, it either stays unchanged or changes its sign. The former is called a

Σ^- state while the latter case is denoted by Σ^+. For degenerate states with $\Lambda > 0$ the Λ^+ and Λ^- components are isoenergetic to the first-order. However, an energy splitting does occur for states with $\Omega = 0$, but $\Lambda \neq 0$. For example, a $^3\Pi_0$ state can either be a $^3\Pi_{0^+}$ state or a $^3\Pi_{0^-}$ state, and each has a different energy.

For homonuclear diatomics, the electrostatic field in which the electrons move also possesses a center of symmetry. As a result, the electronic eigenfunctions can either remain unchanged or change sign upon inversion through this center (that is, $(x_i, y_i, z_i) \rightarrow (-x_i, -y_i, -z_i)$). The former case is an even (gerade) state, and is indicated by a subscript g. The latter case is an odd (ungerade) state which is denoted by the subscript u. Quantum mechanically, this operation is fulfilled by the parity operator. Both degenerate and non-degenerate terms have this property.

(2) Hund's Case (c)

Hund's case (c) occurs at long bondlength for heavy molecules with many electrons. This scenario is the most appropriate coupling case when the spin-orbit interaction between L and S is stronger than the interaction with the internuclear axis. In this situation Λ and Σ are not defined. Instead, L and S add vectorially to form a resultant J_a, which is subsequently coupled to the internuclear axis. The component along the bond axis is again labeled by Ω. Molecular terms are distinguished by the quantum number Ω such that $\Omega = 0, 1, 2, \ldots$ corresponds to 0, 1, 2, ... states. Parity labeling (g, u) remains the same as described for Hund's coupling case (a).

(3) Electronic Selection Rules

If ψ_1 represents the wave function of the initial state 1, and ψ_2 represents the wave function of the final state 2, the transition dipole moment matrix element is defined by [22]

$$R_{21} = \int \psi_2 \, \hat{\mu} \, \psi_1 d\tau \qquad (2.52)$$

where $\hat{\mu}$ is the electric dipole moment operator, and $d\tau$ is the differential volume. The integral provides a measure of the dipole charge redistribution in the molecule under the influence of an electric field when the molecule changes its state. If Eq. 2.52 is zero for a

particular transition, then electromagnetic radiation cannot induce an electric dipole allowed transition. The transition is then said to be forbidden even though much weaker transitions between the states may still be possible by higher order multipolar moments. The selection rules derived from equation 2.52 outlines the changes in quantum numbers and symmetry that are permitted for an allowed transition.

An electronic transition occurs between two potential energy curves. The electric dipole allowed single-photon electronic selection rules for Hund's coupling case (a) can be written as following:

$$\Delta\Lambda = 0,\pm 1 \tag{2.53}$$

$$\Delta S = 0 \tag{2.54}$$

$$\Delta\Sigma = 0 \tag{2.55}$$

$$\Delta\Omega = 0,\pm 1 \tag{2.56}$$

$$\Sigma^+ \leftrightarrow \Sigma^+; \quad \Sigma^- \leftrightarrow \Sigma^- \tag{2.57}$$

$$g \leftrightarrow u, \tag{2.58}$$

and for Hund's coupling case (c):

$$\Delta\Omega = 0,\pm 1 \tag{2.59}$$

$$g \leftrightarrow u \tag{2.60}$$

$$0^+ \leftrightarrow 0^+; \quad 0^- \leftrightarrow 0^-. \tag{2.61}$$

2.4.3 Vibrational Structure of Electronic Transitions

If the vibration of a diatomic molecule can be described as a simple harmonic oscillation, then the motion of the two atoms can be reduced as the harmonic vibration of a single mass point. Quantum mechanically, the energy eigenvalues of such a system, $E(\mathrm{v})$, are given by [25]:

$$E(\mathrm{v}) = \frac{\mathrm{h}}{2\pi}\sqrt{\frac{\mathrm{k}}{\mu}}\left(\mathrm{v}+\frac{1}{2}\right) = h\upsilon_{\mathrm{osc.}}\left(\mathrm{v}+\frac{1}{2}\right) \tag{2.62}$$

where k is the force constant, μ is the reduced nuclear mass of the system, v is the vibrational quantum number which can take integer values ≥ 0, and $\upsilon_{\mathrm{osc.}} = \frac{1}{2\pi}\sqrt{\frac{k}{\mu}}$ is the

classical vibrational frequency of the oscillator Equation 2.62 indicates that the frequency spacing of adjacent vibrational levels is a constant. The term values, $G(v)$, can be readily obtained from equation 2.62

$$G(v) = E(v)/hc = \frac{\upsilon_{osc.}}{c}\left(v + \frac{1}{2}\right) = \omega\left(v + \frac{1}{2}\right) \qquad (2.63)$$

where $\omega = \upsilon_{osc.}/c$ is the vibrational frequency, generally quoted in cm^{-1} wavenumber units. In an actual molecule, however, the vibrations of the two nuclei are anharmonic. Equation 2.63 then needs to be expanded in a power series in $(v + \frac{1}{2})$ to account for this effect:

$$G(v) = \omega_e\left(v + \frac{1}{2}\right) - \omega_e x_e\left(v + \frac{1}{2}\right)^2 + \omega_e y_e\left(v + \frac{1}{2}\right)^3 + \cdots \qquad (2.64)$$

where ω_e is the vibrational frequency, $\omega_e x_e$, $\omega_e y_e$, ..., are anharmonicity constants, and $\omega_e >> \omega_e x_e >> \omega_e y_e$, etc. Except in a few isolated instances, the constant $\omega_e x_e$ is positive for all diatomic molecules, while the high order terms in the expansion may be either positive or negative. Indeed, the higher order terms in Eq. 2.64 only become significant with increasing v and/or for very light molecules. As well, the spacings between the vibrational levels decrease with increasing v. Lastly, the zero-point energy, $G(0)$, can be calculated directly from Eq. 2.64 by setting $v = 0$.

Vibrational transitions in electronic spectra (that is, vibronic transitions) occur between two vibrational levels within the potential energy curves associated with two electronic states, and are labeled by v' and v'', where v' and v'' are vibrational quantum numbers in upper and lower state, respectively.

Vibronic transitions can be divided appropriately into progressions and sequences As shown in Fig. 2.6, a progression involves a series of vibronic transitions with a common lower or upper vibrational level, while a group of transitions with the same value of Δv (= v' - v'') is referred to as a sequence.

There is no general selection rule for vibrational transitions in terms of the change in vibrational quantum number. However, the vibrational intensity distribution is controlled by Franck-Condon factors which will be discussed in the following section.

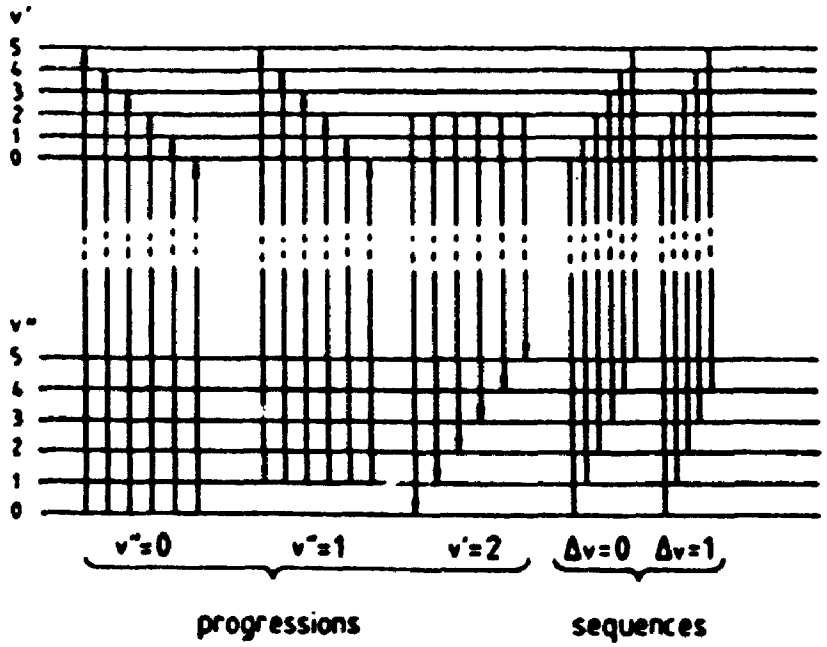

Fig. 2.6. Vibrational progressions and sequences in the electronic spectrum of a diatomic molecule [24].

2.4.4 The Franck-Condon Principle

A diatomic molecule in its ground vibrational state, has a bondlength very close to the equilibrium internuclear distance. However, when the molecule absorbs a photon and ends up in a higher excited electronic state, the equilibrium internuclear distance can be different from that of the ground state. In 1925, Franck recognized that since an electronic transition occurs much more quickly than a vibrational transition, the nuclei have nearly the same position and velocity before and after the transition [24]. As a result, an electronic transition can be represented in a potential energy diagram by a vertical line (Fig. 2.7). In this figure, the upper curve represents an excited state, while the lower curve represents the ground state in an absorption process where $r_e' > r_e''$ in (a) and $r_e' \approx r_e''$ in (b). The transition from point A in the ground state will terminate on point B in the excited state, but not on point C, since the former transition lies on a vertical line in Fig. 2.7 (a), and therefore, meets the requirement that the nuclei have the same position before and after the transition. Similarly, transitions from points A in Fig 2.7 (a) and (b) where the nuclei are stationary to points D and C, respectively, where the nuclei are in motion are also unlikely. In general, vibronic transitions probe the classical tuning points of a vibration where the nuclei are stationary.

Condon treated Franck's principle quantum mechanically in 1928. The intensity of a vibronic transition is proportional to the square of the transition moment R_{ev}

$$R_{ev} = \int \psi'^{*}_{ev}\ \hat{\mu}\ \psi''_{ev}\, d\tau_{ev} \tag{2.65}$$

where $\hat{\mu}$ is the electric dipole moment operator, ψ'_{ev} and ψ''_{ev} are the vibronic wave functions of the upper and lower states, respectively, and the integration is taken over the electronic and vibrational coordinates. According to Born-Oppenheimer approximation discussed earlier, ψ_{ev} can be factorized as $\psi_e\psi_v$. Hence, Eq. 2.65 can be written

$$R_{ev} = \iint \psi'^{*}_{e}\,\psi'_{v}\ \hat{\mu}\ \psi''_{e}\,\psi''_{v}\, d\tau_e dr\,. \tag{2.66}$$

By integrating over the electronic coordinates τ_e, and setting $R_e = \int \psi'^{*}_{e}\ \hat{\mu}\ \psi''_{e}\, d\tau_e$, Eq. 2.66 reduces to

$$R_{ev} = \int \psi'_{v}\ R_e\ \psi''_{v}\, dr\,. \tag{2.67}$$

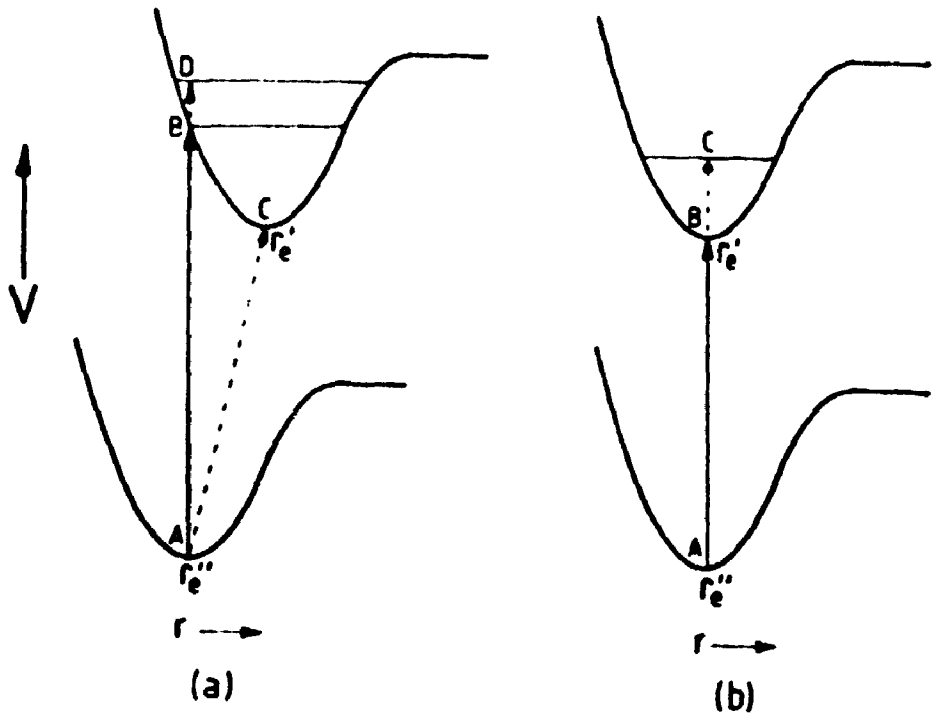

Fig. 2.7. Illustration of the Franck-Condon principle for (a) $r_e' > r_e''$ and (b) $r_e' \approx r_e''$. The vibronic transition B-A is the most probable in both cases [24].

Given that R_e is independent of the internuclear distance r, it can be taken outside of the integral in equation 2.67,

$$R_{e'v'} = R_e \int \psi'_{v'} \psi''_{v''} \, dr \,. \tag{2.68}$$

The quantity $\int \psi'_{v'} \psi''_{v''} \, dr$ is called the vibrational overlap integral. The Franck-Condon factor, defined as the square of the overlap integral, governs the intensity of a vibronic transition. It follows that the greater the Franck-Condon factor, the more intense the vibronic transition will be.

In the quantum mechanical interpretation of the Frank-Condon principle [25], the classical tuning point is replaced by either a maximum or a minimum in the amplitude of ψ_v near this point on the potential energy curve. The higher the vibrational quantum number v, the closer the amplitude of ψ_v is to the classical tuning point, as illustrated in Fig. 2.8 (a) for v=28. Consider the particular case shown in Fig. 2.8 (b), where the maximum of the v'=4 wave function near to the classical tuning point is vertically above that of v''=0. As a result, the maximum intensity in the stick spectrum for the (v', 0) progression shown in Fig. 2.8 (c) occurs for (4, 0). On the other hand, appreciable overlapping extends to values of r within the dashed lines on figure 2.8 (b). Consequently, the intensity distribution for the v''=0 progression has the distinctly Gaussian appearance illustrated in Fig 2.8 (c).

2.4.5 Rotational Structure of Electronic Transitions

The simplest description of the rotational motion of a diatomic molecule is the "rigid rotator" model in which the bond joining the two nuclei is regarded as a rigid and massless rod. The rotational energy, $E_v(J)$, for a given vibrational level, v, can be written as [26]

$$E_v(J) = \frac{h^2 J(J+1)}{8\pi^2 \mu r_v^2} = \frac{h^2 J(J+1)}{8\pi^2 I} \tag{2.69}$$

where J is the integer rotational quantum number ≥ 0, r_v is the equilibrium bond length for the given vibrational level, I is the moment of inertia = μr_v^2. The rotational term values

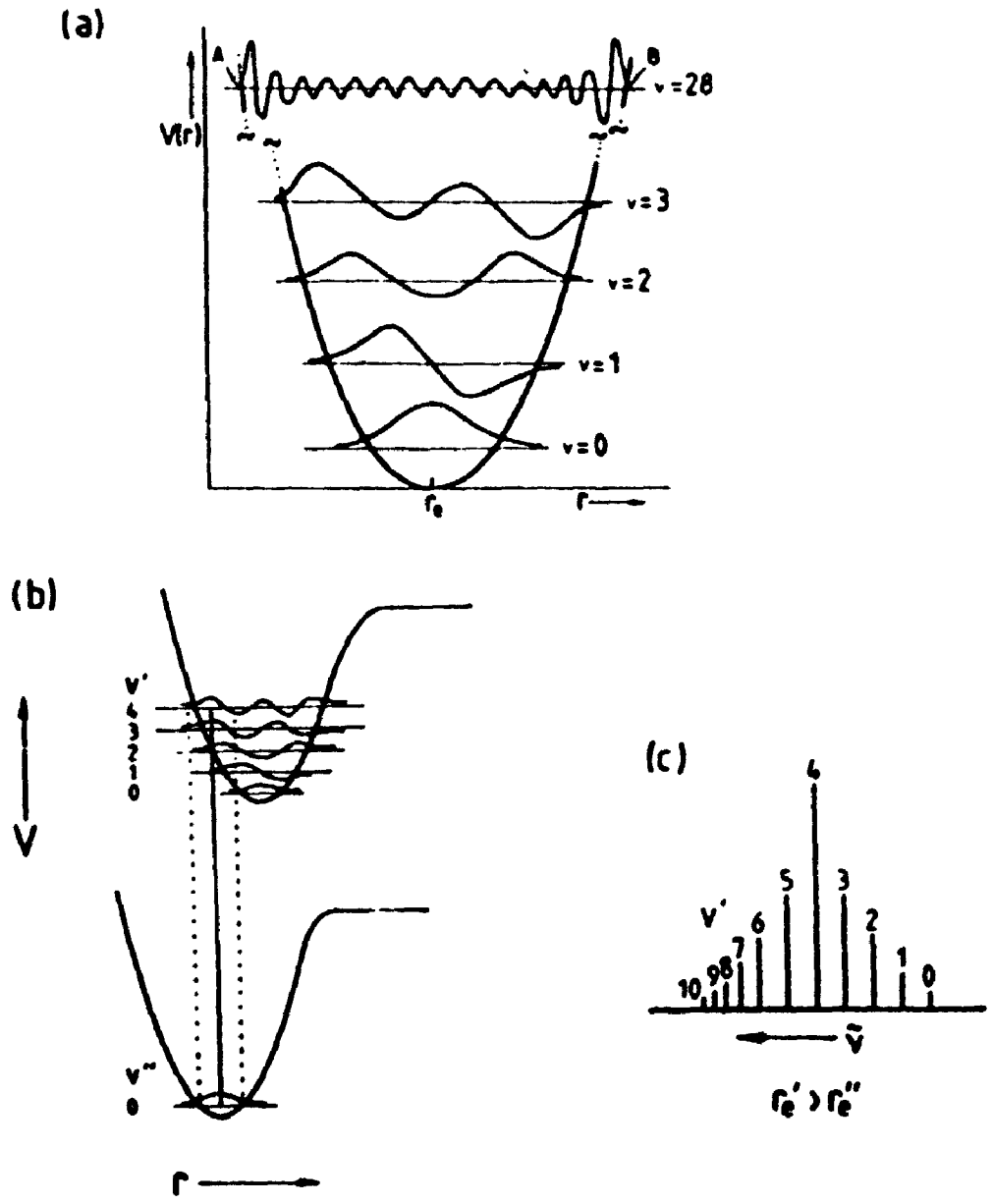

Fig. 2.8. (a) Plot of $V(r)$ against r for the harmonic oscillator model for vibration. A few energy levels and wave functions are shown.
(b). Franck-Condon principle applied to a case in which $r_e' > r_e''$ and where the (4, 0) transition is the most probable.
(c). Typical vibrational progression intensity distribution for the case of $r_e' > r_e''$ [24].

can be easily obtained from Eq. 2.69,

$$F_v(J) = E_v(J)/hc = \frac{h}{8\pi^2 cI} J(J+1) = B_v J(J+1) \qquad (2.70)$$

where B_v is called rotational constant for a given vibrational level. A diatomic molecule is not a strict rigid rotator, however, since it is also subject to centrifugal distortion forces which stretch the bond. Therefore, term values for a nonrigid rotator model, $F_v(J)$, are used instead, where $F_v(J)$ is given by:

$$F_v(J) = B_v J(J+1) - D_v J^2(J+1)^2 + H_v J^3(J+1)^3 + \cdots \qquad (2.71)$$

Here D_v is the centrifugal distortion constant, and is large when the bond is easily stretched. In a well behaved system, the sign of $D_v J^2(J+1)^2$ is negative ($D_v > 0$) since the effect of centrifugal distortion is to increase r_v and therefore, decrease B_v. H_v and any other higher order constants describing the nonrigidity of the bond are added when needed, but are generally quite small. Their contributions only become appreciable for very light molecules, and/or high J values. Their sign can be either positive or negative. In the harmonic approximation the centrifugal distortion constant is related to the vibrational frequency of the bond, ω_v through:

$$D_v = 4B^3_v/\omega^2_v \qquad (2.72)$$

The rotational structure of a rovibronic transition, that is, an electronic transition accompanied by changes in both the vibrational and rotational states of the molecule, can be understood by considering the contribution of the rotational energy to the emitted or absorbed energy of the photon [25]:

$$\upsilon = \upsilon_e + \upsilon_v + \upsilon_r \qquad (2.73)$$

The quantity $\upsilon_0 = \upsilon_e + \upsilon_v$ is a constant for a particular vibronic transition while υ_r is variable and depends on the different values of the rotational quantum number in the upper and lower states. All possible rotational transitions with a constant υ_0 group together to form a single band. Transition wavenumbers can be expressed by the following relationship:

$$\upsilon = \upsilon_0 + F_v'(J') - F_v''(J'') \qquad (2.74)$$

where $F_v'(J')$ and $F_v''(J'')$ are the rotational term values for the upper and lower state, respectively, and υ_0 is the band origin. The rotational selection rules determined from the electric dipole matrix elements of the transition are:

$$\Delta J = 0, \pm 1. \tag{2.75}$$

However, $\Delta J = 0$ is forbidden when $\Lambda = 0$ or $\Omega = 0$ in both electronic states. According to the selection rules, up to three series of lines, called branches, can be formed:

$$R \text{ branch: } \upsilon = \upsilon_0 + F_v'(J+1) - F_v''(J) = R(J), \tag{2.76}$$

$$Q \text{ branch: } \upsilon = \upsilon_0 + F_v'(J) - F_v''(J) = Q(J), \tag{2.77}$$

$$P \text{ branch: } \upsilon = \upsilon_0 + F_v'(J-1) - F_v''(J) = P(J). \tag{2.78}$$

Here the Js are the rotational quantum numbers in the lower state (= J''). The P and R branches can be represented together by a single formula,

$$\upsilon = \upsilon_0 + (B_v' + B_v'')m + (B_v' - B_v'')m^2, \tag{2.79}$$

where $m = -J$ for the P branch and $m = J + 1$ for the R branch. Incorporating the Q branch into Eq. 2.79 usually cannot be done without taking Λ-doubling into account [25]. An illustration of all three branches (P, Q, and R) of a $^1\Pi \leftarrow {}^1\Sigma$ transition are shown in Fig. 2.9.

In most cases either the P or R branch can "turn back"; that is, form a band head due to the quadratic term in Eq. 2.79. The band head is formed in the R branch if $B_v' < B_v''$, which implies that the internuclear distance in the upper state is longer than that in the lower state. In this case, a frequency maximum is reached for certain value of J to the blue of the band origin. The band is then said to be shaded toward the red. Conversely, the band head is formed in the P branch if $B_v' > B_v''$, which indicates that the bond length in the upper state is shorter than that in the lower state. In this latter case, the head lies to the red of the band origin, and the band is said to be shaded toward the violet. By taking the first derivative of Eq. 2.79, $d\upsilon / dm$, and setting it equal to zero, the value of m corresponding to the band head, can be obtained:

$$m = -(B_v' + B_v'')/2(B_v' - B_v''). \tag{2.80}$$

An expression for the frequency separation between the head and the band origin can be found by substituting relation 2.80 into Eq. 2.79.

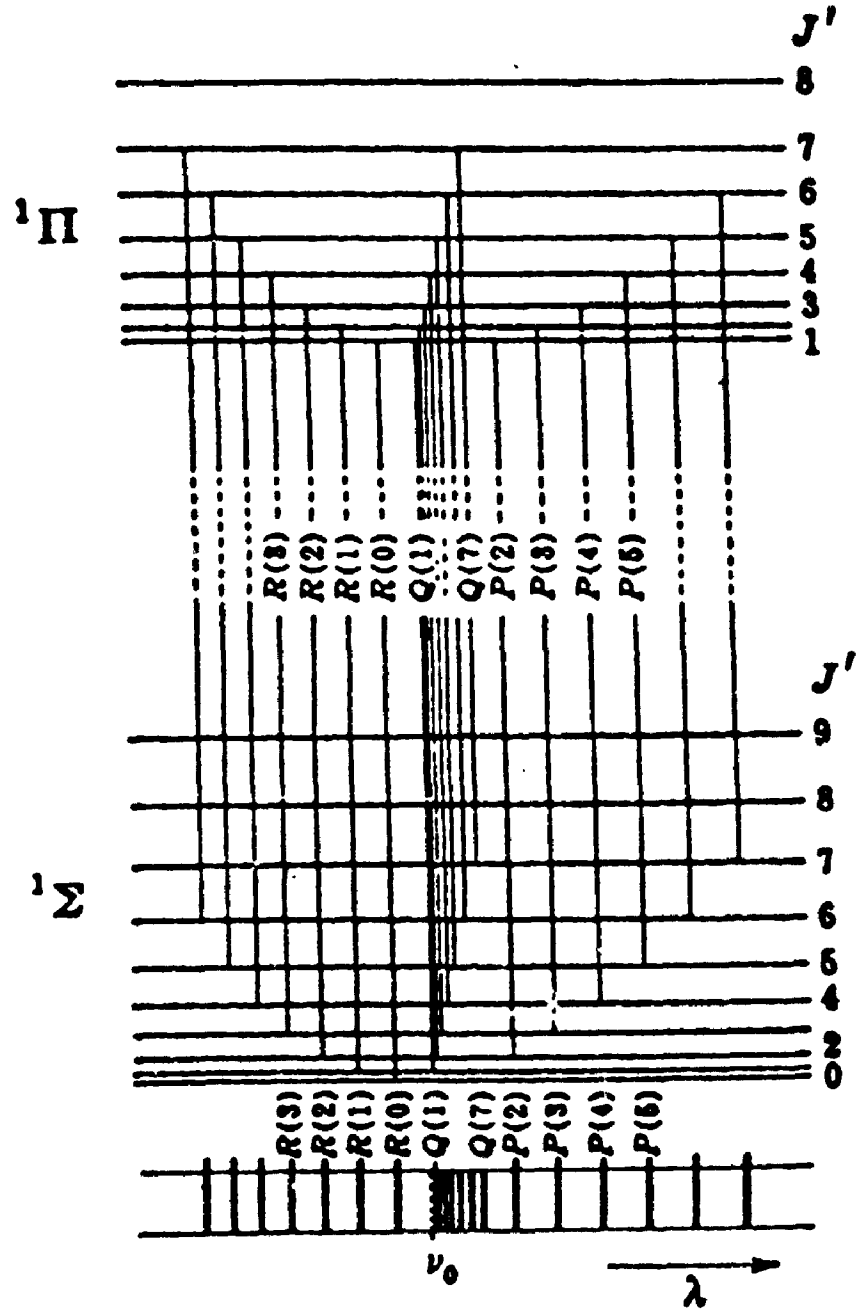

Fig. 2.9. Energy Level Diagram for $^1\Pi$ - $^1\Sigma$ transitions with *P*, *Q*, and *R* Branches [25].

$$\upsilon_{head} - \upsilon_0 = -(B_v' + B_v'')^2/4(B_v' - B_v'') \quad (2.81)$$

For every line in the P branch of a rotationally resolved spectrum there are corresponding lines in the R branch which have either a common upper or lower rotational state. The frequency differences between these lines corresponds to a well-defined separation between rotational levels in either the upper or the lower state, which is called a combination difference, $\Delta_2 F$. Combination differences are functions of J, and in some respects are even more individual for an electronic state than molecular constants such as B_v because they can be determined and used to identify a state even when perturbations are in evidence.

Upper and lower state combination differences can be calculated from:

$$\begin{aligned} \Delta_2 F''(J) &= R(J-1) - P(J+1) \\ \Delta_2 F'(J) &= R(J) - P(J) \end{aligned} \quad (2.82)$$

As a rule, J always refers to the lower state in Eq. 2.82. A schematic illustration for $\Delta_2 F''(J)$ and $\Delta_2 F'(J)$ can be found in Fig. 2.10.

Combination differences are commonly employed in spectroscopy. As noted above they are especially useful when the upper electronic state is perturbed by a nearby electronic state since the combination differences for the rotational levels in the lower state, for example, the ground state, will be unaffected. Combination differences permit the unambiguous assignment of the absolute J values in the rotational branches, and if desired, the determination of B_v values. Another utility of combination differences is that their values are unbiased in that systematic frequency measurement errors cancel out.

2.4.6 Symmetry Properties of the Rotational Levels/Nuclear Spin

The rotational levels of a diatomic molecule are classified according to the behavior of the total eigenfunction of the molecule upon inversion. A rotational level is called positive or negative depending on whether the total eigenfunction remains unchanged or changes sign upon an inversion operation. Since vibrational eigenfunctions always remains unchanged by a reflection at the symmetry origin, only electronic and rotational eigenfunctions need to be considered In the case of Σ^+ states (which are the

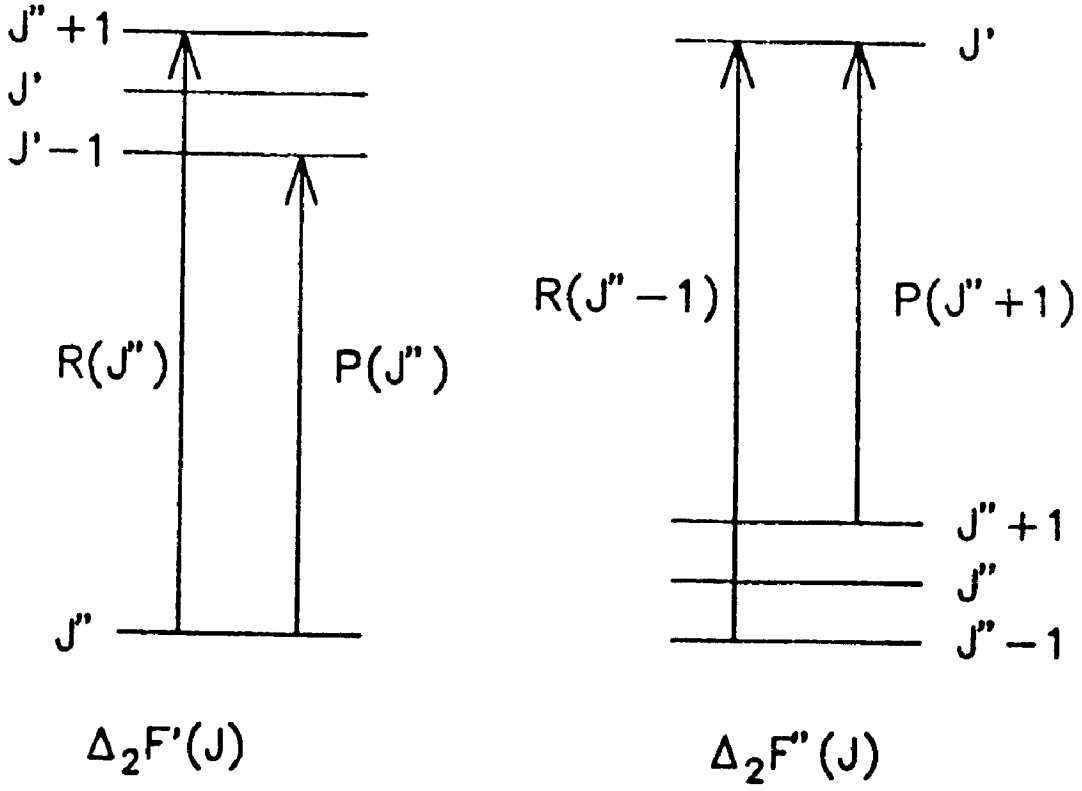

Fig. 2.10 An energy level diagram illustrates the combination differences.

type considered in this thesis), the parity of the total eigenfunction depends only on the rotational eigenfunction, that is, rotational levels are positive when J is even, or negative, if J is odd. Here positive levels will be indicated by $\oplus$ and negative levels by $\ominus$ [25].

In the case of a symmetric top where $\Lambda \neq 0$, there is a positive and a negative rotational level of equal energy for each value of J corresponding to the double degeneracy of $\Lambda > 0$ states noted above. An energy splitting between the parity levels will occur, however, when the interaction of electronic motion and rotation is taken into account (Λ-doubling).

An important selection rule holds for single-photon allowed electronic dipole transitions. Positive levels combine only with negative, and vice versa, or symbolically: $\oplus \leftrightarrow \ominus$ This selection rule does not violate the rotational selection rule $\Delta J = 0, \pm 1$ discussed previously.

For homonuclear molecules, an additional symmetry operation corresponding to the exchange of identical nuclei has to be considered. The rules for labeling the symmetry property of the rotational levels within an electronic state are:

$$(g) \times \oplus = s, \quad (g) \times \ominus = a, \tag{2.83}$$

$$(u) \times \oplus = a, \quad (u) \times \ominus = s \tag{2.84}$$

where s stands for symmetric, a refers to antisymmetric. Therefore, for a Σ_g^+ state, the positive rotational levels are symmetric while the negative levels are antisymmetric. Conversely, for a Σ_u^+ state, positive levels are antisymmetric while negative levels are symmetric. As shown in Fig. 2.11, the transitions between rotational levels in a ${}^1\Sigma_u^+ \leftarrow {}^1\Sigma_g^+$ transition are only permitted for $s \leftrightarrow s$ and $a \leftrightarrow a$.

When nuclear spin is considered, however, the selection rule $s \not\leftrightarrow a$ no longer holds absolutely. Although both symmetric and antisymmetric terms can participate in electronic transitions, their intensities are determined by their different statistical weights. Qualitatively, this phenomenon can be understood by the fact that an exchange of identical nuclei with nuclear spin does not necessarily lead to a completely identical state since the

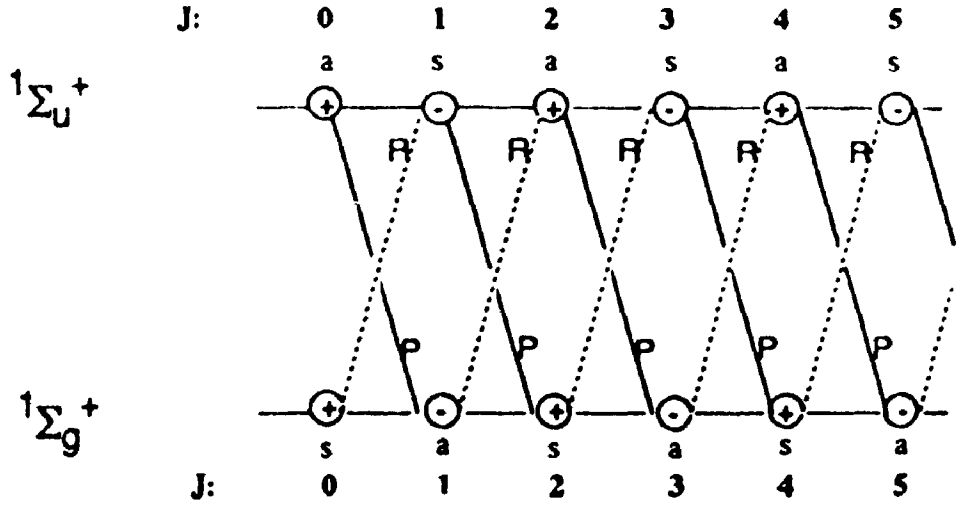

Fig. 2.11 A $^1\Sigma_u^+ \leftarrow ^1\Sigma_g^+$ transition [25].

nuclei may still differ by the orientation of their spins.

If the nuclear angular momentum (nuclear spin), I, is zero, only half the lines of any given branch is observed in an electronic spectrum. On the other hand, when $I > 0$, for example in the case of Cl_2, all lines in a branch will be present, but their intensities depend markedly on whether J is even or odd. This phenomenon is referred to as an intensity alternation.

If the two identical nuclei of a diatomic molecule have spin $I_1 = I_2 = I$, the resultant total nuclear spin T can be obtained by vector addition:

$$T = 2I,\ 2I - 1, \ldots, 0. \tag{2.85}$$

From the theory of angular momentum, the statistical weight for a state with a given T is $2T + 1$. The statistical weights of the symmetric and antisymmetric rotational levels are obtained by adding separately the quantities $2T + 1$ for even and odd T.

If the atoms in the molecule are bosons; that is, they have integer nuclear spins, the overall wavefunction must be symmetric with respect to exchange of identical particles. On the other hand, if the atoms are fermions; that is, they have half integer spins, the total wavefunction must be antisymmetric with respect to such an interchange. Consider the case when $I = 3/2$, which is the nuclear spin of ^{35}Cl and ^{37}Cl. The resultant spin T is given by

$$T = 3, 2, 1, 0. \tag{2.86}$$

In a magnetic field the $2T + 1$ levels of slightly different energy that split out, are distinguished by different values of M_T, the quantum number of the component of T in the field direction For

$$T = 3, \qquad M_T = +3, +2, +1, 0, -1, -2, -3; \tag{2.87}$$

$$T = 2, \qquad M_T = +2, +1, 0, -1, -2; \tag{2.88}$$

$$T = 1, \qquad M_T = +1, 0, -1, \tag{2.89}$$

$$T = 0, \qquad M_T = 0. \tag{2.90}$$

Although T is not defined,

$$M_T = M_{I_1} + M_{I_2}. \tag{2.91}$$

where $M_{I_1} = M_{I_2} = +3/2, +1/2, -1/2, -3/2$ since $I_1 = I_2 = 3/2$. The total eigenfunctions representing the nuclear spin states, β, may be expressed as products of two functions β_1 and β_2 of the two spins. The sixteen spin eigenfunctions β are

$$
\begin{aligned}
&(1)\ \beta_1^{3}\beta_2^{3}, \quad \beta_1^{1}\beta_2^{1}, \quad \beta_1^{1}\beta_2^{1}, \quad \beta_1^{3}\beta_2^{3};\\
&(2)\ \beta_1^{3}\beta_2^{1}, \quad \beta_1^{1}\beta_2^{3},\\
&(3)\ \beta_1^{3}\beta_2^{1}, \quad \beta_1^{1}\beta_2^{3},\\
&(4)\ \beta_1^{3}\beta_2^{3}, \quad \beta_1^{3}\beta_2^{3};\\
&(5)\ \beta_1^{1}\beta_2^{1}, \quad \beta_1^{1}\beta_2^{1};\\
&(6)\ \beta_1^{1}\beta_2^{3}, \quad \beta_1^{3}\beta_2^{1};\\
&(7)\ \beta_1^{1}\beta_2^{3}, \quad \beta_1^{3}\beta_2^{1};
\end{aligned}
\qquad (2\ 92)
$$

where the superscripts indicate the values of M_{I_1} and M_{I_2}. The first four functions in (1) are symmetric with respect to an exchange of the two identical nuclei. The remaining twelve functions ((2) to (7)) occur in degenerate pairs. The degeneracy is removed, however, when the interaction of the spins is taken into account. The resultant eigenfunctions to zeroth-order are:

$$
\begin{aligned}
&(2a)\ \beta_1^{3}\beta_2^{1} + \beta_1^{1}\beta_2^{3}, \qquad (2b)\ \beta_1^{3}\beta_2^{1} - \beta_1^{1}\beta_2^{3},\\
&(3a)\ \beta_1^{3}\beta_2^{1} + \beta_1^{1}\beta_2^{3}, \qquad (3b)\ \beta_1^{3}\beta_2^{1} - \beta_1^{1}\beta_2^{3},\\
&(4a)\ \beta_1^{3}\beta_2^{3} + \beta_1^{3}\beta_2^{3}, \qquad (4b)\ \beta_1^{3}\beta_2^{3} - \beta_1^{3}\beta_2^{3},\\
&(5a)\ \beta_1^{1}\beta_2^{1} + \beta_1^{1}\beta_2^{1}, \qquad (5b)\ \beta_1^{1}\beta_2^{1} - \beta_1^{1}\beta_2^{1},\\
&(6a)\ \beta_1^{1}\beta_2^{3} + \beta_1^{3}\beta_2^{1}, \qquad (6b)\ \beta_1^{1}\beta_2^{3} - \beta_1^{3}\beta_2^{1},\\
&(7a)\ \beta_1^{1}\beta_2^{3} + \beta_1^{3}\beta_2^{1}, \qquad (7b)\ \beta_1^{1}\beta_2^{3} - \beta_1^{3}\beta_2^{1}
\end{aligned}
\qquad (2\ 93)
$$

The spin eigenfunctions (1, 2a - 7a) are symmetric while spin eigenfunctions (2b - 7b) are antisymmetric. In the case of Cl_2, the overall eigenfunction must be antisymmetric. Consequently, the ten symmetric nuclear spin eigenfunctions combine with antisymmetric rotational levels (odd J), while the six antisymmetric functions are associated with symmetric rotational levels (even J). Since the ratio of the statistical weights is 10:6 = 5:3, the antisymmetric rotational levels occur 5/3 times as frequently as the symmetric. Experimentally, this means that the odd J levels will be 5/3 more intense than the even J levels for $^{35}Cl_2$ and $^{37}Cl_2$.

2.4.7 Dunham Expansions

Dunham calculated the energy levels of a vibrating rotator within any potential energy curve which can be expanded as a power series in $(r - r_e)$ in the neighborhood of the potential minimum. In this case, the term values of the energy levels, F_{vJ}, can be written in the form

$$F_{vJ} = \sum_{l,j} Y_{lj}\left(v + \frac{1}{2}\right)^{l} J^{j}(J+1)^{j} \qquad (2.94)$$

where l and j are summation indices, v and J are vibrational and rotational quantum numbers, and Y_{ij} are the Dunham coefficients. In general, the equilibrium rotational constant, B_e, is much smaller than ω_e. In this case, the set $\{Y_{ij}\}$ can be related to the well-known molecular constants as follows:

$$Y_{10} \approx \omega_e \qquad Y_{20} \approx -\omega_e x_e \qquad Y_{30} \approx \omega_e y_e$$

$$Y_{01} \approx B_e \qquad Y_{02} \approx -D_e \qquad Y_{03} \approx H_e$$

etc.

2.4.8 Isotope Effects

Many atomic elements have different naturally occurring isotopes with different masses. Diatomic isotopic molecules, or isotopomers, are made up from these different isotopes

The potential energy functions for two isotopomers are basically the same to a high degree of approximation since they depend only on the motions of the electrons and the Coulomb repulsion of the two nuclei [25]. In general, the mass differences influence only the energies of vibrational and rotational levels within each electronic state, which is not unexpected given that the vibrational and rotational constants explicitly depend on the mass of the isotopomer.

To relate the vibrational and rotational energy shifts of one isotopomer to another, usually the most abundant isotopomer with reduced mass μ is selected to be the reference. Another other isotopomer with reduced mass μ_i are connected to the reference through the parameter ρ_i, where

$$\rho_i = \sqrt{\frac{\mu}{\mu_i}}. \tag{2.95}$$

With these values of ρ_i the vibrational and rotational constants for the reference isotopomer can be scaled to obtain molecular constants for the other isotopomers. Ordinarily, molecular constants decrease with increasing isotopomer mass If the isotopomer of the interest is heavier than the reference, then $\rho_i < 1$. Consequently, vibrational and rotational levels for the heavier isotopomer will lie lower in energy than those of the reference species inside the potential energy curve. The opposite is expected for the lighter isotopomers.

Term values belonging to different isotopomers can be fitted together using a mass-reduced Dunham expansion which incorporates ρ_i factors:

$$F_{vJ} = \sum_{i,j} Y_{ij} \left[\rho_i \left(\upsilon + \frac{1}{2} \right) \right]^i \left[\rho^2 J(J+1) \right]^j \tag{2.96}$$

However, if the band system is perturbed Dunham expansions may fail. When this happens different isotopomer bands can be fitted on an individual basis

2.5 References

1 P. A. Franken, A.E Hill, C. W. Peters, and G. Weinreich, *Phys. Rev. Lett.*, **7**, 118 (1961).

2 P. D. Maker, R.W Terhune, and C. M. Savage, *Phys. Rev.*, **137**, A801 (1965).

3. G. H. C. New and J. F. Ward, *Phys. Rev. Lett.*, **19**, 556 (1967).

4. S E. Harris and R.B. Miles: *Appl. Phys. Lett* , **19**, 385 (1971).

5. D. M Bloom, J. T. Yardley, J. F. Young, S. E. Harris, *Appl. Phys. Lett.*, **24**, 427 (1974).

6 R. T. Hodgson, P. P. Sorokin, and J. J. Wynne, *Phys. Rev. Lett.*, **32**, 343 (1974).

7. Carl R. Vidal, **Tunable Lasers**, edited by L.F. Mollenauer and J. C. White.

8. W. Jamroz and B. P. Stoicheff, *Progress in Optics* **XX**, 327 edited by E. Wolf, North-Holland, Amsterdam. (1983).

9. B. B. Laud, **Lasers and Non-linear Optics**, 2nd ed., John Wiley & Sons, New York (1991).

10. Gary C. Bjorklund, *IEEE J. Quantum Electron.*, **QE-11**, 287 (1975).

11. J. Hager and S. C. Wallace, *Chem. Phys. Lett.*, **90**, 472 (1982).

12. R. Mahon, T. J. Mcilrath, V. P. Myerscough, and D. W. Koopman, *IEEE J. Quantum Electron.*, **QE-15**, 444 (1979).

13. J. Bokor, R. R. Freeman, R. L. Panock, and J. C. White, *Opt. Lett.*, **6**, 182 (1981);
P. R. Herman and B. P. Stoicheff, *Opt. Lett.*, **10**, 502 (1985);
P. R. Herman, P. E. LaRocque, R. H. Lipson, W. Jamroz, and B. P. Stoicheff, *Can. J. Phys.*, **63**, 1581 (1985).

14. A. Kantrowitz and J. Grey, *Rev. Sci. Instrum.*, **22**, 328 (1951).

15. R. E. Smalley, L. Wharton, and D. H. Levy, *Acc. Chem. Res.*, **10**, 139 (1977).

16 R. H. Lipson, Ph. D thesis, University of Toronto (1985).

17. E. Becker, **Gas Dynamics**, Academic Press, New York, N. Y., 1968.

18 J. B. Anderson and J. B. Fenn, *Phys. Fluids*, **8**, 780 (1965);
R. A. Oman, A. Bogan, C. H. Weiser, and C. H. Li, Research Department, Grumman Aircraft Engineering Co., Report RE-166, 1963.

19. R. Campargue, *J. Chem. Phys.*, **52**, 1795 (1969).

20. H. Ashkenas and F. S. Sherman, **Rarefied Gas Dynamics**, Vol. **2**, ed by J. H Leeuw, Academic Press Inc., New York, 1966.

21 W. C. Wiley and I. H. Mclaren, *Rev. Sci. Instruments*, **26**, 1150 (1955).

22. R. A. Alberty, **Physical Chemistry**, 7-th ed., John Wiley & Sons (1987).

23. C. H. Townes and A. L. Schawlow, **Microwave Spectroscopy**, Dover Publications Inc., New York (1975).

24. J. Michael Hollas, **Modern Spectroscopy**, John Wiley & Sons (1986).

25. Gerhard Herzberg, **Molecular Spectra and Molecular Structure**, I. Spectra of Diatomic Molecules, 2nd edition, Van Nostrand Reinhold Co (1950).

26. P. W. Atkins, **Physical Chemistry**, 4-th edition, W. H. Freeman and Company, New York (1990).

Chapter 3

Experimental

3.1 An Overview of the Experimental Apparatus and Procedure

A new VUV "laser" time-of-flight (TOF) mass spectrometer was built in 1993 to record single isotopomer spectra in the VUV and the XUV spectral regions. The experimental apparatus was designed to combine the techniques of two-photon resonantly enhanced four-wave mixing (FWM), linear time-of-flight mass spectrometry, and supersonic jet cooling to record vibrationally and rotationally resolved spectra of small molecules such as bromine monochloride, BrCl, and chlorine, Cl_2.

A schematic of the apparatus used to record the VUV laser TOF spectra presented in this thesis is shown in Fig. 3.1. Briefly, tunable, coherent, and monochromatic VUV laser radiation having output wavelengths necessary to excite BrCl and Cl_2, was generated by the nonlinear optical technique of two-photon resonantly enhanced four-wave difference mixing (FWDM) in Kr gas. A tripled neodymium: yttrium aluminum garnet (Nd: YAG) laser (Spectra-Physics GCR-4) with a 355 nm optical output operating at a 10 Hz repetition rate was used to pump two dye lasers (Lumonics HD-500 and HD-300), hereafter labeled υ_1 and υ_2, respectively. Typically, both dye lasers generated ≈ 10 mJ of energy in a 4 ns pulse. The frequency bandwidth of the υ_1 dye laser, $\Delta\upsilon_1$, was ≈ 0.04 cm^{-1} while $\Delta\upsilon_2$ was ≈ 0.07 cm^{-1}. The output of the υ_1 dye laser was frequency doubled in a beta-barium borate (BBO) crystal (A cut, Inrad Autotracker II) to produce ultraviolet, UV radiation at $\omega_1 = 2\upsilon_1$, which was two-photon resonant with the appropriate transition of the nonlinear medium. The UV and υ_2 outputs were focused into a cell containing the nonlinear medium Kr. As the υ_2 dye laser was scanned, tunable VUV radiation at the difference frequency $4\upsilon_1 - \upsilon_2$ was generated. The frequency of the υ_2 dye laser was calibrated by using a small portion of its output to

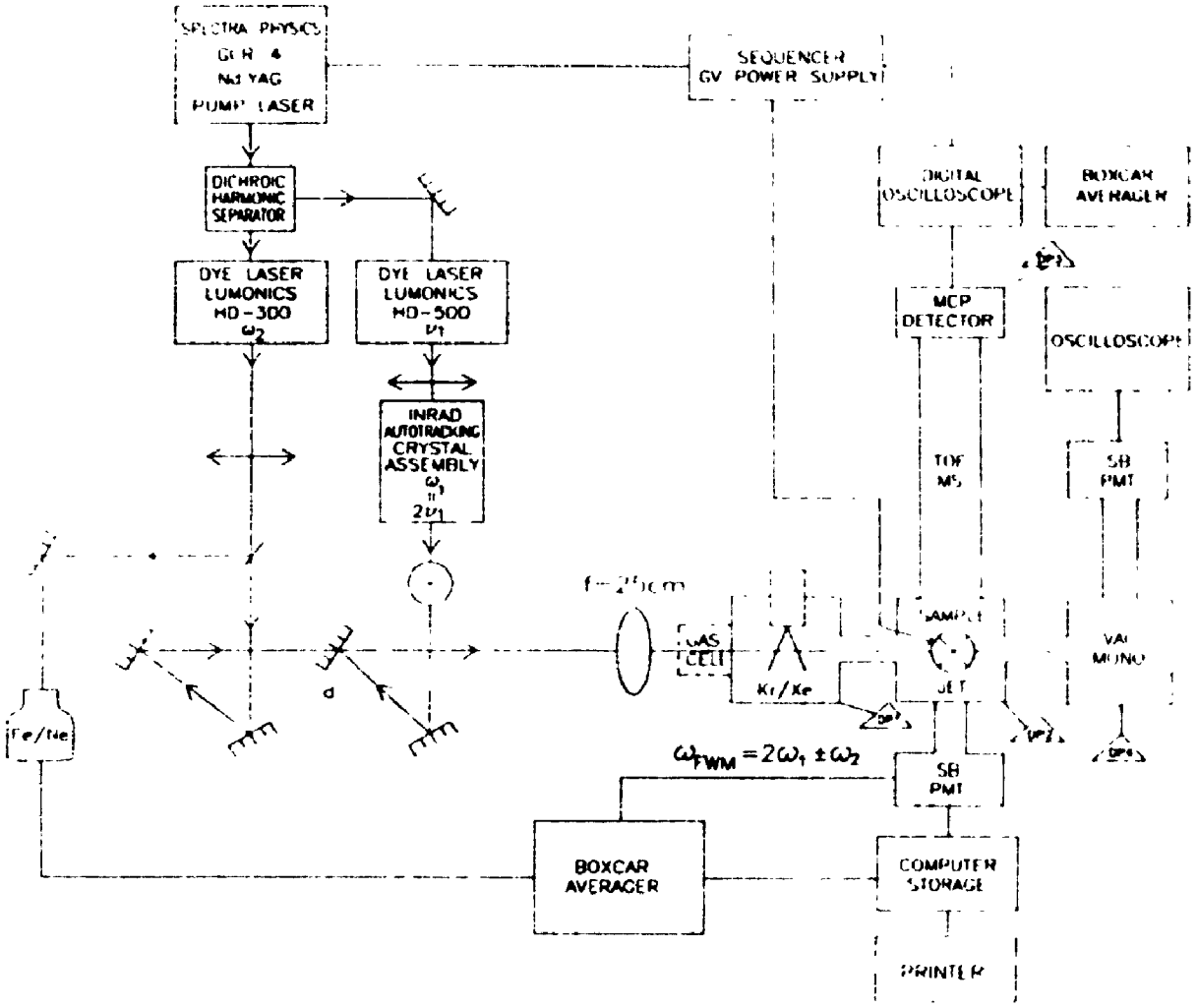

Fig. 3.1 The schematic of the apparatus used for the experiments of BrCl and Cl_2

excite the optogalvanic (OG) spectrum of neon in an Fe/Ne hollow cathode lamp (1st Imaging & Sensing Technology, model WL 22810). The beams were spatially overlapped for the FWM process using dichroic mirrors which also provided beam steering.

The generated VUV pulses, divergently exiting the Kr gas cell through a LiF window, entered a differentially pumped vacuum chamber housing the pulsed valve (General Valve Corporation, 9-181-901) which produced the cold supersonic jet. Photoions, produced in the jet by a (1+1) resonantly enhanced multiphoton ionization (REMPI) process involving both the VUV and fundamental beams, were accelerated by grids biased by positive voltage into a field-free 1.01 m long flight tube of a commercial TOF mass spectrometer (Comstock Inc., model TOF-101), and detected at the end of the flight tube with a dual microchannel plate (MCP, Galileo Electro-Optics Co.) detector. The VUV laser induced fluorescence (LIF) was monitored at the same time with a solar-blind photomultiplier (EMR 541G-08-17) mounted on a flange located 180^0 to the flight tube. In order to record laser-induced fluorescence and REMPI/TOF excitation spectra at the same time, the center of the back repeller plate was replaced with a fine copper mesh (0.875 inch diameter, 70 lines/inch. ≈ 90% optical transmission). Scattered light into the photocathode was reduced using light baffles (black Delrin) placed around the phototube and the path of the laser beams. A lithium fluoride (LiF) flat (1 inch diameter, 1 mm thick) was mounted on the front of the photomultiplier housing to prevent damage to the window covering the cathode from high energy electrons produced in the (1+1) REMPI process. In general, an (n + m) REMPI process means that n photons are used to excite a molecule to an intermediate rovibronic state, while m photons ionize the molecule from that intermediate level. This technique is widely used in molecular spectroscopy primarily because high energy states can be accessed using relatively low energy photons. However, the laser employed must be intense enough, and the chosen intermediate state must be sufficiently long-lived to excite a REMPI transition.

The generated VUV laser output was monitored continuously during an experiment by dispersing the unused radiation after the jet chamber in a vacuum

monochromator (Macpherson, model 218) and detecting the light with second solar-blind photomultiplier located at the exit slit.

OG calibration spectra were recorded at the same time as the LIF and the single isotopomer REMPI/TOF spectra. Since the frequency υ_1 was fixed for a FWM experiment its calibration was achieved in separate experiments by recording the well known spectrum of carbon monoxide (CO) [1].

TOF signals from the MCP detector were displayed on a digital storage oscilloscope (LeCroy ScopeStation-140) to ensure that the Wiley-Mclaren space-focusing conditions were fulfilled. Signals from the microchannel plate detector, the LIF solar-blind photomultiplier for LIF, and the optogalvanic wavemeter were processed individually in gated integrators/boxcar averagers (Stanford Research Systems, SR 250), digitized, and stored in an AT computer for later analysis.

Our experimental system has XUV generation capabilities for wavelengths shorter than 105 nm where no broadly transmitting and reflecting optics are available. XUV radiation by four-wave sum-mixing can be produced in the first six-arm vacuum chamber (MDC, 4.5 inch Conflat), hereafter named the XUV chamber, which was diffentially pumped by a 100 mm diameter Edwards Diffstak diffusion pump backed with a two-stage mechanical pump (Edwards, E2M18). This diffusion pump, like the three others on the entire vacuum system, was operated with Santovac 5 pump oil to reduce vapor backstreaming. As a result, liquid nitrogen traps were found to be unnecessary. The XUV chamber was attached to the main chamber housing the TOF mass spectrometer (Fig. 3.1).

The nonlinear medium (Xe or Kr gas) was delivered inside the chamber using a pulsed valve (Laser Technics Model LPV) mounted to the top flange of the chamber. The entire vacuum system was maintained at a base pressure of $\leq 10^{-6}$ Torr. Since a supersonic jet can be viewed as a spatially localized gas sample, the entire vacuum system under these conditions becomes windowless with effective differential pumping. As a result, the generated XUV light is free to propagate from one region to another without being absorbed. While this technique is also possible for VUV generation in

these experiments, the longer wavelength light was generated in a gas cell attached to the XUV chamber, to conserve the expensive rare gas.

Two investigations were carried out, one for BrCl and the other for Cl_2. Since both were run in a very similar manner, only a detailed description will be given for BrCl work. This will be followed by a very brief discussion of the changes required to study Cl_2.

3.2 Experiments of BrCl

3.2.1 BrCl Sample Preparation

Different percentage compositions of Br_2 and Cl_2 were tried to produce enough BrCl for the experiment by the reaction of $Br_2 + Cl_2 \Leftrightarrow 2\ BrCl$ having an equilibrium constant, $K_{eq} \approx 6.5$ at room temperature[2]. The gas-handling system shown schematically in Fig. 3.2 consists of a stainless steel cylinder which could be evacuated to ≈ 1 mTorr using a mechanical pump (Welch Scientific Co., model 1400). An absolute pressure gauge (Matheson, part No. 63-5601, 0 - 760 Torr) was used to measure the pressures of the constituent gases below 760 Torr (Br_2), while the second pressure gauge (Matheson, part No. 63-5652, 0 - 550 psig) was installed to measure higher gas pressures (> 760 Torr, Cl_2) and the total pressure after adding the He buffer gas. As soon as the gas mixture was made, the stainless steel cylinder was isolated and the rest of the system was flushed with He and pumped out, since Br_2 and Cl_2 are corrosive. An in-line regulator (Matheson, part No. 63-2208, 0 - 300 psi) was also used to maintain a constant gas pressure inside the nozzle valve. The best sample was prepared by mixing the Br_2 vapor at room temperature (20°C, ≈ 180 Torr), with 1280 Torr Cl_2. The mixture was then diluted in 520 Torr (10 psia) He for a total pressure of ≈ 34 psia. The gas mixture equilibrated completely after about two hours, and could be used for a couple of days before another mixture was needed.

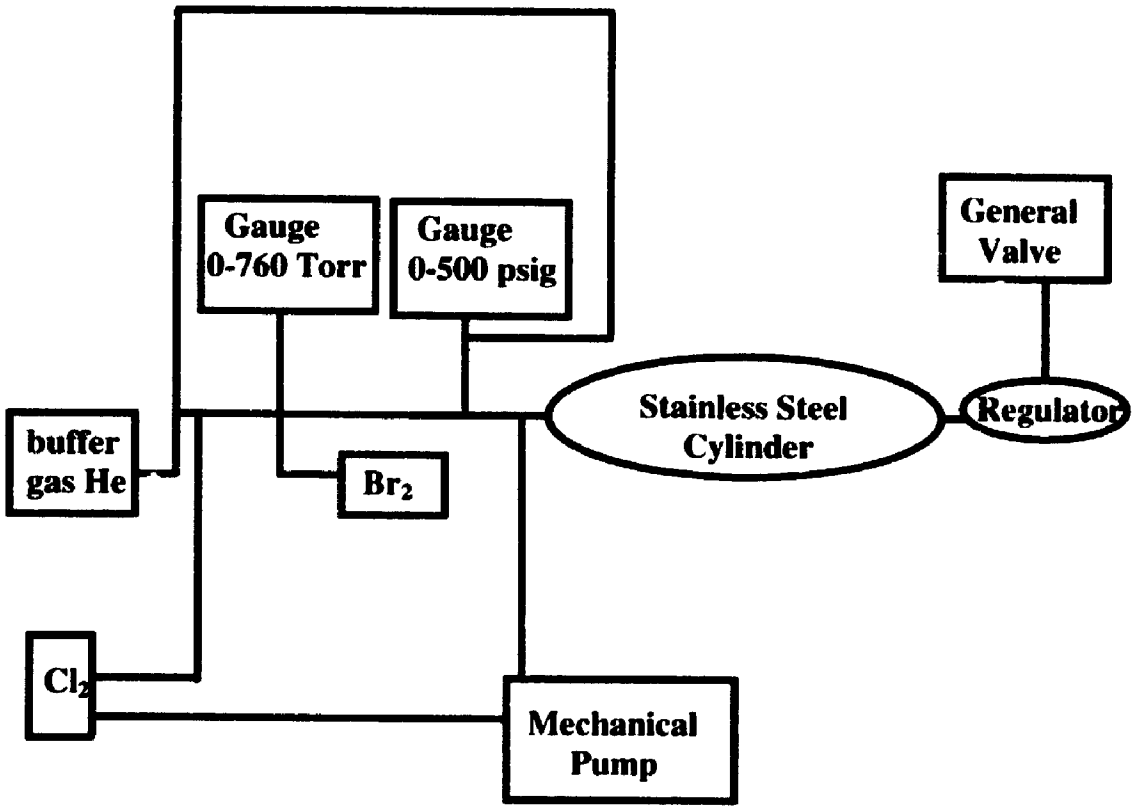

Fig. 3.2. A schematic of the homemade gas handling system

3.2.2 VUV Generation and Calibration

(a) Pump laser

A pulsed Nd: YAG laser (Spectra-Physics, GCR-4), was used to pump two dye lasers. YAG is an acronym for yttrium aluminum garnet, $Y_2Al_5O_{12}$. The lasing ion, Nd^{3+}, which has replaced ≈ 1% the Y^{3+} ions in the matrix, produces stimulated emission at $\lambda \approx 1.064$ μm in the infrared (IR) spectral region. Since the population inversion in the GCR-4 was produced by long pulse duration flash lamps ($\tau \approx$ 3-50 μsec.) having outputs in the visible and IR, higher laser peak powers per pulse was achieved by Q-switching. The laser, with an oscillator and one amplifier, had outputs in the IR as high as 1 joule over 4 ns, corresponding to 250 MW peak power. The timing between the trigger pulses for the flash lamp and the Q-switch, called the Q-switch delay, could be controlled either by internal or external electronics.

The wavelength of the fundamental infrared laser pulse is too long to pump visible dye lasers. However, frequency upconversion by second harmonic generation (SHG) in nonlinear crystals such as potassium dideuterium phosphate (KD^*P) is efficient. This process yields green light at λ = 532 nm. UV pulses at λ = 355 nm used in this work could also be generated by mixing the 532 nm light with the residual 1064 nm fundamental in a second KD^*P crystal. The UV, green, and IR pulses were separated from one another using a set of dichroic mirrors (Spectra Physics, DHS-2) placed between the Nd: YAG laser and the dye lasers. The total UV peak power used to pump the two dye lasers was typically 38 MW, when measured before the dichroic mirrors with a thermocouple powermeter (Scientech Boulder Co., model 380101). About 60% of the power was used to pump the υ_1 dye laser while the rest was used to pump υ_2.

(b) Dye lasers

Pulsed dye lasers have found their great applicability in laser spectroscopy mainly due to their extensive wavelength tuning ranges. The active media are organic dye solutions which usually have strong absorption bands in the UV or visible regions of the spectrum. The two dye lasers employed in these experiments, Lumonics HD-500 and HD-300, are both basically grazing incidence configuration devices [3] but as the HD-500

has a longer grating, it produces an output with a narrower spectral linewidth, ≈ 0.04 cm $^{-1}$, compared to ≈ 0.07 cm^{-1} for the HD-300. In addition to an oscillator inside their cavities, both dye lasers have a single amplifier stage, and the necessary optics for pump beam steering. The wavelength scanning and selection is microprocessor controlled. The polarization of the output of both dye lasers is > 95% vertical, and their wavelength tuning range is ≈ 390 - 700 nm [4].

In general, the output powers of a dye laser depend mainly on the efficiencies of dyes used. VUV generation near 145 nm, required both dye laser to be operating on a Stilbene 420/Methanol solution (Exciton, 04200, 112mg/liter). With UV pumping, the conversion efficiency ranged from 12% to 15% for both dye lasers. Although the linewidth under identical pumping condition could be narrowed by changing the order of the diffraction grating from first to second, the output power of the laser was subsequently reduced by ≈ 10-15%.

(c) Optical arrangement after the dye lasers

In the experiments described in this thesis, the wavelength of υ_1 dye laser fixed at $\lambda \approx$ 433.4 nm, was frequency doubled in a BBO crystal (A cut) installed in an autotracking assembly (Inrad, Autotracker), to produce UV at $\lambda \approx$ 216.7 nm, which is two-photon resonant with the $4p^5 5p\ [2\frac{1}{2}]_2 \leftarrow 4p^6\ ^1S_0$ transition of atomic Kr at 92307.4393 cm^{-1} (Fig 3.3) [5]. Even though the dye laser was not pumped by the full output of the Nd: YAG laser, the lifetime of Stilbene 420 was short (≈ 1 day). A dye solution was replaced when the monitor signals on the electronic control unit of the Autotracker assembly dropped significantly.

The output of second dye laser, υ_2, tuned between 22456 cm^{-1} and 24140 cm^{-1}, was calibrated by splitting a small portion of its output (≈ 4%) to excite the optogalvanic spectrum of neon atoms in an Fe/Ne hollow cathode lamp (1st Imaging & Sensing Technology WL 22810). The lamp discharge (≈ 14 mA) was struck using a commercial high voltage power supply (Fluke, 415 B). As the frequency of the laser was scanned, any transitions of neon excited by the optical radiation changed the ionization rate in the hollow-cathode lamp. The well-known spectrum of neon [6] could therefore be obtained

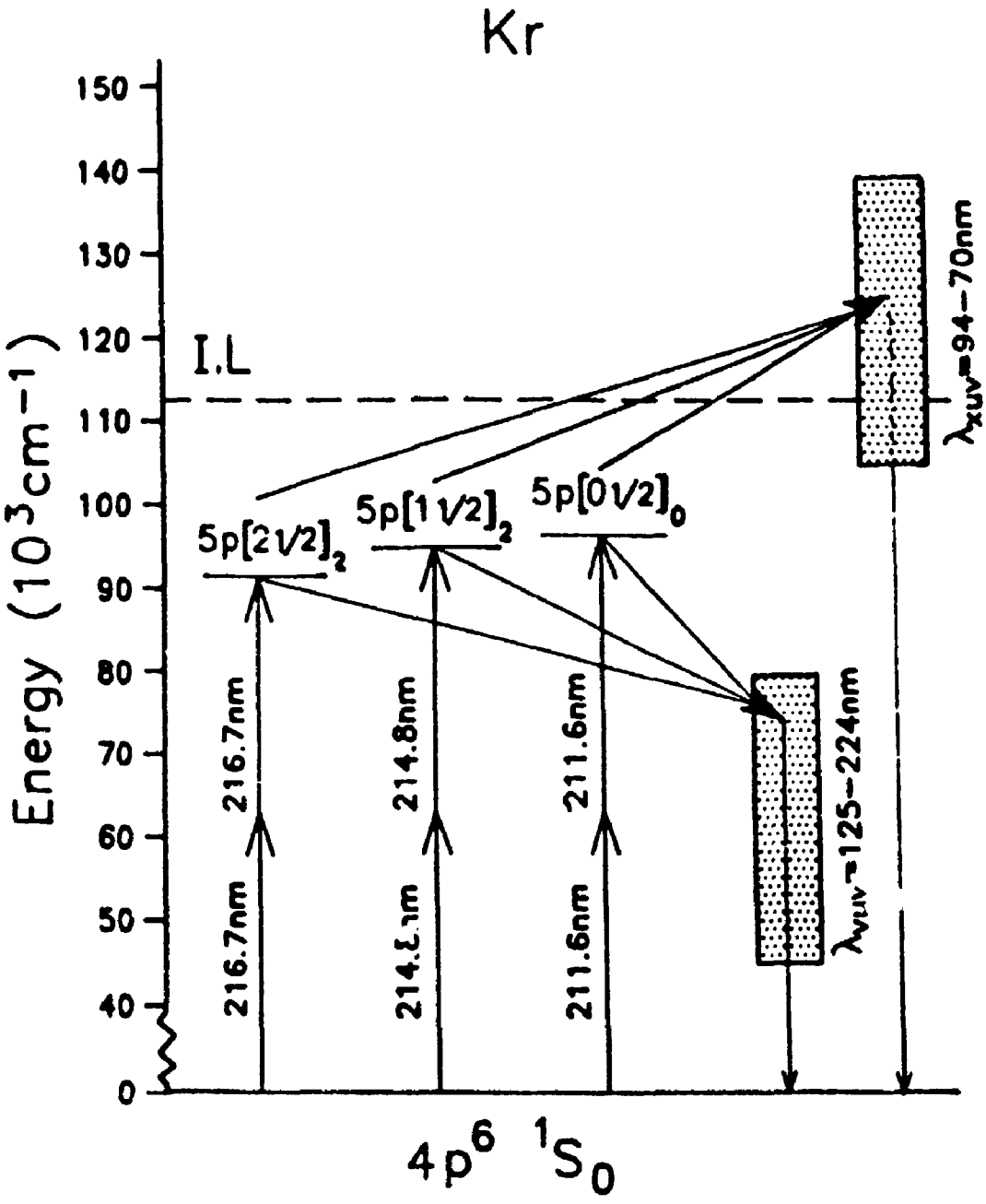

Fig. 3.3 Energy level diagrams illustrating the useful two-photon resonances of Kr, the nonlinear medium in the four-wave mixing process

by measuring the change in lamp current across a ballart resistor limiting the current in the lamp as a function of laser frequency. The OG signals were processed by a gated integrator/boxcar averager (Stanford Research Systems, SR 250) and displayed with the VUV/TOF and LIF spectra simultaneously on the output of a three-pen chart recorder (Graphtec Co., Servocorder SR6221-3L) during an experiment.

The known Ne line frequencies in the resultant OG spectra were initially determined by measuring the spacings between the lines on the chart paper after assigning a couple of the features by trial and error. In this way, the frequency scale of the unknown LIF and TOF spectra, could be determined to a relative precision of ≈ 0.1 cm^{-1}. An OG spectrum with the highest signal-to-noise ratio was achieved by limiting the amount of laser light inside the lamp with an aperture, and by properly aligning the beam onto the center of cathode. This minimized the noise due to photoelectrons produced if the light struck the lamp electrodes.

Absolute frequency accuracy requires knowing υ_1. To this end, the well-known LIF spectra of CO A $^1\Pi$ (v' = 3) $\leftarrow$ $X\ ^1\Sigma^+$ (v'' = 0) were recorded in the region from 69030 cm^{-1} to 68858 cm^{-1} in separate experiments [1]. The exact frequency of υ_1 was determined by calculating the differences between the known frequencies of the rotationally resolved spectra, and those obtained using OG calibration and the literature value of the two-photon resonance [5]. The differences were attributed to the uncertainty in knowning the exact frequency ($4\upsilon_1$) which optimized the FWM process under our experimental conditions.

The frequency doubled dye-laser output at $2\upsilon_1$ was separated from the residual visible dye laser output on one dichroic mirror, and overlapped with the υ_2 beam with a second dichroic flat. Both mirrors were located on an optical table in front of the dye lasers (Fig. 3.1). Both υ_1 and υ_2 were focused into the gas cell containing the nonlinear medium Kr with a lens (f = 25 cm). Although the XUV chamber was not used in the thesis experiments for short wavelength generation, a set of stainless steel plates mounted just below the pinhole of the Laser Technics valve was useful for finding the two-photon resonance by a (2+1) REMPI process in a Kr jet. Experimentally, this was accomplished

by applying positive voltage (+ 300 - 800 V) to one of the two plates with a regulated dc power supply (Hewlett Packard Harrrison 6110A), while grounding the second. In this way, the electrons produced by the (2+1) REMPI could be detected as the Kr was pulsed through the nozzle. The corresponding signal was displayed on an oscilloscope (Philips, PM 3200).

Once the dye laser υ_1 was tuned to the two-photon resonance of the nonlinear medium, the optics were adjusted to overlap the two beams as completely as possible. Any VUV light having passed through the two vacuum chambers was separated from the stronger residual fundamental beams with a small vacuum monochromator (MacPherson model 218), which was evacuated by a 63 mm. diameter Edward Diffstak diffusion pump backed with a two-stage mechanical pump (Edwards, E2M18). In-line isolation valves (Nor-Cal Products, model STV-1122 CF) were placed between the XUV chamber, the main vacuum chamber, and the vacuum monochromator to allow each section of the vacuum system to be individually pumped out when not running experiments. A solarblind photomultiplier tube (EMI 541G-08-17) was mounted to a flange on the exit slit part of the vacuum monochromator to monitor the VUV signal continuously during an experiment.

The pressure of the Kr sample in the gas cell was varied to optimize the power of the VUV light. It was discovered that the highest conversion efficiency was achieved using only $\approx$ 5 Torr of nonlinear medium under our experimental conditions, rather than $\approx$ 100 Torr determined by Hilber *et al* [6]. The cell was evacuated every couple of hours and filled with a new Kr sample to minimize the amount of air in the system. In general, the conversion efficiency of FWM process is on the order of $\approx 10^{-5}$, corresponding to $\approx 10^{10}$ photons/pulse. The average power of the generated VUV radiation was several watts. For BrCl experiments, sufficiently intense VUV radiation was generated at $4\upsilon_1 - \upsilon_2$ between 68167 cm^{-1} and 69851 cm^{-1}.

3.2.3 Supersonic Jet Formation

A pulsed valve (General valve, model, 9-181-901, 0.15 mm diameter pinhole) was

mounted above the ionization region of the TOF mass spectrometer inside the six-arm main vacuum chamber (MDC, 8 inch Conflat) located next to the XUV chamber. This section of the vacuum system was evacuated by a 250 mm diameter Edward Diffstak diffusion pump, backed by a two-stage mechanical pump (Edwards, E2M18). Pulsed voltage (240 V, $\tau \approx 160$ μs) was applied to the solenoid inside the General valve with a homemade power supply. The voltage pulse to the General valve was monitored continuously on an oscilloscope (Iwatsu, SS-7610, 100 MHz). When the valve was operating, the pressure inside the chamber rose to $\leq 1 \times 10^{-5}$ Torr from its base level of $\approx 1 \times 10^{-7}$ Torr. All pressures were monitored using Penning ionization gauges (Edwards, model CP 25-EK).

A second EMR solar-blind detector was mounted onto a flange located on one of the six arms of the vacuum chamber. Its purpose was to detect the total laser induced fluorescence intensity as a function of exciting laser frequency. The commercial TOF mass spectrometer (Comstock, TOF-101) was installed to detect photoions produced by (1+1) REMPI. The ionization region of the TOF mass spectrometer, consisting of a repeller plate and a central ground plate, was located in the center of the chamber.

When the TOF mass spectrometer was initially purchased from Comstock, the distance between the plates making the ionization region was only 8 mm which is smaller than the diameter of the General valve. Similarly, the acceleration region was only 5 mm long. The spectra obtained with these spacings were found to be rotationally hot due to collisions between the jet molecules and the grids. Therefore, the dimension of the ionization and acceleration regions were increased to 21.1 mm and 24.4mm, respectively. Although this form was still small relative to the diameter of the commercial valve, by machining the faceplate of the nozzle down to the diameter of the main body (19.3 mm) and electrically insulating the entire unit in a Teflon sheath, this entire valve could be lowered into the ionization region. Rotationally cold spectra were obtained immediately when this was done. The height of the nozzle with respect to center of the ionization volume could be adjusted after the mechanical modifications, and was chosen to be 25 mm. In addition, the entire valve could be positioned over the optical axis defined by the

VUV beam by sliding the flangeholding the valve at the top of the chamber (≈ 2 - 3 mm in any direction) over a fixed o-ring.

Since the jet was not skimmed, and because the MCP detector at the end of the mass spectrometer flight tube required a vacuum ≤ 10^{-5} Torr at all time, a conductance limiting plate was inserted between the chamber and the flight tube to reduce the effective operation in the TOF arm of the chamber from "8 inches" to outer diameter of the flight tube (≈ 4.1 inch diameter). Furthemore, the MCP detector at the end of the flight tube was evacuated by its own 250 mm Edwards Diffstak diffusion pump backed by a two-stage mechanical pump (Edwards, E2M18).

In the event of a power failure or if by an accident, the pressure in the system rose to ≥ 10^{-2} Torr, gate valves (VAT, model F10-60408-58) located between the sample chamber and diffusion pump, and the MCP detector and its associated diffusion pump, were closed electrically with a switch initiated by the pressure reading (MDC, model 45) of a thermocouple Pirani gauge (Edwards, PR 10, D021-66-000).

3.2.4 TOF Mass Spectrometer

The Comstock mass spectrometer was used in this experiment to detect positive BrCl ions or daughter fragment ions produced by (1+1) REMPI. As mentioned in Chapter II, all ions which have the same mass to charge ratio acquire the identical kinetic energy inside the TOF mass spectrometer. Thus, their velocities are solely proportional to the square root of their mass under space-focusing conditions. Each ion with different mass can then be identified by its unique time-of-flight.

A schematic showing the ionization and acceleration regions of the TOF instrument, the X-Y deflection plates, ion lens, and dual microchannel plate detector is presented in Fig. 3.4. As the temporal resolution of the instrument was ultimately limited by the duration of the laser pulse (< 10 ns), ion formation and extraction could be carried out using dc-fields. Typically, the dc voltage applied to the repeller plate was ≈ + 340 V. Since the velocity vectors of the molecules in the supersonic jet (the Y axis) were perpendicular to the axis of the flight tube (the Z axis), it is possible that ions formed in the jet by (1+1) REMPI would completely miss the microchannel plate detector at the end

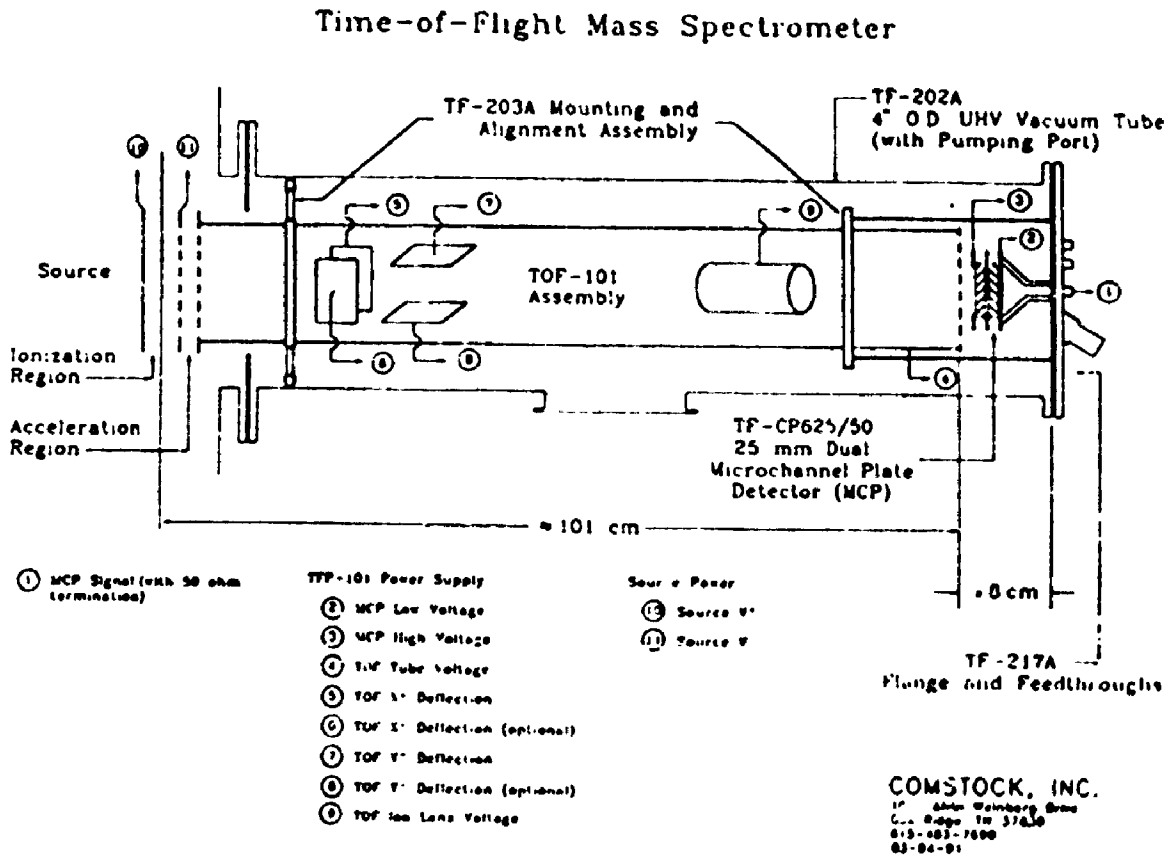

Fig 3.4. A schematic showing the ion source, X-Y deflection plates, ion lens, and a dual microchannel plate detector [8]

of the 1.01 m flight. For example, an ion with energy E_y = 1 eV, accelerated to energy E_z = 2.7 eV to reach the MCP detector at the end of flight tube of length L (1.01m), would be located off axis in the Y-direction by an amount l given by

$$l = (V_y/V_z)\, L = (E_y/E_z)^{1/2}\, L = 1.94 \text{ cm}. \qquad (3.1)$$

As a result, Y-axis deflectors were installed inside the flight tube, which in the Comstock instrument consists of two plates separated by 2.54 cm. In addition, X-axis deflectors were also provided to ensure the optimum ion transmission through the TOF mass spectrometer. Typically, ion steering was possible when their electric field strengths of ≈ 200 V/cm were applied to the X and Y deflectors. The X and Y plates are floated (± 250V) above and below the flight tube voltage, so that ions traveling along the Z axis would not gain or lose energy during the time they passed through the plates.

The ion lens located in front of the MCP focused the photoions at the end of the flight tube onto the detector. The voltage on the lens (0 - +500 V with respect to the flight tube potential) was chosen to produce an ion-image on the MCP detector which utilized the entire active area of the cathode (1.040 inch diameter).

The detector at the end of the flight tube is composed of two 4 cm diameter microchannel plates placed in tandem, and separated by a small gap (≈ 5 mm). The front surface of the first plate was biased at a few hundred volts positive potential relative to the flight tube to prevent electrons ejected from the MCP returning to the flight tube. The total voltage on the MCP pair was always kept at ≤ 2000 V for maximum stability, and to optimize the rise time and gain characteristics of the detector. The electron collection plate after the second MCP was biased at a few hundred volts more positive than the potential of the exit surface of the second MCP to ensure that the electron collection efficiency was high.

The Comstock Time-of-Flight Power Supply (Model TFP-101) provided all the voltages necessary to operate the mass spectrometer. The optimum settings was determined experimentally by monitoring the signal from MCP detector on the digital oscilloscope while adjusting one voltage at a time. Typically, for the BrCl experiments, the settings were:

Flight tube: -2710 V.

MCP detector: -1900 V.

Ion lens: ≈ +180 V.

X pair deflection plates: $X_1 \approx +100$ V, $X_2 \approx -100$ V.

Y pair deflection plates: $Y_1 \approx +190$ V, $Y_2 \approx -190$ V.

3.2.5 Timing and Signal Processing

Since the experimental system operates in a pulsed mode it is critical to synchronize all the different optical and mechanical components. To this end, a home-made electronic sequencer was built (circuit diagram, Fig. 3.5). In general, valve opening is relatively slow compared with the time required to produce a laser pulse. As a result, the valve had to be opened before the laser was fired to produce the cold jet before the VUV beam arrived inside the main vacuum chamber. The repetition rate of the experiments (10 Hz) was controlled by an internal pulse generator inside the sequencer, which in turn triggered several TTL pulses used to fire the laser and open the General valve (timing diagram, Fig. 3.6). Typically, the flash lamps of the oscillator of the Nd: YAG laser were fired ≈ 360 μs after the valve was triggered. The Q-switch was activated ≈ 200 μs after that. A small portion of the light from the Nd: YAG laser was used to illuminate the cathode of a photodiode which in turn triggered three gated integrators/boxcar averagers and the digital oscilloscope. The predelay between opening the General valve and firing the Q-switch was measured by monitoring both the General valve voltage pulse and Q-switch trigger pulse on the oscilloscope. The optimum predelay of ≈ 560 μs was established when the rotationally resolved spectra obtained exhibited as many rotational lines as possible without strong overlapping between the vibrational bands.

The digital oscilloscope (LeCroy, ScopeStation 140) proved useful for ensuring that single isotopomer spectra were obtained. As noted earlier, LIF, TOF, and OG signals were processed in a separate gated integrators/boxcar averagers. However, often TOF excitation spectra of two BrCl isotopomers or one atomic Br isotope and one BrCl

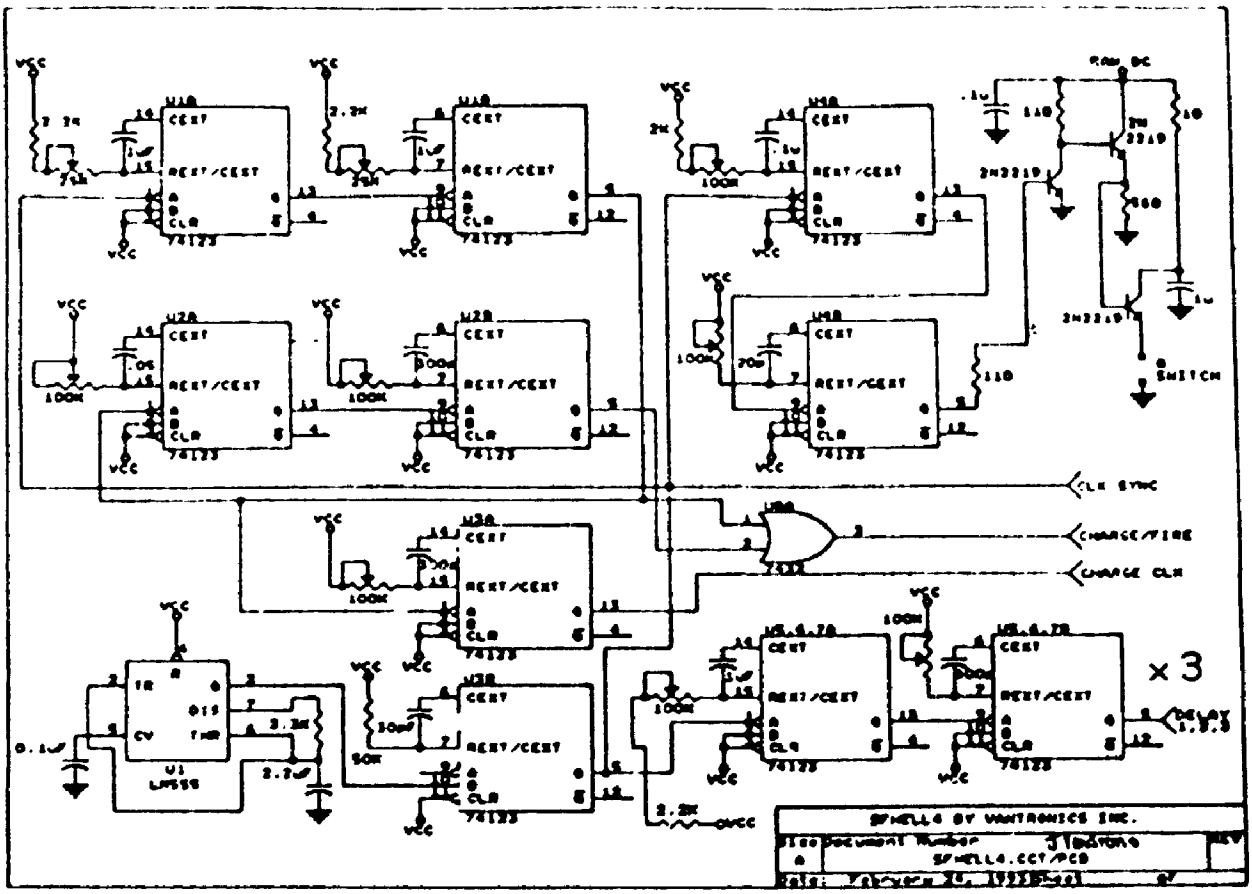

Fig. 3.5. Circuit diagram of the sequencer used to synchronize the optical and mechanical components of the system

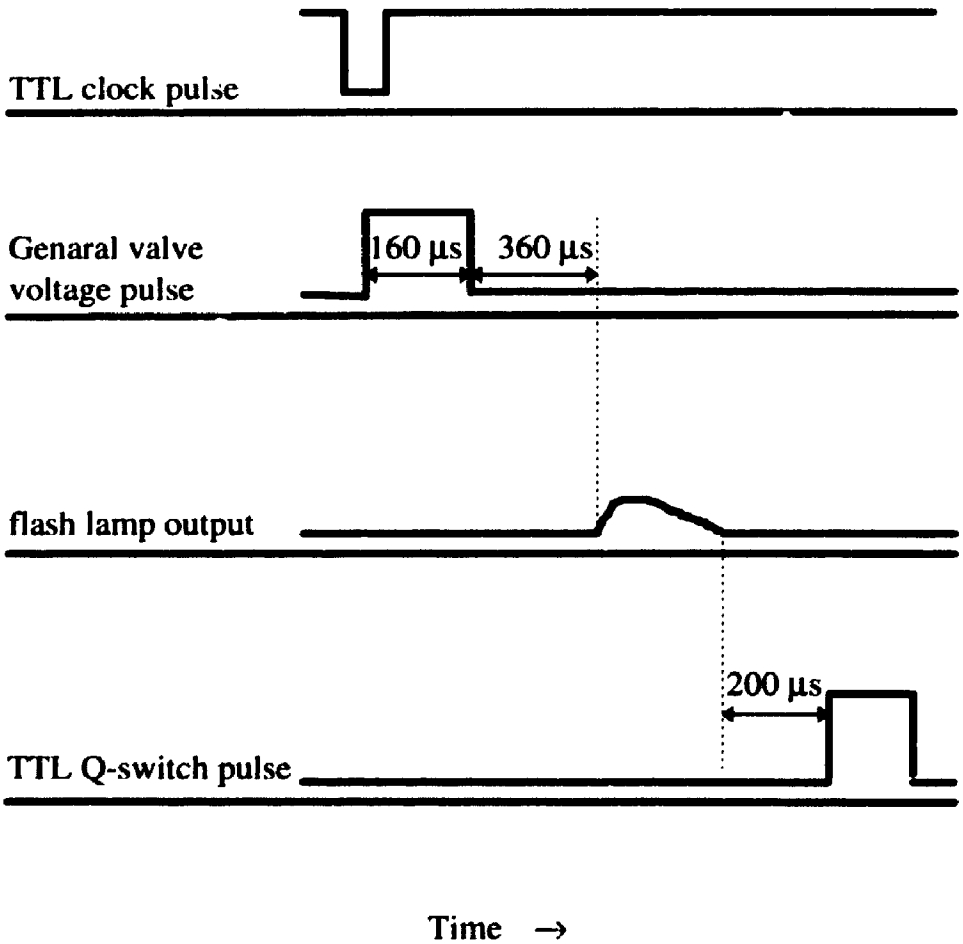

Fig. 3.6. The timing sequence for the BrCl experiments within one repetition cycle of 0.1 sec. All TTL pulses were used as edge triggers.

isotopomer were desired. Then, the width of the gate (≈ 80 ns) and gate opening relative to the boxcar trigger pulse was chosen by monitoring both the gate and the TOF mass spectrum on the digital oscilloscope. The desired spectrum was obtained by directly locating the gate in time underneath the signal of the interest on the scope. The averaged output (10 - 30 sample averaged) from each boxcar (three in total) was sent to computer through a computer interface module (Stanford Research Systems, SR 245) operated with a commercial software package (Stanford Research Systems, SR265). Originally, the spectra were recorded for each trigger pulse from the boxcar by multiple scans. However, it turned out from detailed calibrations that the data collected between scans was lost. Consequently, all spectra reported in this work were recorded for every trigger pulses n (n ranging from 3 - 5) in a signal scan over the desired frequency range.

3.3 Experiments of Cl_2

The Cl_2 experiments were carried out in a similar manner to that described above for BrCl. Briefly, tunable coherent VUV radiation was generated by FWDM in Kr gas. Excitation spectra of the $1\,^1\Sigma_u^+ \leftarrow X\,^1\Sigma_g^+$ transition near 136 nm were recorded by tuning the frequency doubled output of the ν_1 laser to the same two-photon resonance transition of Kr used for the BrCl work, $4p^5 5p\ [2\frac{1}{2}]_2 \leftarrow 4p^6\ ^1S_0$, while the output of the ν_2 laser (using Coumarin 485 dye dissolved in Methanol, 386 mg/liter) was scanned from 17637 to 19920 cm^{-1} to provide the VUV radiation at $4\nu_1 - \nu_2$ between 72387 and 74670.44 cm^{-1}. The fixed ν_1 frequency was inferred by recording the well known spectrum of the CO $A^1\Pi(v'=6) \leftarrow X^1\Sigma^+(v''=0)$ transition [1]. Excitation spectra of the $2\,^1\Sigma_u^+ \leftarrow X\,^1\Sigma_g^+$ transition near 126.4 nm required the output of the frequency doubled ν_1 dye laser to be in resonance with the $4p^5 5p\ [\frac{1}{2}]_0 \leftarrow 4p^6\ ^1S_0$ transition of Kr ($4\nu_1$ = 94092.9236 cm^{-1}) [5]. The tunable ν_2 laser was operated on either a DCM, a 1:1 LD690/DCM mixture, or a LDS698 dye solution to produce excitation frequencies between 13992 to 15992 cm^{-1}. In addition, only the ν_1 dye laser was pumped by the UV output of the Nd: YAG laser. The

ν_2 dye laser was pumped by the 532 nm light which was separated from the UV beam using the dichroic mirrors in front of the Nd:YAG pump laser. With green light pumping, the conversion efficiency of the dye approached 30%. In this work, FWDM signals at $4\nu_1 - \nu_2$ were generated between 78100 and 80100 cm^{-1}. The two-photon resonance, $4\nu_1$, was established for each 2-X vibrational band by recording both TOF and fluorescence excitation spectra of the CO $A^1\Pi(v'=10-12) \leftarrow X^1\Sigma^+(v''=0)$ transitions in separate experiments.

The predelay between the General valve and Q-switch varied from 500 μs to 740 μs which depended mainly on the exhibited rotational structures obtained in their corresponding spectral regions.

The Cl_2 gas was diluted in He to 1.6%, and delivered to the General valve at a stagnation pressure of 65 psia using the home-made gas handling system described earlier. Due to the corrosive nature of the Cl_2, pump oil with detergent (Canadian Tire Co., Diesel, Formula 2000) had to be used to prepare mixtures at the expense of the vacuum in the mixing cylinder.

3.4 References

1. S. G. Tilford and J. D. Simmons, *J. Phys. Chem.*, Ref. Data **1**, 147 (1972).

2. J. A. Coxon, *J. Mol. Spectrosc.*, **50**, 142 (1974).

3. M. G. Littman and H. J. Metcalf, *Appl. Opt.*, **17**, 2224 (1978).

4. The Lumonics dye laser manual.

5. V. Kaufman and C. J. Humphreys, *J. Opt. Soc. Am.* **59**, 1614 (1969).

6. G. R. Harrison, *M.I.T. tables*. Boston: Technology Press. M.I.T. 1939.

7. G. Hilber, A. Lago, and R. Wallenstein, *J. Opt. Soc. Am.*, B **4**, 1753 (1987).

8. Comstock TOF manual

Chapter 4

Results and Analyses

4.1 Results and Analysis of the $E0^+ \leftarrow X0^+$ Transition of BrCl

Vibrationally and rotationally resolved spectra of the $E0^+$ ion-pair state $\leftarrow$ $X0^+$ ground state transition of jet-cooled BrCl near 145 nm were recorded for the first time. The isotopomer identity of the LIF excitation spectra of $E0^+ \leftarrow X0^+$ transition became straightforward with the help of single isotopomer TOF spectra, although the large band intensity variations as a function of frequency were still present. Small segments of the VUV fluorescence and TOF excitation spectra near 145.4 nm are presented in Fig. 4.1. The fluorescence excitation portion is shown in trace (a). The mass selected spectra in traces (b), (c), and (d) were obtained by temporally gating for the $^{79}Br^{35}Cl$ isotopomer, the $^{79}Br^{37}Cl/^{81}Br^{35}Cl$ combination, and the $^{81}Br^{37}Cl$ species, respectively. There is little doubt that the correct isotopomer assignments are now possible using single isotopomer TOF excitation spectra. Note that although the flight times of the $^{79}Br^{37}Cl/^{81}Br^{35}Cl$ pair could not be resolved with our instrument, their bands could be distinguished by monitoring either $^{79}Br^+$ or $^{81}Br^+$ daughter ions produced by predissociation followed by ionization as a function of VUV laser frequency. In this way, the spectrum in trace 1(c) could be assigned to the $^{81}Br^{35}Cl$ isotopomer only.

4.1.1 Spectra Calibration

The VUV light source used to excite the jet-cooled BrCl molecules was generated by four-wave difference mixing (FWDM) in Kr. The fundamental laser frequencies, υ_1 and υ_2, needed to be calibrated to determine the exact frequency of the observed vibrationally and rotationally resolved bands of the $E0^+$ ion-pair state $\leftarrow$ $X0^+$ ground state transition at $\upsilon_{VUV} = 4\,\upsilon_1 - \upsilon_2$.

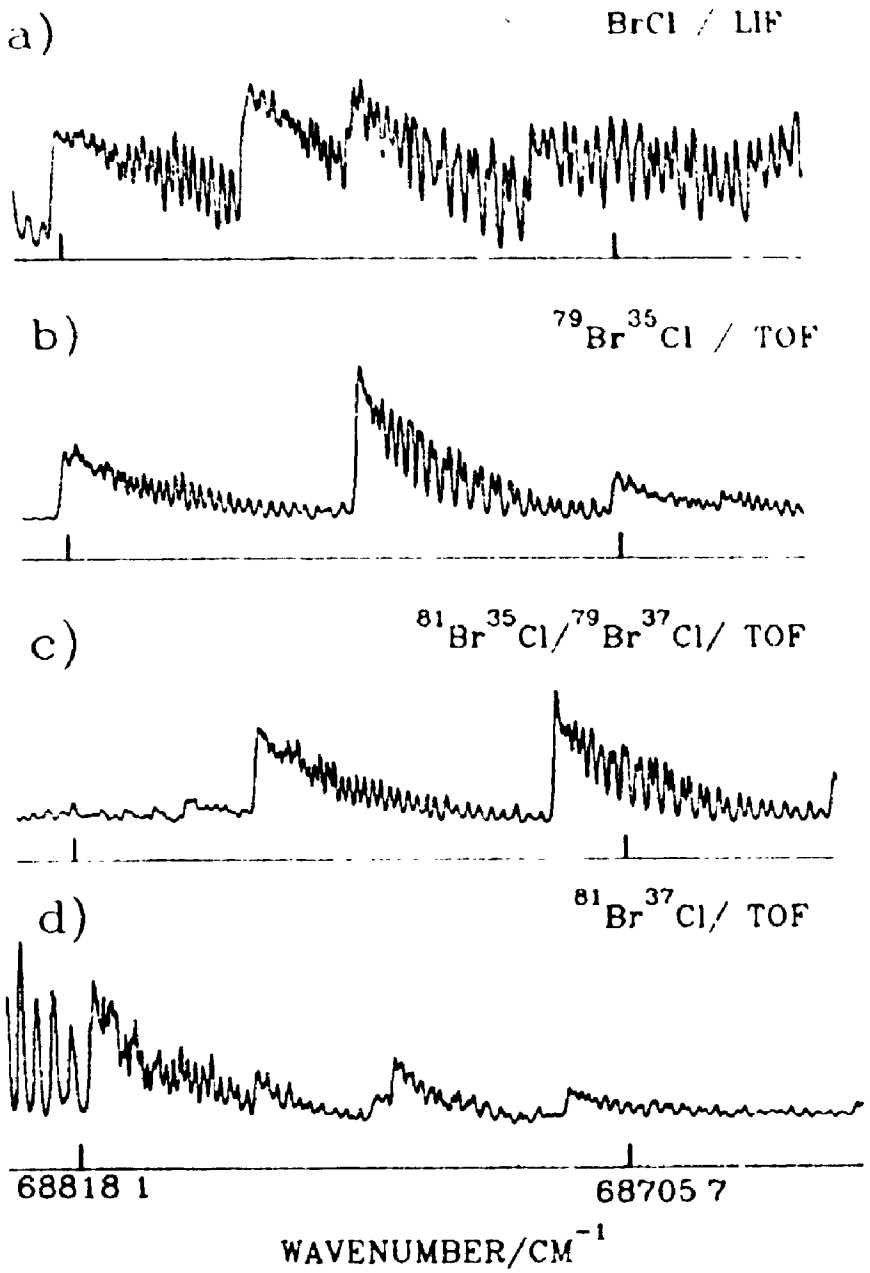

Fig. 4.1. A small portion of the VUV laser excitation spectrum of BrCl near 145.4 nm. The strongest vibrational band of the $E \leftarrow X$ transition for the $^{79}Br^{35}Cl$ isotopomer in this spectral region was assigned to (182,0). (a) VUV laser-induced fluorescence excitation spectrum of a naturally abundant isotopic sample of BrCl. (b) VUV laser/time-of-flight (TOF) mass spectrum of the $^{79}Br^{35}Cl$ isotopomer. (c) VUV laser/TOF mass spectrum of the $^{81}Br^{35}Cl/^{79}Br^{37}Cl$ isotopomer pair. (d) VUV laser/TOF mass spectrum of the $^{81}Br^{37}Cl$ isotopomer.

The frequency of the tunable υ_2 dye laser was determined by using a small portion of its output to excite the optogalvanic (OG) spectrum of neon atoms in an Fe/Ne hollow cathode lamp. OG signals could be observed when the wavelength of the υ_2 laser was in resonance with an allowed transition in the neon atoms. Since these Ne transitions are accurately known [1] they can be used to produce a frequency scale. The OG spectrum was recorded at the same time as the VUV/TOF and VUV/LIF excitation spectra. All signals were processed in separate gated integrators/boxcar averagers, digitized, and stored in a computer for later analysis.

The OG calibration spectrum displayed on a three-pen chart recorder paper was used to establish the initial assignment of the observed OG lines by trial and error. A computer program for measuring spectra was developed in this lab to assign a digitized point number for any selected OG peak of known frequency υ_2. Initially, the literature value of the two-photon resonance in Kr, $4\upsilon_1 = 92307.4393$ cm^{-1} [2], was used to determine the resultant frequency of the VUV radiation corresponding to each measured OG line. These calculated VUV frequencies in turn were fitted to a second order polynomial:

$$y = a + bx + cx^2 \qquad (4.1)$$

by the method of least-squares, where y is the wavenumber of VUV radiation corresponding to the selected OG peaks of a scan, x is the digitized point number along a scan, and {a, b, and c} are constants determined from the fit. In the linear least-squares analysis, the objective is to obtain the best fit by minimizing the sum of squares deviations of the observed transition wavenumbers to those calculated using Eq. 4.1. Once done the frequency of any unknown line in either the VUV/TOF or VUV/LIF excitation spectra could be obtained by substituting its point number (from the frequency scale) into the "best" Eq. 4.1 determined by the OG lines. In general, the standard deviation of a fit was ≤ 0.1 cm^{-1}. A larger standard deviation was usually an indication that one or more OG lines were misassigned.

Typically, the two-photon resonance frequency was expected to differ slightly from that in the literature because its experimental value was that required to optimize the VUV generation, not the two-photon absorption. For this reason, the frequency of fixed

υ_1 dye laser had to be calibrated as well. This was accomplished by recording both TOF and fluorescence excitation spectra of closest member (frequency-wise) of the well-known CO $A^1\Pi(v') \leftarrow X^1\Sigma^+(v''=0)$ progression [3] in separate experiments. For the BrCl experiments, v' = 3. By using the same peak measurement and fitting programs described above, it was found that our transition wavenumbers were systematically higher by ≈ 0.21 cm^{-1} from published data when the literature value of the two-photon resonance of Kr was used. A correction of 0.21 cm^{-1} was therefore subtracted from each frequency measurement. Taking into account the laser linewidth, the standard deviation of the fit, and the discrepancy of the two-photon resonance used, the absolute accuracy of our measurements is estimated to be ≈ 0.5 cm^{-1}.

4.1.2 Rotational Analysis

As noted earlier, our instrument could not resolve the time-of-flight of the $^{79}Br^{37}Cl$ isotopomer from that of $^{81}Br^{35}Cl$ directly due to their nearly identical masses. Therefore, the production of either $^{79}Br^+$ or $^{81}Br^+$ daughter ions was monitored so that their relative contributions could be deconvoluted. In this way, it was determined that all the observed spectra of these two isotopomers were actually due to $^{81}Br^{35}Cl$ exclusively. Therefore, the VUV/TOF spectra of only three of the four possible isotopomers, $^{79}Br^{35}Cl$, $^{81}Br^{35}Cl$, and $^{81}Br^{37}Cl$, were analyzed.

The rotational branch structure for the $E0^+$ ion pair state $\leftarrow$ $X0^+$ ground state transition is governed by the single-photon rotational selection rule, $\Delta J = \pm 1$, which leads to one *R* and one *P* branch only. All vibrational bands observed were strongly red-shaded which indicates that band head formation occurs in the *R* branch. The rotational assignment for each band, branch assignments and *J* numbering, was established by trial and error using ground state (v'' = 0) combination differences, $\Delta_2F''(J)$. These could be calculated for each isotopomer by substituting the ground state parameters reported by Coxon (Ref. 4, see Tables I and II) into the well-known formula [5]:

$$\Delta_2F''(J) \approx 4\,B_0''(J+1/2) - 8\,D_0''(J+1/2)^3. \qquad (4.2)$$

Since B_0'' and D_0'' were only available for $^{79}Br^{35}Cl$ and $^{81}Br^{35}Cl$ from Coxon's work [4], the corresponding parameters for $^{81}Br^{37}Cl$ used to calculate the ground state combination differences by Eq. 4.2 was obtained by mass-scaling, relative to $^{79}Br^{35}Cl$ (Table III).

Next, for each band, combination differences were calculated using two transitions, one from the *R* branch and the other from the *P* branch, which were picked out randomly. These $\Delta_2F''(J)$ values were compared with those derived from Coxon's ground state parameters to determine the absolute *J* numbering of the bands. In the beginning of each band analysis, the correct J numbering and branch assignments were uncertain. The calculation were repeated therefore with different branch and/or J assignments until the $\Delta_2F''(J)$ values obtained in this way agreed with these calculated using Eq. 4.2. Despite the limited number of transitions per band due to the jet-cooling, both set of combination difference had to agree with each other within experimental error to be acceptable. Once completed, the transition wavenumbers obtained for each band were averaged from a range of 2 to 8 spectra. These averaged transition wavenumbers for the *P* and *R* branches were then fitted simultaneously by the method of least-squares using a Dunham analysis computer program developed in this lab.

The general Dunham expansion discussed in Chapter 2 was modified for analysis of rovibronic spectra because in this case, two Dunham expansions are required, one for excited state, and the other for the ground state. The appropriate expression for the Dunham expansion can be written as:

$$\upsilon_i = \upsilon_0 + \sum_n Y'_{0,n}\left[J'(J'+1)\right]^n - \sum_m Y''_{0,m}\left[J''(J''+1)\right]^m \qquad (4.3)$$

where υ_i is averaged measured transition wavenumbers obtained from the least-squares calibration program, υ_0 is the band origin of the particular rovibronic transition, $\{ Y'_{0,n} \}$ is the set of the excited state (*E*-state in this case) rotational constants for a particular vibrational level, and $\{ Y''_{0,m} \}$ is the set of ground state Dunham parameters. For each computer analysis, the transition wavenumbers of the assigned *P* and *R* lines were inputted following the format required by the program. Occasionally, for so. bands, a few odd-looking lines were evident whose transition wavenumber deviated from the

Table I. Rotational constants (in cm^{-1}) for the $X0^+$ ground state of $^{79}Br^{35}Cl$ from Ref. 4.

Parameter	Value
B_e	0.152469
α_e	7.697×10^{-4}
γ_e	-2.56×10^{-6}
D_0	7.200×10^{-8}

Table II. Rotational constants (in cm^{-1}) for the $X0^+$ ground state of $^{81}Br^{35}Cl$ from Ref. 4.

Parameter	Value
B_e	0.150926
α_e	7.640×10^{-4}
γ_e	-1.87×10^{-6}
D_0	7.092×10^{-8}

Table III. Calculated rotational constants (in cm^{-1}) for the $X0^+$ ground state of $^{81}Br^{37}Cl$.

Parameter	Value
B_e	0.145602
α_e	7.183×10^{-4}
D_0	6.566×10^{-8}

calculated value obtained from the least-squares analysis by more than 3σ, where σ is the standard deviation of the fit. These peaks were weighted to zero in the fit on the basis that such deviations were uncharacteristic of the distribution of the measurement errors for the other lines. For the majority of the bands, however, almost every rotational line was acceptable. Ultimately, the *E*-state rotational constants for different vibrational levels were generated from the fitting program with final σ values in the range $0.05\ cm^{-1} \leq \sigma \leq 0.32\ cm^{-1}$. In the case of the $^{81}Br^{37}Cl$ isotopomer whose ground state rotational *B* value was unknown, B_0'' ($\approx Y''_{01}$) was floated, and found to be (on average value) $0.146\ cm^{-1}$.

Another useful feature of the program was its capability of predicting unknown rotational lines once a number of lines was assigned. This helped to identify vague or unresolved features.

Branch assignments were also switched for each band; that is, lines assigned to the *R* branch were assigned to the *P* branch, and vice versa. The analysis procedure above was then repeated to establish another set of possible *J* numbers. On occasion, an alternate *J* numbering could be attained for a band with reasonable combination differences. In these cases, both sets of assignments were fitted by the Dunham program. The branch assignment chosen was that which predicted the position of the band head best. A close-up of a vibronic band for each isotopomer is shown in Figs. 4.2-4.

The branch assignments and *J* numbering of all analyzed vibrational bands of the $E0^+ \leftarrow X0^+$ transition are presented in Tables IV to XXXIII. The results of rotational analyses for three BrCl isotopomers can be found in Tables XXXIV -XXXVI.

It can be gleamed from Tables XXXIV - XXXVI, that the variation of the B'_vs with v' is irregular. In addition, for some of the bands, the D'_v ($\approx -Y'_{02}$) constants are either not determined statistically or had the wrong sign. These results are attributed to interstate perturbations.

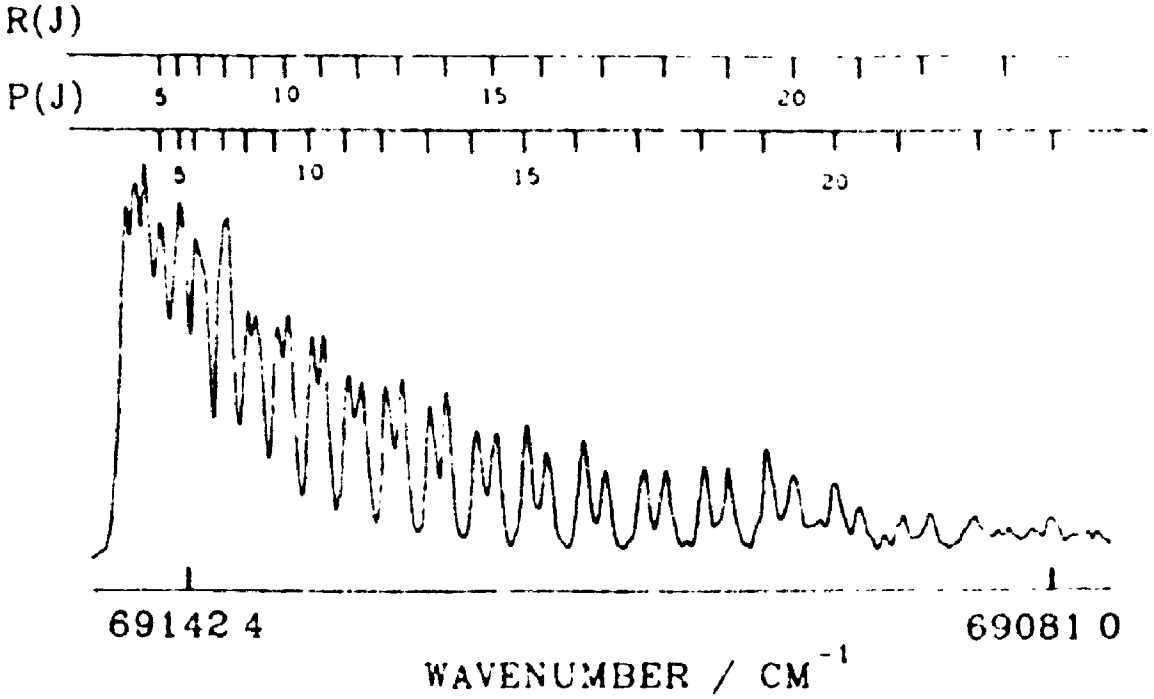

Fig. 4.2. A close-up of the vibrational band assigned to the (189,0) member of the $E0^+ \leftarrow X0^+$ band system of $^{79}Br^{35}Cl$. Branch assignments and rotational quantum numbers are indicated

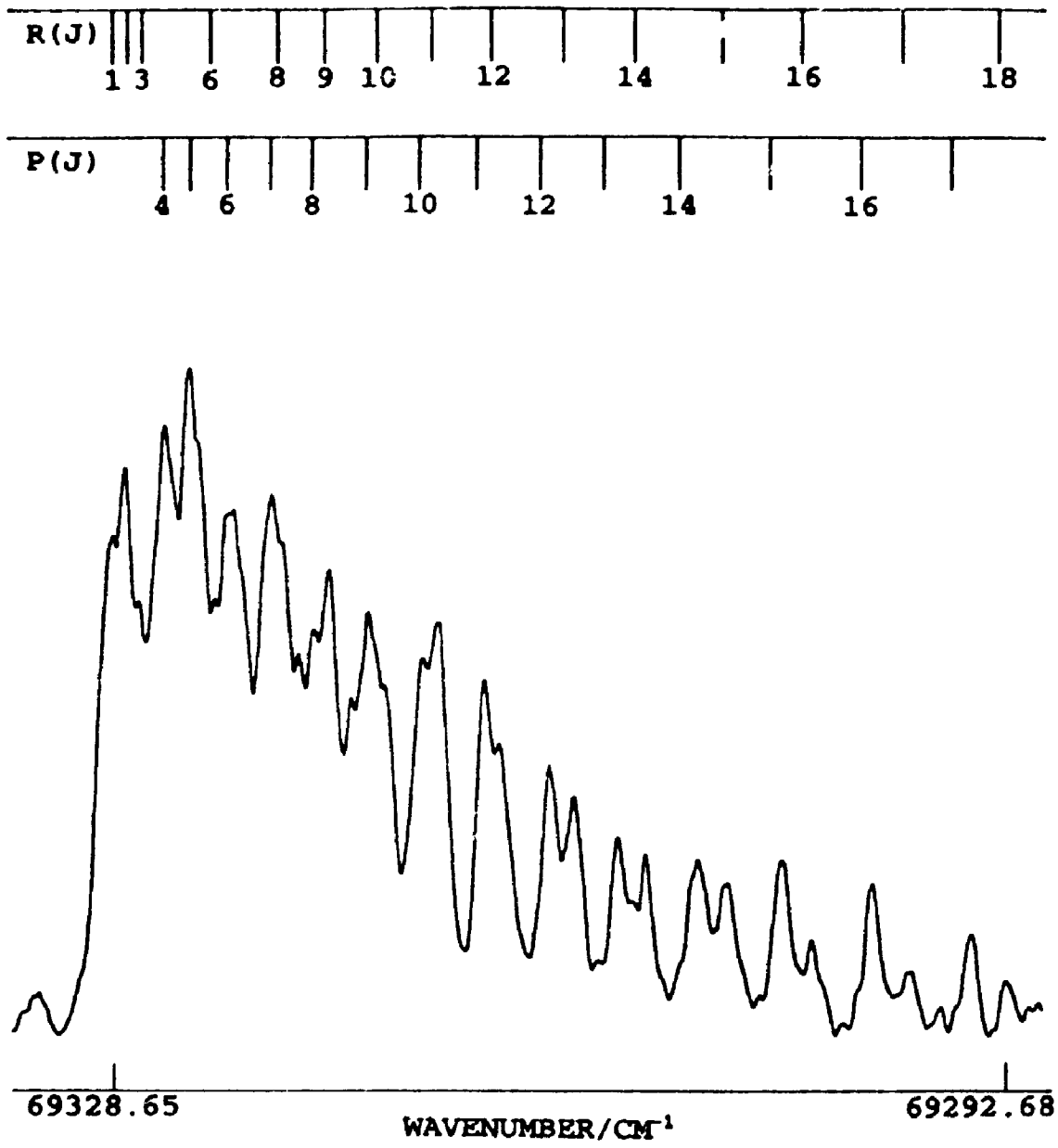

Fig. 4.3 A close-up of the vibrational band assigned to the (193,0) member of the $E0^+ \leftarrow X0^+$ band system of $^{81}Br^{35}Cl$. Branch assignments and rotational quantum numbers are indicated.

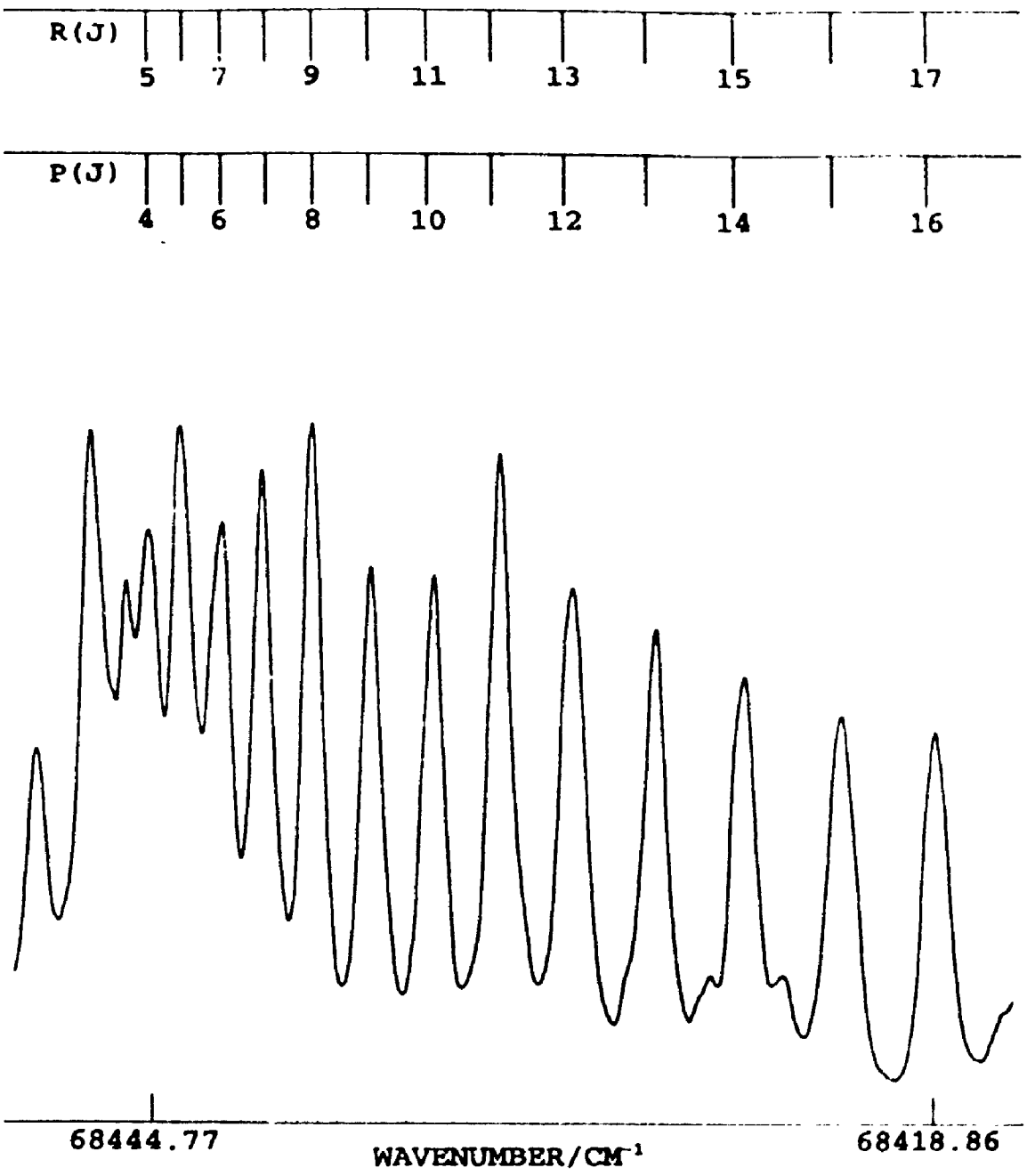

Fig. 4.4 A close-up of the vibrational band assigned to the (181,0) member of the $E0^+ \leftarrow X0^+$ band system of $^{81}Br^{37}Cl$. Branch assignments and rotational quantum numbers are indicated

Table IV. Transition wavenumbers (cm^{-1}), branch assignments, and ground state combinations, $\Delta_2F''(J)$ (in cm^{-1}), for the (173, 0) band of $^{79}Br^{35}Cl$.

J	$R(J)$	$P(J)$	$\Delta_2F''(J)^{obs}$	[a] $\Delta_2F''(J)^{calc.}$	[b] $\Delta(\Delta_2F''(J))^{o-c}$
10		68221.42(9-)[c]		6.39	
11	68220.65(15)[c]	68218.87(0)		7.00	
12	68217.70(-7)	68215.98(3)	7.88	7.60	+0.28
13	68214.79(-2)	68212.77(12)	8.08	8.21	-0.13
14	68211.62(1)	68209.62(7)	8.87	8.82	+0.05
15	68208.22(4)	68205.92(-7)	9.78	9.43	+0.35
16	68204.48(-4)	68201.84(-34)	10.03	10.04	-0.01
17	68200.58(-4)	68198.19(4)	10.67	10.64	+0.03
18	68196.42(-7)	68193.80(-7)	11.16	11.25	-0.09
19	68192.15(2)	68189.42(5)		11.86	
20	68187.64(10)			12.47	

[a] Calculated using Eq. 4.2.
[b] $\Delta_2F''(J)^{obs.} - \Delta_2F''(J)^{calc.}$ in cm^{-1} units.
[c] Observed-calculated residuals in units of 10^{-2} cm^{-1}.

Table V. Transition wavenumbers (cm^{-1}), branch assignments, and ground state combinations, $\Delta_2F''(J)$ (in cm^{-1}), for the (174, 0) band of $^{79}Br^{35}Cl$.

J	$R(J)$	$P(J)$	$\Delta_2F''(J)^{obs.}$	[a] $\Delta_2F''(J)^{calc}$	[b] $\Delta(\Delta_2F''(J))^{o-c}$
10	68283.68(4)[c]			6.39	
11	68281.11(1)		7.03	7.00	+0.03
12	68278.34(2)	68276.64(0)[c]	7.61	7.60	+0.01
13	68275.25(-5)	68273.50(0)	8.31	8.21	+0.10
14	68272.00(-4)	68270.04(-7)	8.83	8.82	+0.01
15	68268.48(-7)	68266.42(-6)	9.48	9.43	+0.05
16	68264.74(-8)	68262.52(-9)	10.05	10.04	+0.01
17	68260.81(-5)	68258.43(-9)	10.45	10.64	-0.19
18	68256.48(-18)	68254.29(11)	11.12	11.25	-0.13
19	68252.25(4)	68249.69(8)	11.64	11.86	-0.22
20	68247.58(4)	68244.83(4)		12.47	
21	68242.61(-1)			13.07	
22	68237.55(8)			13.68	

[a] Calculated using Eq. 4.2.

[b] $\Delta_2F''(J)^{obs} - \Delta_2F''(J)^{calc.}$ in cm^{-1} units

[c] Observed-calculated residuals in units of 10^{-2} cm^{-1}.

Table VI. Transition wavenumbers (cm^{-1}), branch assignments, and ground state combinations, $\Delta_2F''(J)$ (in cm^{-1}), for the (175,0) band of $^{79}Br^{35}Cl$.

J	$R(J)$	$P(J)$	$\Delta_2F''(J)^{obs.}$	[a] $\Delta_2F''(J)^{calc.}$	[b] $\Delta(\Delta_2F''(J))^{o-c}$
9		68345.52(-9)[c]		5.78	
10	68344.93(3)[c]	68343.11(-16)		6.39	
11	68342.43(-6)	68340.74(3)	7.03	7.00	+0.03
12	68339.77(-8)	68337.90(-1)	7.51	7.60	-0.09
13	68336.95(-4)	68334.92(3)	8.06	8.21	-0.15
14	68333.83(-7)	68331.71(7)	8.77	8.82	-0.05
15	68330.50(-8)	68328.18(1)	9.41	9.43	-0.02
16	68326.85(-19)	68324.42(-5)	9.98	10.04	-0.06
17	68323.21(-6)	68320.52(-2)	10.38	10.64	-0.26
18	68319.30(2)	68316.47(7)	11.19	11.25	-0.06
19	68315.06(1)	68312.02(0)	11.88	11.86	+0.02
20	68310.65(4)	68307.42(0)	12.53	12.47	+0.06
21	68305.92(-1)	68302.53(-6)	13.11	13.07	+0.04
22	68301.22(18)	68297.54(1)		13.68	

[a] Calculated using Eq. 4.2.
[b] $\Delta_2F''(J)^{obs} - \Delta_2F''(J)^{calc.}$ in cm^{-1} units
[c] Observed-calculated residuals in units of 10^{-2} cm^{-1}.

Table VII. Transition wavenumbers (cm^{-1}), branch assignments, and ground state combinations, $\Delta_2F''(J)$ (in cm^{-1}), for the (182, 0)band of $^{79}Br^{35}Cl$.

J	$R(J)$	$P(J)$	$\Delta_2F''(J)^{obs.}$	[a] $\Delta_2F''(J)^{calc.}$	[b] $\Delta(\Delta_2F''(J))^{o-c}$
6		68753.64(8)[c]		3.95	
7		68752.03(10)		4.56	
8		68750.16(-1)		5.17	
9		68748.30(-5)		5.78	
10	68747.89(13)[c]	68745.94(-10)		6.39	
11	68745.37(-1)	68743.45(-7)	7.03	7.00	+0.03
12	68742.88(12)	68740.86(10)	7.59	7.60	-0.01
13	68740.03(13)	68737.78(0)	8.31	8.21	+0.10
14	68736.71(-9)	68734.57(2)	8.85	8.82	+0.03
15	68733.28(-18)	68731.18(10)	9.27	9.43	-0.16
16	68729.93(6)	68727.45(7)	9.84	10.04	-0.20
17	68726.01(-2)	68723.44(1)	10.66	10.64	+0.02
18	68721.80(-13)	68719.27(4)	11.14	11.25	-0.11
19	68717.41(-16)	68714.87(8)	11.78	11.86	-0.08
20	68712.86(-10)	68710.02(-5)		12.47	
21	68708.29(23)			13.07	

[a] Calculated using Eq. 4.2.

[b] $\Delta_2F''(J)^{obs.} - \Delta_2F''(J)^{calc.}$ in cm^{-1} units

[c] Observed-calculated residuals in units of 10^{-2} cm^{-1}.

Table VIII. Transition wavenumbers (cm^{-1}), branch assignments, and ground state combinations, $\Delta_2F''(J)$ (in cm^{-1}), for the (183, 0) band of $^{79}Br^{35}Cl$.

J	$R(J)$	$P(J)$	$\Delta_2F''(J)^{obs.}$	[a] $\Delta_2F''(J)^{calc.}$	[b] $\Delta(\Delta_2F''(J))^{o-c}$
8	68810.84(-4)[c]	68809.91(6)[c]		5.17	
9	68808.66(-11)	68807.62(2)	5.82	5.78	+0.04
10	68806.34(-7)	68805.02(-9)	6.37	6.39	-0.02
11	68803.89(8)	68802.29(-9)	6.92	7.00	-0.08
12	68800.89(-8)	68799.42(1)	7.71	7.60	+0.11
13	68797.94(4)	68796.18(-3)	8.24	8.21	+0.03
14	68794.58(-1)	68792.65(-11)	8.63	8.82	-0.19
15	68791.06(2)	68789.31(23)	9.51	9.43	+0.08
16	68787.40(14)	68785.07(-9)	10.15	10.04	+0.11
17	68783.19(-6)	68780.91(-9)	10.68	10.64	+0.04
18	68779.07(6)	68776.72(10)	11.14	11.25	-0.11
19	68774.43(-11)	68772.05(4)	11.85	11.86	-0.01
20	68769.72(-12)	68767.22(7)	12.22	12.47	-0.25
21	68764.89(-3)	68762.21(13)		13.07	

[a] Calculated using Eq. 4.2.

[b] $\Delta_2F''(J)^{obs.} - \Delta_2F''(J)^{calc.}$ in cm^{-1} units

[c] Observed-calculated residuals in units of 10^{-2} cm^{-1}.

Table IX. Transition wavenumbers (cm^{-1}), branch assignments, and ground state combinations, $\Delta_2F''(J)$ (in cm^{-1}), for the (189, 0) band of $^{79}Br^{35}Cl$.

J	$R(J)$	$P(J)$	$\Delta_2F''(J)^{obs.}$	[a] $\Delta_2F''(J)^{calc.}$	[b] $\Delta(\Delta_2F''(J))^{o-c}$
7		69139.44(16)[c]		4.56	
8	69138.94(5)[c]	69137.45(-22)		5.17	
9	69136.95(8)	69135.47(-4)	5.85	5.78	+0.07
10	69134.70(8)	69133.08(-3)	6.46	6.39	+0.07
11	69132.26(12)	69130.50(1)	6.98	7.00	-0.02
12	69129.52(9)	69127.73(10)	7.68	7.60	+0.08
13	69126.55(7)	69124.58(4)	8.24	8.21	+0.03
14	69123.39(9)	69121.28(6)	8.83	8.82	-0.01
15	69119.88(-2)	69117.72(6)	9.52	9.43	+0.09
16	69116.31(6)	69113.88(0)	10.10	10.04	+0.06
17	69112.41(3)	69109.78(-8)	10.69	10.64	+0.05
18	69108.19(-8)	69105.62(1)	11.26	11.25	+0.01
19	69103.86(-8)	69101.15(2)	11.85	11.86	-0.01
20	69099.53(17)	69096.34(-8)	12.46	12.47	-0.01
21	69094.56(0)	69091.40(-7)	13.19	13.07	+0.12
22	69089.36(-17)	69086.34(5)	13.27	13.68	-0.41
23	69083.85(-41)	69081.30(41)		14.29	

[a] Calculated using Eq. 4.2.

[b] $\Delta_2F''(J)^{obs.} - \Delta_2F''(J)^{calc.}$ in cm^{-1} units

[c] Observed-calculated residuals in units of 10^{-2} cm^{-1}.

Table X. Transition wavenumbers (cm^{-1}), branch assignments, and ground state combinations, $\Delta_2F''(J)$ (in cm^{-1}), for the (192, 0) band of $^{79}Br^{35}Cl$.

J	$R(J)$	$P(J)$	$\Delta_2F''(J)^{obs.}$	[a]$\Delta_2F''(J)^{calc.}$	[a]$\Delta(\Delta_2F''(J))^{o-c}$
11		69285.22(-8)[c]		7.00	
12	69284.64(18)[c]	69282.44(-6)		7.60	
13	69281.93(34)	69279.52(3)	8.38	8.21	+0.17
14	69278.60(10)	69276.27(2)	9.19	8.82	+0.37
15	69275.29(11)	69272.75(-3)	9.55	9.43	+0.12
16	69271.72(10)	69269.04(-3)	10.16	10.04	+0.12
17	69267.90(5)	69265.14(-1)	10.68	10.64	+0.04
18	69263.86(2)	69261.04(6)	11.24	11.25	-0.01
19	69259.65(6)	69256.65(6)	11.93	11.86	+0.07
20	69254.16(-95)	69251.92(-5)	12.59	12.47	+0.12
21	69250.27(-13)	69247.06(-6)	13.21	13.07	+0.14
22	69245.41(-4)	69241.95(-8)	13.61	13.68	-0.07
23	69240.19(-8)	69236.66(-6)	14.28	14.29	-0.01
24	69234.78(-7)	69231.14(-3)	14.91	14.90	+0.01
25	69229.12(-9)	69225.28(-10)	15.17	15.50	-0.33
26	69223.42(10)	69219.62(26)	16.46	16.10	+0.36
27	69217.28(9)	69212.66(-43)	16.71	16.71	0
28	69210.67(-15)	69206.70(10)	17.38	17.32	+0.06
29	69204.26(4)	69199.91(4)	17.60	17.93	-0.33
30	69197.34(-4)	69193.07(18)		18.54	
31	69190.33(4)			19.14	

[a]Calculated using Eq. 4.2.
[b]$\Delta_2F''(J)^{obs}$ - $\Delta_2F''(J)^{calc.}$ in cm^{-1} units
[c]Observed-calculated residuals in units of 10^{-2} cm^{-1}.

Table XI. Transition wavenumbers (cm^{-1}), branch assignments, and ground state combinations, $\Delta_2F''(J)$ (in cm^{-1}), for the (196, 0) band of $^{79}Br^{35}Cl$.

J	$R(J)$	$P(J)$	$\Delta_2F''(J)^{obs}$	[a] $\Delta_2F''(J)^{calc}$	[b] $\Delta(\Delta_2F''(J))^{o-c}$
7		69508.27(-7)[c]		4.56	
8	69507.95(24)[c]	69506.43(-1)		5.17	
9	69505.88(16)	69504.29(0)	6.01	5.78	+0.23
10	69503.58(9)	69501.93(1)	6.58	6.39	+0.19
11	69501.17(13)	69499.30(-3)	7.16	7.00	+0.16
12	69498.41(4)	69496.42(-8)	7.73	7.60	+0.13
13	69495.56(10)	69493.44(0)	8.22	8.21	+0.01
14	69492.39(7)	69490.19(4)	8.95	8.82	+0.13
15	69488.90(-6)	69486.62(-2)	9.45	9.43	+0.02
16	69485.35(-1)	69482.94(5)	10.16	10.04	+0.12
17	69481.48(-5)	69478.73(-19)	10.57	10.64	-0.07
18	69477.48(0)	69474.78(6)	11.30	11.25	+0.05
19	69473.19(-1)	69470.18(10)	11.84	11.86	-0.02
20	69468.74(5)	69465.64(2)	12.56	12.47	+0.09
21	69463.75(-20)	69460.64(-10)		13.07	
22	69459.21(23)			14.29	

[a] Calculated using Eq. 4.2.

[b] $\Delta_2F''(J)^{obs.} - \Delta_2F''(J)^{calc.}$ in cm^{-1} units.

[c] Observed-calculated residuals in units of 10^{-2} cm^{-1}.

Table XII. Transition wavenumbers (cm^{-1}), branch assignments, and ground state combinations, $\Delta_2F''(J)$ (in cm^{-1}), for the (197, 0) band of $^{79}Br^{35}Cl$.

J	$R(J)$	$P(J)$	$\Delta_2F''(J)^{obs}$	[a] $\Delta_2F''(J)^{calc}$	[b] $\Delta(\Delta_2F''(J))^{o-c}$
9		69561.16(5)[c]		5.78	
10	69560.79(10)[c]	69558.63(-23)		6.39	
11	69558.07(-29)	69556.51(11)	7.70	7.00	+0.70
12	69555.70(-11)	69553.72(3)	6.99	7.60	-0.61
13	69552.90(-12)	69551.08(32)	8.03	8.21	-0.18
14	69549.91(-6)	69547.67(8)	8.79	8.82	-0.03
15	69546.82(12)	69544.11(-8)	9.50	9.43	+0.07
16	69543.54(38)	69540.42(-14)	10.24	10.04	+0.20
17	69539.27(-11)	69536.58(-9)	10.99	10.64	+0.34
18	69535.29(-6)	69532.56(3)	10.91	11.25	-0.34
19	69530.61(-43)	69528.36(23)	11.99	11.86	+0.13
20		69523.29(-19)		12.47	

[a] Calculated using Eq. 4.2.

[b] $\Delta_2F''(J)^{obs.} - \Delta_2F''(J)^{calc.}$ in cm^{-1} units

[c] Observed-calculated residuals in units of 10^{-2} cm^{-1}.

Table XIII. Transition wavenumbers (cm^{-1}), branch assignments, and ground state combinations, $\Delta_2F''(J)$ (in cm^{-1}), for the (198, 0) band of $^{79}Br^{35}Cl$.

J	$R(J)$	$P(J)$	$\Delta_2F''(J)^{obs.}$	[a] $\Delta_2F''(J)^{calc.}$	[b] $\Delta(\Delta_2F''(J))^{o-c}$
6		69607.55(6)[c]		3.95	
7	69607.55(6)[c]	69606.04(12)		4.56	
8	69606.04(12)	69604.17(3)	5.38	5.17	+0.21
9	69604.17(3)	69602.16(1)	6.16	5.78	+0.38
10	69602.16(1)	69599.88(-8)	6.92	6.39	+0.54
11	69599.88(-8)	69597.25(-30)	7.35	7.00	+0.35
12	69597.25(-30)	69594.81(-12)	8.04	7.60	+0.43
13	69594.81(-12)	69591.84(-27)	8.20	8.21	-0.01
14	69591.84(-27)	69589.05(-3)	8.95	8.82	+0.13
15	69589.05(-3)	69585.86(3)	9.28	9.42	-0.14
16	69585.86(3)	69582.56(18)	10.24	10.04	+0.20
17	69582.56(18)	69578.82(9)	10.94	10.64	+0.30
18	69578.82(9)	69574.92(7)		11.25	
19	69574.92(7)			11.86	

[a] Calculated using Eq. 4.2.

[b] $\Delta_2F''(J)^{obs.} - \Delta_2F''(J)^{calc.}$ in cm^{-1} units.

[c] Observed-calculated residuals in units of 10^{-2} cm^{-1}.

Table XIV. Transition wavenumbers (cm^{-1}), branch assignments, and ground state combinations, $\Delta_2F''(J)$ (in cm^{-1}), for the (175, 0) band of $^{81}Br^{35}Cl$.

J	$R(J)$	$P(J)$	$\Delta_2F''(J)^{obs.}$	[a] $\Delta_2F''(J)^{calc}$	[b] $\Delta(\Delta_2F''(J))^{o-c}$
6		68313.19(22)[c]		3.92	
7	68312.99(5)[c]	68311.79(3)		4.53	
8	68311.52(30)	68310.02(12)	5.31	5.13	+0.18
9	68309.51(23)	69307.68(-13)	6.22	5.74	+0.48
10	68307.29(16)	68305.30(-19)	6.41	6.34	+0.07
11	68304.72(-2)	68303.10(15)	7.08	6.94	+0.14
12	68302.13(0)	68300.21(3)	7.53	7.54	-0.01
13	68299.16(-14)	68297.19(0)	8.11	8.15	-0.04
14	68296.09(-15)	68294.02(4)	8.71	8.75	-0.04
15	68292.95(-1)	68290.45(-10)	9.34	9.36	-0.02
16	68289.49(3)	68286.74(-14)	10.02	9.96	+0.06
17	68285.61(-12)	68282.93(-7)	10.65	10.56	+0.09
18	68281.86(9)	68278.84(-6)	11.00	11.16	-0.16
19	68277.56(-4)	68274.61(5)	11.92	11.77	+0.15
20	68273.28(8)	68269.94(-7)	12.53	12.37	+0.16
21	68268.76(18)	68265.03(-20)		12.97	
22	68263.85(12)			13.58	

[a] Calculated using Eq. 4 2.

[b] $\Delta_2F''(J)^{obs}$ - $\Delta_2F''(J)^{calc.}$ in cm^{-1} units

[c] Observed-calculated residuals in units of 10^{-2} cm^{-1}.

Table XV. Transition wavenumbers (cm^{-1}), branch assignments, and ground state combinations, $\Delta_2F''(J)$ (in cm^{-1}), for the (182, 0) band of $^{81}Br^{35}Cl$.

J	$R(J)$	$P(J)$	$\Delta_2F''(J)^{obs.}$	[a] $\Delta_2F''(J)^{calc.}$	[b] $\Delta(\Delta_2F''(J))^{o-c}$
7	68713.44(6)[c]	68712.84(23)[c]		4.53	
8	68711.42(-1)	68710.72(16)	5.09	5.13	-0.04
9	68708.96(-28)	68708.35(10)	5.62	5.74	-0.12
10	68706.59(-19)	68705.80(10)	6.06	6.34	-0.28
11	68703.94(-13)	68702.89(0)	6.76	6.94	-0.18
12	68701.01(-12)	68699.83(-1)	7.47	7.54	-0.07
13	68697.78(-14)	68696.48(-5)	8.02	8.15	-0.13
14	68694.36(-10)	68692.99(1)	8.60	8.75	-0.15
15	68690.67(-9)	68689.18(1)	9.18	9.36	-0.18
16	68686.88(7)	68685.19(7)	9.83	9.96	-0.13
17	68682.74(13)	68680.84(4)	10.61	10.56	+0.05
18	68678.18(3)	68676.27(2)	11.24	11.16	+0.08
19	68673.52(8)	68671.50(6)	11.81	11.77	+0.04
20	68668.46(-4)	68666.37(-1)		13.58	

[a] Calculated using Eq. 4.2.
[b] $\Delta_2F''(J)^{obs.} - \Delta_2F''(J)^{calc}$ in cm^{-1} units.
[c] Observed-calculated residuals in units of 10^{-2} cm^{-1}.

Table XVI. Transition wavenumbers (cm^{-1}), branch assignments, and ground state combinations, $\Delta_2F''(J)$ (in cm^{-1}), for the (183, 0) band of $^{81}Br^{35}Cl$.

J	$R(J)$	$P(J)$	$\Delta_2F''(J)^{obs.}$	[a]$\Delta_2F''(J)^{calc.}$	[b]$\Delta(\Delta_2F''(J))^{o-c}$
5	68776.97(3)[c]	68776.42(4)[c]		3.32	
6	68775.55(5)	68774.95(13)	3.84	3.92	-0.08
7	68773.78(-2)	68773.13(11)	4.60	4.53	-0.07
8	68771.84(-1)	68770.95(-2)	5.17	5.13	+0.04
9	68769.74(6)	68768.61(-6)	5.81	5.74	+0.07
10	68767.24(-1)	68766.03(-9)	6.51	6.34	+0.17
11	68764.60(2)	68763.22(-11)	7.09	6.94	+0.15
12	68761.54(-13)	68760.15(-16)	7.65	7.54	+0.11
13	68758.49(-4)	68756.95(-9)	8.01	8.15	-0.14
14	68755.17(2)	68753.53(0)	8.77	8.75	+0.02
15	68751.56(1)	68749.73(-5)	9.32	9.36	-0.04
16	68747.76(4)	68745.85(5)	9.85	9.96	-0.11
17	68743.65(-1)	68741.70(11)	10.57	10.56	+0.01
18	68739.35(-2)	68737.19(4)	10.98	11.16	-0.18
19	68734.83(-3)	68732.66(18)	11.62	11.77	-0.15
20	68730.04(-10)	68727.74(14)		12.37	
21	68725.16(-6)			12.97	

[a]Calculated using Eq. 4.2.
[b]$\Delta_2F''(J)^{obs}$ - $\Delta_2F''(J)^{calc.}$ in cm^{-1} units
[c]Observed-calculated residuals in units of 10^{-2} cm^{-1}.

Table XVII. Transition wavenumbers (cm^{-1}), branch assignments, and ground state combinations, $\Delta_2F''(J)$ (in cm^{-1}), for the (189, 0) band of $^{81}Br^{35}Cl$.

J	$R(J)$	$P(J)$	$\Delta_2F''(J)^{obs.}$	[a] $\Delta_2F''(J)^{calc}$	[b] $\Delta(\Delta_2F''(J))^{o-c}$
4	69104.69(16)[c]	69104.37(9)[c]		2.72	
5	69103.38(18)	69102.90(2)	3.66	3.32	+0.34
6	69101.75(15)	69101.02(-19)	4.21	3.92	+0.29
7	69099.76(2)	69099.16(-11)	4.69	4.53	+0.16
8	69097.66(4)	69097.06(-2)	5.57	5.13	+0.44
9	69095.40(15)	69094.19(-42)	5.78	5.74	+0.04
10	69092.46(-18)	69091.88(-1)	6.56	6.34	+0.22
11	69089.89(10)	69088.84(-8)	6.76	6.94	-0.18
12	69086.81(10)	69085.70(0)	7.66	7.54	+0.12
13	69083.56(16)	69082.24(-1)	8.33	8.15	+0.18
14	69080.05(18)	69078.48(-9)	8.94	8.75	+0.19
15	69075.96(-18)	69074.62(-3)	9.51	9.36	+0.15
16	69072.18(-2)	69070.54(2)		9.96	

[a] Calculated using Eq. 4.2.
[b] $\Delta_2F''(J)^{obs.} - \Delta_2F''(J)^{calc}$ in cm^{-1} units.
[c] Observed-calculated residuals in units of 10^{-2} cm^{-1}.

Table XVIII. Transition wavenumbers (cm^{-1}), branch assignments, and ground state combinations, $\Delta_2F''(J)$ (in cm^{-1}), for the (192, 0) band of $^{81}Br^{35}Cl$.

J	$R(J)$	$P(J)$	$\Delta_2F''(J)^{obs.}$	[a] $\Delta_2F''(J)^{calc.}$	[b] $\Delta(\Delta_2F''(J))^{o-c}$
4		69258.29(85)[c]		2.72	
5	69256.79(48)[c]	69256.54(51)	3.86	3.32	+0.54
6	69254.85(18)	69254.85(51)	4.44	3.92	+0.52
7	69253.08(32)	69252.35(-3)	4.93	4.53	+0.40
8	69250.56(-4)	69249.92(-22)	5.74	5.13	+0.61
9	69247.90(-27)	69247.35(-29)	6.13	5.74	+0.39
10	69245.25(-23)	69244.42(-44)	6.41	6.34	+0.07
11	69242.23(-29)	69241.48(-34)	7.13	6.94	+0.19
12	69238 99(-32)	69238.12(-41)	7.69	7.54	+0.15
13	69235.70(-16)	69234.54(-43)	8.24	8.15	+0.09
14	69232.04(-12)	69230.75(-42)	8.85	8.75	+0.10
15	69228.16(-5)	69226.85(-25)	9.41	9.36	+0.05
16	69224.03(1)	69222.62(-17)	10.03	9.96	+0.07
17	69219.65(4)	69218.13(-12)	10.60	10.56	+0.04
18	69215.00(3)	69213.43(-3)	11.14	11.16	-0.02
19	69210.30(20)	69208.51(-6)	11.54	11.77	-0.23
20	69205.22(19)	69203.46(-26)	12.13	12.37	-0.24
21	69199.92(16)	69198.17(-44)	12.82	12.97	-0.15
22	69194.45(18)	69192.40(34)	13.40	13.58	-0.18
23	69188.57(-2)	69186.52(34)	14.09	14.18	-0.09
24	69182.68(-5)	69180.36(27)	14.45	14.78	-0.33
25	69176.35(-34)	69174.12(31)	15.37	15.38	-0.01
26	69169.88(-59)	69167.31(-4)		15.99	

[a] Calculated using Eq. 4.2.

[b] $\Delta_2F''(J)^{obs.} - \Delta_2F''(J)^{calc.}$ in cm^{-1} units.

[c] Observed-calculated residuals in units of 10^{-2} cm^{-1}.

Table XIX. Transition wavenumbers (cm^{-1}), branch assignments, and ground state combinations, $\Delta_2F''(J)$ (in cm^{-1}), for the (193, 0) band of $^{81}Br^{35}Cl$.

J	$R(J)$	$P(J)$	$\Delta_2F''(J)^{obs.}$	[a] $\Delta_2F''(J)^{calc.}$	[b] $\Delta(\Delta_2F''(J))^{o-c}$
7		69321.98(-9)[c]		4.53	
8	69321.69(-1)[c]	69320.43(18)		5.13	
9	69319.78(-4)	69318.15(-7)	5.67	5.74	-0.07
10	69317.59(-13)	69316.02(5)	6.37	6.34	+0.03
11	69315.36(-3)	69313.41(-7)	6.85	6.94	-0.09
12	69312.85(2)	69310.75(-3)	7.26	7.54	-0.28
13	69309.95(-9)	69308.11(26)	8.15	8.15	0
14	69306.84(-16)	69304.70(2)	8.42	8.75	-0.33
15	69303.63(-10)	69301.53(25)	9.26	9.36	-0.10
16	69300.24(2)	69297.58(-7)	9.79	9.96	-0.17
17	69296.42(-4)	69293.84(7)		10.56	
18	69292.48(4)			11.16	

[a] Calculated using Eq. 4.2.

[b] $\Delta_2F''(J)^{obs.} - \Delta_2F''(J)^{calc.}$ in cm^{-1} units.

[c] Observed-calculated residuals in units of 10^{-2} cm^{-1}.

Table XX. Transition wavenumbers (cm^{-1}), branch assignments, and ground state combinations, $\Delta_2F''(J)$ (in cm^{-1}), for the (195, 0) band of $^{81}Br^{35}Cl$.

J	$R(J)$	$P(J)$	$\Delta_2F''(J)^{obs}$	[a] $\Delta_2F''(J)^{calc}$	[b] $\Delta(\Delta_2F''(J))^{o-c}$
9		69411.23(19)[c]		5.74	
10	69411.60(21)[c]	69409.43(2)		6.34	
11	69409.43(2)	69407.33(12)	6.74	6.94	-0.20
12	69407.70(2)	69404.86(4)	7.50	7.54	-0.04
13	69405.20(-13)	69402.37(13)	7.95	8.15	-0.20
14	69402.37(-43)	69399.75(27)	8.64	8.75	-0.11
15	69399.91(-16)	69396.57(5)	8.75	9.36	-0.61
16	69396.97(-18)	69393.62(25)	9.75	9.96	-0.21
17	69394.11(7)	69390.16(13)	10.16	10.56	-0.40
18	69390.59(-15)	69386.81(30)		11.16	
19	69387.28(2)			11.77	

[a] Calculated using Eq. 4.2

[b] $\Delta_2F''(J)^{obs.} - \Delta_2F''(J)^{calc.}$ in cm^{-1} units.

[c] Observed-calculated residuals in units of 10^{-2} cm^{-1}.

Table XXI. Transition wavenumbers (cm^{-1}), branch assignments, and ground state combinations, $\Delta_2F''(J)$ (in cm^{-1}), for the (196, 0) band of $^{81}Br^{35}Cl$.

J	$R(J)$	$P(J)$	$\Delta_2F''(J)^{obs.}$	[a] $\Delta_2F''(J)^{calc.}$	[b] $\Delta(\Delta_2F''(J))^{o-c}$
6		69473.10(0)[c]		3.92	
7	69472.70(16)[c]	69471.40(-3)		4.53	
8	69470.97(19)	69469.47(-7)	5.25	5.13	+0.12
9	69468.91(10)	69467.44(4)	6.15	5.74	+0.41
10	69466.59(-1)	69464.82(-23)	6.75	6.34	+0.41
11	69464.21(4)	69462.16(-30)	7.00	6.94	+0.06
12	69461.56(6)	69459.60(-6)	7.58	7.54	+0.04
13	69458.73(12)	69456.62(1)	8.23	8.15	+0.08
14	69455.52(3)	69453.33(-3)	8.92	8.75	+0.17
15	69452.18(3)	69449.81(-5)	9.47	9.36	+0.11
16	69448.55(-2)	69446.05(-9)	9.96	9.96	0
17	69444.80(3)	69442.22(3)	10.45	10.56	-0.11
18	69440.82(8)	69438.10(9)	11.10	11.16	-0.06
19	69436.50(2)	69433.70(10)	11.82	11.77	+0.05
20	69431.81(-19)	69428.9992)	12.47	12.37	+0.10
21	69427.40(11)	69424.04(-7)		12.97	
22	69422.21(-11)			13.58	

[a] Calculated using Eq. 4.2.

[b] $\Delta_2F''(J)^{obs.} - \Delta_2F''(J)^{calc.}$ in cm^{-1} units.

[c] Observed-calculated residuals in units of 10^{-2} cm^{-1}.

Table XXII. Transition wavenumbers (cm^{-1}), branch assignments, and ground state combinations, $\Delta_2F''(J)$ (in cm^{-1}), for the (198, 0) band of $^{81}Br^{35}Cl$.

J	$R(J)$	$P(J)$	$\Delta_2F''(J)^{obs.}$	[a] $\Delta_2F''(J)^{calc.}$	[b] $\Delta(\Delta_2F''(J))^{o-c}$
5		69573.97(1)[c]		3.32	
6	69573.97(1)[c]	69572.35(-12)		3.92	
7	69572.35(-12)	69570.81(-5)	4.76	4.53	+0.23
8	69570.81(-5)	69569.11(7)	5.21	5.13	+0.08
9	69569.11(7)	69567.14(12)	5.98	5.74	+0.24
10	69567.14(12)	69564.83(3)	6.70	6.34	+0.36
11	69564.83(3)	69562.32(-6)	7.32	6.94	+0.38
12	69562.32(-6)	69559.82(4)	7.80	7.54	+0.26
13	69559.82(4)	69557.03(5)	8.23	8.15	+0.08
14	69557.03(5)	69554.09(9)	9.18	8.75	+0.43
15	69554.09(9)	69550.64(-21)	9.59	9.36	+0.23
16	69550.64(-21)	69547.44(-7)	10.07	9.96	+0.11
17	69547.44(-7)	69544.02(1)	10.21	10.56	-0.35
18	69544.02(1)	69540.43(8)		11.16	
19	69540.43(8)			13.58	

[a] Calculated using Eq. 4.2.

[b] $\Delta_2F''(J)^{obs.} - \Delta_2F''(J)^{calc.}$ in cm^{-1} units.

[c] Observed-calculated residuals in units of 10^{-2} cm^{-1}.

Table XXIII. Transition wavenumbers (cm^{-1}), branch assignments, and ground state combinations, $\Delta_2F''(J)$ (in cm^{-1}), for the (199, 0) band of $^{81}Br^{35}Cl$.

J	$R(J)$	$P(J)$	$\Delta_2F''(J)^{obs.}$	[a] $\Delta_2F''(J)^{calc.}$	[b] $\Delta(\Delta_2F''(J))^{o-c}$
6		69619.93(-1)[c]		3.92	
7	69619.93(-1)[c]	69618.12(-16)		4.53	
8	69618.12(-16)	69616.55(-12)	5.56	5.13	+0.42
9	69616.40(29)	69614.37(-22)	6.03	5.74	+0.29
10	69614.15(17)	69612.10(-20)	6.70	6.34	+0.36
11	69611.70(8)	69609.70(-8)	7.14	6.94	+0.20
12	69609.22(18)	69607.01(-3)	7.53	7.54	-0.01
13	69606.43(19)	69604.17(10)	8.20	8.15	+0.05
14	69603.20(-1)	69601.02(12)	8.92	8.75	+0.17
15	69600.15(18)	69597.50(2)	9.51	9.36	+0.15
16	69596.49(-1)	69593.69(-16)	10.10	9.96	+0.14
17	69592.72(-9)	69590.05(4)	10.57	10.56	+0.01
18	69588.84(-6)	69585.91(-2)		11.16	
19	69584.71(-6)	69581.52(-13)		11.77	
20	69580.41(0)			12.37	

[a] Calculated using Eq. 4.2.

[b] $\Delta_2F''(J)^{obs.} - \Delta_2F''(J)^{calc.}$ in cm^{-1} units.

[c] Observed-calculated residuals in units of 10^{-2} cm^{-1}.

Table XXIV. Transition wavenumbers (cm^{-1}), branch assignments, and ground state combinations, $\Delta_2F''(J)$ (in cm^{-1}), for the (181, 0) band of $^{81}Br^{37}Cl$.

J	$R(J)$	$P(J)$	$\Delta_2F''(J)^{obs.}$	[a] $\Delta_2F''(J)^{calc.}$	[b] $\Delta(\Delta_2F''(J))^{o-c}$
5	68444.81(5)[c]	68443.63(-5)[c]		3.19	
6	68443.62(-5)	68442.31(-6)	3.88	3.78	+0.10
7	68442.31(-6)	68440.92(3)	4.36	4.36	0
8	68440.92(3)	68439.26(4)	4.97	4.94	+0.03
9	68439.26(4)	68437.34(-1)	5.66	5.52	+0.14
10	68437.34(-1)	68435.26(-2)	6.23	6.10	+0.13
11	68435.26(-2)	68433.03(1)	6.73	6.68	+0.05
12	68433.03(1)	68430.61(6)	7.36	7.26	+0.10
13	68430.61(6)	68427.90(1)	8.01	7.85	+0.16
14	68427.90(1)	68425.01(-2)	8.71	8.42	+0.29
15	68425.01(-2)	68421.89(-8)	9.13	9.00	+0.13
16	68421.89(-8)	68418.77(5)		9.58	
17	68418.77(5)			10.16	

[a] Calculated using Eq. 4.2.
[b] $\Delta_2F''(J)^{obs.} - \Delta_2F''(J)^{calc.}$ in cm^{-1} units.
[c] Observed-calculated residuals in units of 10^{-2} cm^{-1}.

Table XXV. Transition wavenumbers (cm^{-1}), branch assignments, and ground state combinations, $\Delta_2F''(J)$ (in cm^{-1}), for the (182, 0) band of $^{81}Br^{37}Cl$.

J	$R(J)$	$P(J)$	$\Delta_2F''(J)^{obs.}$	[a] $\Delta_2F''(J)^{calc.}$	[b] $\Delta(\Delta_2F''(J))^{o-c}$
8	68517.50(-8)[c]	68517.10(18)[c]		4.94	
9	68515.46(9)	68514.49(-13)	5.66	5.52	+0.14
10	68513.10(17)	68511.84(-22)	6.22	6.10	+0.12
11	68510.25(-1)	68509.25(-3)	6.80	6.68	+0.12
12	68507.24(-11)	68506.30(5)	7.29	7.26	+0.03
13	68504.33(10)	68502.96(-3)	7.70	7.85	-0.15
14	68501.01(13)	68499.55(4)	8.44	8.42	+0.02
15	68497.43(11)	68495.89(9)	9.20	9.00	+0.20
16	68493.49(-8)	68491.81(-7)	9.84	9.58	+0.26
17	68489.56(-5)	68487.59(-15)	10.22	10.16	+0.06
18	68485.57(12)	68483.27(-13)		10.74	

[a] Calculated using Eq. 4.2.
[b] $\Delta_2F''(J)^{obs.} - \Delta_2F''(J)^{calc}$ in cm^{-1} units
[c] Observed-calculated residuals in units of 10^{-2} cm^{-1}.

Table XXVI. Transition wavenumbers (cm^{-1}), branch assignments, and ground state combinations, $\Delta_2F''(J)$ (in cm^{-1}), for the (186, 0) band of $^{81}Br^{37}Cl$.

J	$R(J)$	$P(J)$	$\Delta_2F''(J)^{obs.}$	[a] $\Delta_2F''(J)^{calc.}$	[b] $\Delta(\Delta_2F''(J))^{o-c}$
7	68750.44(3)[c]	68749.85(18)[c]		4.36	
8	68748.47(12)	68748.10(22)	4.92	4.94	-0.02
9	68745.97(-8)	68745.52(4)	5.84	5.52	+0.32
10	68743.75(22)	68742.64(-20)	6.12	6.10	+0.02
11	68740.94(16)	68739.86(-10)	6.88	6.68	+0.20
12	68737.72(-10)	68736.87(3)	7.58	7.26	+0.32
13	68734.84(18)	68733.36(-16)	7.76	7.85	-0.09
14	68731.31(1)	68729.96(-2)	8.81	8.42	+0.39
15	68727.81(3)	68726.03(-20)		9.00	

[a] Calculated using Eq. 4.2.

[b] $\Delta_2F''(J)^{obs.} - \Delta_2F''(J)^{calc.}$ in cm^{-1} units

[c] Observed-calculated residuals in units of 10^{-2} cm^{-1}.

Table XXVII. Transition wavenumbers (cm^{-1}), branch assignments, and ground state combinations, $\Delta_2F''(J)$ (in cm^{-1}), for the (188, 0) band of $^{81}Br^{37}Cl$.

J	$R(J)$	$P(J)$	$\Delta_2F''(J)^{obs.}$	[a] $\Delta_2F''(J)^{calc.}$	[b] $\Delta(\Delta_2F''(J))^{o-c}$
4		68841.59(5)[c]		2.61	
5	68841.59(5)[c]	68840.50(6)		3.19	
6	68840.50(6)	68839.17(5)	3.97	3.78	+0.19
7	68839.17(5)	68837.62(3)	4.74	4.36	+0.38
8	68837.62(3)	68835.75(-12)	5.27	4.94	+0.32
9	68835.75(-12)	68833.90(-4)	5.84	5.52	+0.32
10	68833.90(-4)	68831.78(-2)	6.31	6.10	+0.21
11	68831.78(-2)	68829.44(-1)	6.81	6.68	+0.13
12	68829.44(-1)	68827.09(-2)	7.58	7.26	+0.32
13	68826.93(24)	68824.20(6)	8.22	7.85	+0.37
14	68824.20(6)	68821.22(-21)	8.75	8.42	+0.33
15	68821.07(15)	68818.18(-9)	9.39	9.00	+0.39
16	68817.82(11)	68814.81(-10)	9.90	9.58	+0.32
17	68814.31(2)	68811.17(-16)	10.24	10.16	+0.08
18	68810.85(21)	68807.57(3)	10.97	10.74	+0.23
19	68806.79(1)	68803.34(-20)	11.73	11.32	+0.41
20	68802.73(2)	68799.12(-20)	11.84	11.90	-0.06
21	68797.84(-58)	68794.95(7)	11.88	12.49	-0.61
22	68793.83(-6)	68790.84(62)		13.07	
23	68789.24(9)			13.64	

[a] Calculated using Eq. 4.2.

[b] $\Delta_2F''(J)^{obs.} - \Delta_2F''(J)^{calc.}$ in cm^{-1} units.

[c] Observed-calculated residuals in units of 10^{-2} cm^{-1}.

Table XXVIII. Transition wavenumbers (cm^{-1}), branch assignments, and ground state combinations, $\Delta_2F''(J)$ (in cm^{-1}), for the (189, 0) band of $^{81}Br^{37}Cl$.

J	$R(J)$	$P(J)$	$\Delta_2F''(J)^{obs.}$	[a] $\Delta_2F''(J)^{calc.}$	[b] $\Delta(\Delta_2F''(J))^{o-c}$
8	68907.17(19)[c]	68906.38(2)[c]		4.94	
9	68904.80(6)	68903.84(-19)	5.72	5.52	+0.20
10	68902.07(-19)	68901.45(-1)	6.09	6.10	-0.01
11	68899.56(1)	68898.71(7)	6.61	6.68	-0.07
12	68896.81(22)	68895.47(-12)	6.99	7.26	-0.27
13	68893.17(-23)	68892.56(28)	8.04	7.85	+0.19
14	68889.86(-13)	68888.77(2)	8.34	8.42	-0.08
15	68886.54(19)	68884.83(-15)	9.02	9.00	+0.02
16	68882.50(1)	68880.84(-14)	9.60	9.58	+0.02
17	68878.51(9)	68876.94(18)	10.28	10.16	+0.12
18	68874.08(-6)	68872.22(-10)		10.74	

[a] Calculated using Eq. 4.2.

[b] $\Delta_2F''(J)^{obs.} - \Delta_2F''(J)^{calc.}$ in cm^{-1} units

[c] Observed-calculated residuals in units of 10^{-2} cm^{-1}.

Table XXIX. Transition wavenumbers (cm^{-1}), branch assignments, and ground state combinations, $\Delta_2F''(J)$ (in cm^{-1}), for the (195, 0) band of $^{81}Br^{37}Cl$.

J	$R(J)$	$P(J)$	$\Delta_2F''(J)^{obs.}$	[a] $\Delta_2F''(J)^{calc.}$	[b] $\Delta(\Delta_2F''(J))^{o-c}$
4		69224.44(-8)[c]		2.61	
5	69224.27(5)[c]	69223.34(-4)		3.19	
6	69222.92(-10)	69222.41(39)	4.16	3.78	+0.38
7	69221.64(5)	69220.11(-34)	4.51	4.36	+0.15
8	69220.42(47)	69218.41(-25)	5.07	4.94	+0.13
9	69218.24(14)	69216.57(-8)	5.45	5.52	-0.07
10	69215.69(-33)	69214.97(54)	6.29	6.10	+0.19
11	69213.78(6)	69211.95(-5)	6.65	6.68	-0.03
12	69211.25(5)	69209.04(-30)	7.67	7.26	-0.41
13	69208.55(9)	69206.1?(-35)	7.85	7.85	0
14	69205.36(-14)	69203.40(4)	8.50	8.42	+0.08
15	69202.40(8)	69200.06(1)	8.92	9.00	-0.08
16	69199.09(19)	69196.44(-6)	9.79	9.58	+0.21
17	69195.28(3)	69192.60(-13)	10.38	10.16	+0.22
18	69191.35(-3)	69188.72(-2)	10.82	10.74	+0.08
19	69187.19(-9)	69184.46(-5)	10.10	11.32	-0.22
20	69182.98(4)	69180.36(30)		11.90	
21	69178.25(-11)			12.49	

[a] Calculated using Eq. 4.2.

[b] $\Delta_2F''(J)^{obs} - \Delta_2F''(J)^{calc.}$ in cm^{-1} units.

[c] Observed-calculated residuals in units of 10^{-2} cm^{-1}.

Table XXX. Transition wavenumbers (cm^{-1}), branch assignments, and ground state combinations, $\Delta_2F''(J)$ (in cm^{-1}), for the (197, 0) band of $^{81}Br^{37}Cl$.

J	$R(J)$	$P(J)$	$\Delta_2F''(J)^{obs.}$	[a] $\Delta_2F''(J)^{calc}$	[b] $\Delta(\Delta_2F''(J))^{o-c}$
7	69337.15(37)[c]	69336.18(10)[c]		4.36	
8	69334.75(-2)	69333.98(-21)	5.01	4.94	+0.07
9	69332.66(14)	69332.14(30)	5.75	5.52	+0.23
10	69330.03(1)	69329.01(-24)	6.32	6.10	+0.22
11	69327.21(-8)	69326.34(-7)	6.67	6.68	-0.01
12	69324.33(-1)	69323.37(3)	7.28	7.26	+0.02
13	69321.32(16)	69319.93(-10)	8.06	7.85	+0.21
14	69317.88(10)	69316.27(-23)	8.76	8.42	+0.34
15	69314.33(16)	69312.56(-18)	9.12	9.00	+0.12
16	69310.30(-7)	69308.76(-1)	9.63	9.58	+0.05
17	69306.32(-6)	69304.70(8)	9.93	10.16	-0.23
18	69302.22(3)	69300.37(16)	10.81	10.74	+0.07
19	69297.81(-2)	69295.51(-12)		11.32	

[a] Calculated using Eq. 4.2.

[b] $\Delta_2F''(J)^{obs} - \Delta_2F''(J)^{calc}$ in cm^{-1} units.

[c] Observed-calculated residuals in units of 10^{-2} cm^{-1}.

Table XXXI. Transition wavenumbers (cm^{-1}), branch assignments, and ground state combinations, $\Delta_2F''(J)$ (in cm^{-1}), for the (199, 0) band of $^{81}Br^{37}Cl$.

J	$R(J)$	$P(J)$	$\Delta_2F''(J)^{obs.}$	[a] $\Delta_2F''(J)^{calc.}$	[b] $\Delta(\Delta_2F''(J))^{o-c}$
4	69436.71(26)[c]	69436.64(41)[c]		2.61	
5	69435.13(-3)	69434.75(-14)	3.35	3.19	+0.16
6	69433.75(14)	69433.36(8)	3.97	3.78	+0.19
7	69431.97(15)	69431.16(-25)	4.60	4.36	+0.24
8	69429.37(-41)	69429.16(-14)	4.98	4.94	+0.04
9	69427.50(-1)	69426.99(7)	5.24	5.52	-0.28
10	69425.01(2)	69424.14(-17)	6.25	6.10	+0.15
11	69422.31(6)	69421.25(-20)	6.91	6.68	+0.23
12	69419.26(-2)	69418.11(-26)	7.42	7.26	+0.16
13	69416.09(-2)	69414.89(-16)	7.81	7.85	-0.04
14	69413.06(34)	69411.45(-5)	8.35	8.42	-0.07
15	69409.41(26)	69407.74(-1)	8.78	9.00	-0.22
16	69405.27(-11)	69404.29(49)	9.63	9.58	+0.05
17	69401.00(-43)	69399.78(14)		10.16	

[a] Calculated using Eq. 4.2.

[b] $\Delta_2F''(J)^{obs.} - \Delta_2F''(J)^{calc.}$ in cm^{-1} units.

[c] Observed-calculated residuals in units of 10^{-2} cm^{-1}.

Table XXXII. Transition wavenumbers (cm^{-1}), branch assignments, and ground state combinations, $\Delta_2F''(J)$ (in cm^{-1}), for the (200, 0) band of $^{81}Br^{37}Cl$.

J	$R(J)$	$P(J)$	$\Delta_2F''(J)^{obs.}$	[a] $\Delta_2F''(J)^{calc.}$	[b] $\Delta(\Delta_2F''(J))^{o-c}$
10	69484.20(25)[c]			6.10	
11	69481.65(5)		7.17	6.68	+0.49
12	69478.85(-18)	69477.04(19)[c]	7.27	7.26	+0.01
13	69476.23(-2)	69474.38(9)	7.59	7.85	-0.26
14	69473.16(-7)	69471.26(13)	8.58	8.42	+0.16
15	69469.81(-20)	69467.65(-11)	8.88	9.00	-0.12
16	69466.75(20)	69464.28(12)	9.76	6.58	-0.18
17		69460.05(-30)	10.23	10.16	+0.07
18		69456.52(22)		10.74	

[a] Calculated using Eq. 4.2.
[b] $\Delta_2F''(J)^{obs.} - \Delta_2F''(J)^{calc.}$ in cm^{-1} units.
[c] Observed-calculated residuals in units of 10^{-2} cm^{-1}.

Table XXXIII. Transition wavenumbers (cm^{-1}), branch assignments, and ground state combinations, $\Delta_2F''(J)$ (in cm^{-1}), for the (203, 0) band of $^{81}Br^{37}Cl$.

J	$R(J)$	$P(J)$	$\Delta_2F''(J)^{obs.}$	[a] $\Delta_2F''(J)^{calc.}$	[b] $\Delta(\Delta_2F''(J))^{o-c}$
7		69633.53(33)[c]		4.36	
8	69633.10(19)[c]	69631.52(-11)		4.94	
9	69631.80(10)	69629.88(-1)	5.25	5.52	-0.27
10	69629.88(-1)	69627.85(-6)	6.11	6.10	+0.1
11	69627.76(-18)	69625.70(-6)	6.32	6.68	-0.36
12	69625.49(-26)	69623.56(18)	6.64	7.26	-0.62
13	69623.56(18)	69621.11(26)	7.46	7.85	-0.39
14	69620.72(-3)	69618.04(2)	8.23	8.42	-0.19
15	69618.04(2)	69615.33(19)	8.60	9.00	-0.40
16	69614.60(-29)	69612.12(15)	9.87	9.58	+0.29
17	69611.86(23)	69608.17(-42)	10.09	10.16	-0.07
18	69608.64(50)	69604.52(-46)	10.68	10.74	-0.06
19	69604.38(-3)	69601.18(3)	11.18	11.32	-0.14
20	69600.10(-34)	69597.45(37)	11.61	11.90	-0.29
21	69596.50(27)	69592.77(-2)	12.05	12.49	-0.44
22	69592.48(72)	69588.05(-21)	13.35	13.07	+0.28
23	69586.29(-75)	69583.15(-33)	13.61	13.65	-0.04
24	69582.04(-1)	69578.87(42)		14.23	

[a] Calculated using Eq. 4.2.

[b] $\Delta_2F''(J)^{obs.} - \Delta_2F''(J)^{calc.}$ in cm^{-1} units.

[c] Observed-calculated residuals in units of 10^{-2} cm^{-1}.

Table XXXIV. Rotational constants (in cm^{-1}) for the analyzed vibrational bands of the $E0^+ \leftarrow X0^+$ transition of $^{79}Br^{35}Cl$.

(v', 0)	υ_0 (cm^{-1})	B_v' (cm^{-1})	$10^5 D_v'$ (cm^{-1})	σ^a (cm^{-1})
(173, 0)	68235.06 (26)	0.0354 (11)	.....[b]	0.07
(174, 0)	68295.96 (22)	0.03342 (82)	.....[b]	0.08
(175, 0)	68356.50 (31)	0.0389 (11)	.....[b]	0.09
(182, 0)	68759.00 (52)	0.0428 (51)	0.9 (10)	0.10
(183, 0)	68819.10 (39)	0.0302 (41)	0.31 (85)	0.09
(189, 0)	69146.60 (28)	0.0360 (10)	.....[b]	0.09
(192, 0)	69301.04 (42)	0.0395 (22)	0.15 (22)	0.12
(196, 0)	69515.29 (36)	0.0374 (14)	.....[b]	0.11
(197, 0)	69571.6 (14)	0.046 (15)	1.1 (34)	0.17
(198, 0)	69612.52 (54)	0.0474 (29)	.....[b]	0.13

[a]Standard deviation of the least-squares fit.
[b]Parameter not determined statistically.

Table XXXV. Rotational constants (in cm^{-1}) for the analyzed vibrational bands of the $E0^+ \leftarrow X0^+$ transition of $^{81}Br^{35}Cl$.

(v', 0)	υ_0 (cm^{-1})	B_v' (cm^{-1})	$10^5 D_v'$ (cm^{-1})	σ^a (cm^{-1})
(175, 0)	68318.58 (45)	0.0390 (16)	.....[b]	0.13
(182, 0)	68719.98 (44)	0.0257 (18)	.....[b]	0.11
(183, 0)	68780.40 (39)	0.0252 (40)	-0.70 (81)	0.08
(189, 0)	69107.14 (80)	0.013 (13)	-2.3 (44)	0.15
(192, 0)	69260.3 (12)	0.0116 (84)	-1.3 (12)	0.32
(193, 0)	69328.7 (10)	0.044 (12)	0.9 (28)	0.12
(195, 0)	69421.0 (11)	0.0573 (45)	.....[b]	0.19
(196, 0)	69478.33 (39)	0.0369 (16)	.....[b]	0.11
(198, 0)	69577.68 (93)	0.042 (12)	-1.4 (29)	0.10
(199, 0)	69425.30 (56)	0.0400 (23)	.....[b]	0.14

[a]Standard deviation of the least-squares fit.
[b]Parameter not determined statistically.

Table XXXVI. Rotational constants (in cm^{-1}) for the analyzed vibrational bands of the $E0^+ \leftarrow X0^+$ transition of $^{81}Br^{37}Cl$.

(v', 0)	υ_0 (cm^{-1})	B_v' (cm^{-1})	$10^5 D_v'$ (cm^{-1})	σ^a (cm^{-1})
(181, 0)	68447.10 (25)	0.051 (25)	.....[b]	0.05
(182, 0)	68526.4 (13)	0.019 (17)	-1.5 (32)	0.11
(186, 0)	68757.7 (18)	0.009 (26)	-3.3 (85)	0.15
(188, 0)	68843.98 (52)	0.0473 (91)	0.41 (75)	0.09
(189, 0)	68915.47 (95)	0.022 (14)	.....[b]	0.18
(195, 0)	69227.11 (68)	0.0367 (28)	.....[b]	0.22
(197, 0)	69343.8 (12)	0.016 (18)	-1.7 (29)	0.10
(199, 0)	69439.0 (12)	0.012 (18)	-2.3 (55)	0.24
(200, 0)	69495.3 (19)	0.0351 (86)	.....[b]	0.19
(203, 0)	69639.0 (20)	0.050 (24)	.....[b]	0.32

[a]Standard deviation of the least-squares fit.
[b]Parameter not determined statistically.

4.1.3. Vibrational assignments

In spite of the decrease in spectral complexity provided by the TOF method, vibrational quantum numbering proved difficult since large fluctuations in the band intensities were still evident in TOF detection mode. To get an estimate of the vibrational numbering, we refitted the isotopic $E \leftarrow X$ transition wavenumbers, υ_i, for $v' \leq 2$ calculated from the published constants [6] to the following mass-reduced mixed near dissociation expansion (NDE)/Dunham expansion appropriate for an ion-pair ← ground state transition (in cm^{-1}, Ref. 7-9):

$$\upsilon_i = T_e' + D_e' - \frac{R_y}{X^2}\left(1+\frac{a_3}{X}\right) - \rho_i \frac{(444.276)}{2} + \rho_i^2 \frac{(1.843)}{4} - \rho_i^3 \frac{(0.004)}{8}. \qquad (4.4)$$

Here, X is defined as $[(v_D + \frac{1}{2}) - \rho_i(v' + \frac{1}{2})]$, $\rho_i = [\mu(^{79}Br^{35}Cl)/\mu_i]^{1/2}$, where μ_i is the reduced mass of a particular BrCl isotopomer, T_e' and D_e' are E-state electronic origin and dissociation energy, respectively, and R_y is the Rydberg constant for $^{79}Br^{35}Cl$ (4.84729×10^9 cm^{-1}). The second and third term in Eq. 4.4 represent the correct limiting behavior for the term values in an ion-pair R^{-1} potential. The fourth term, proportional to the constant a_3, is empirical, and accounts for the fact that the observed vibrational levels lie well below the dissociation limit. The remaining terms are members of the mass-reduced Dunham expression for the $v'' = 0$ ground state level of the molecule.

The similarity between the second and third terms of Eq. 4.4 and the well-known Rydberg formula for the electronic energy levels of hydrogenic atoms is not coincidental because both systems are Coulombically bound. Just as the H atom supports an infinite number of electronic states characterized by the principle quantum number n, an ion-pair potential energy curve will support an infinite number of vibrational levels having quantum numbers $\{v'\}$. In this context, the parameter v_D can be viewed as a quantum defect, although for well-behaved term values, it must be negative [10].

In many instances, NDEs require fewer parameters than traditional Dunham expansions for fitting large data sets and they have robust extrapolation properties because they incorporate the proper physical behavior of the vibrational levels as

dissociation is approached [11]. The results of the nonlinear least squares fit are given in Table XXXVII. The standard deviation of the fit was ≈ 0.5 cm^{-1}.

Table XXXVII. Near dissociation expansion (NDE) coefficients (in cm^{-1}) for the $E0^+$ ion-pair state of $^{79}Br^{35}Cl$.

Parameter	Value (cm^{-1})
D_e	35780.0[a]
v_D	-350.355 (16)[b]
a_3	33.782 (77)

[a]Constrained
[b]v_D is unitless

A total of ≈ 120 (v', 0) isotopic vibrational bands with 170 ≤ v' ≤ 213 are predicted from Eq. 4.4 to lie between 146.8 nm and 143.3 nm. Consider first the $^{79}Br^{35}Cl$ isotopomer. The vibrational intervals for the 30 bands in this region are predicted to decrease smoothly from ≈ 59 cm^{-1} (at v' = 179) to 51 cm^{-1} (v' = 209). Approximate BrCl $E0^+$ (v') ← $X0^+$ (v'' = 0, 1, 2) Franck-Condon factors (FCFs) are presented graphically in Fig. 4.5. They were obtained from vibrational overlap integrals calculated by first constructing a Rydberg-Klein-Rees (RKR) curve for the X state [12] and a Morse-RKR potential [12, 13] for $E0^+$, and then solving for their respective vibrational wave functions by using a Numerov-Cooley procedure [14]. It is seen in Fig. 4.5, that transition from v'' = 0 to v' between ≈ 165 and ≈ 180 have the strongest FCFs. In addition, the calculations indicate that the FCFs for hot band transitions originating from v'' = 1 are appreciable at the short wavelength end of the experimental observations ($\lambda \approx$ 143.3 nm), while those for transitions from v'' = 2 are nonnegligible in the longer wavelength region ($\lambda \approx$ 146.8 nm). Although jet vibrational temperatures can be higher than that for rotation, all strong transitions were assigned to transitions that originate from v'' = 0, and not hot bands.

To estimate the relative vibrational numbering between different isotopomers, the transition wavenumbers can be written in the harmonic approximation as:

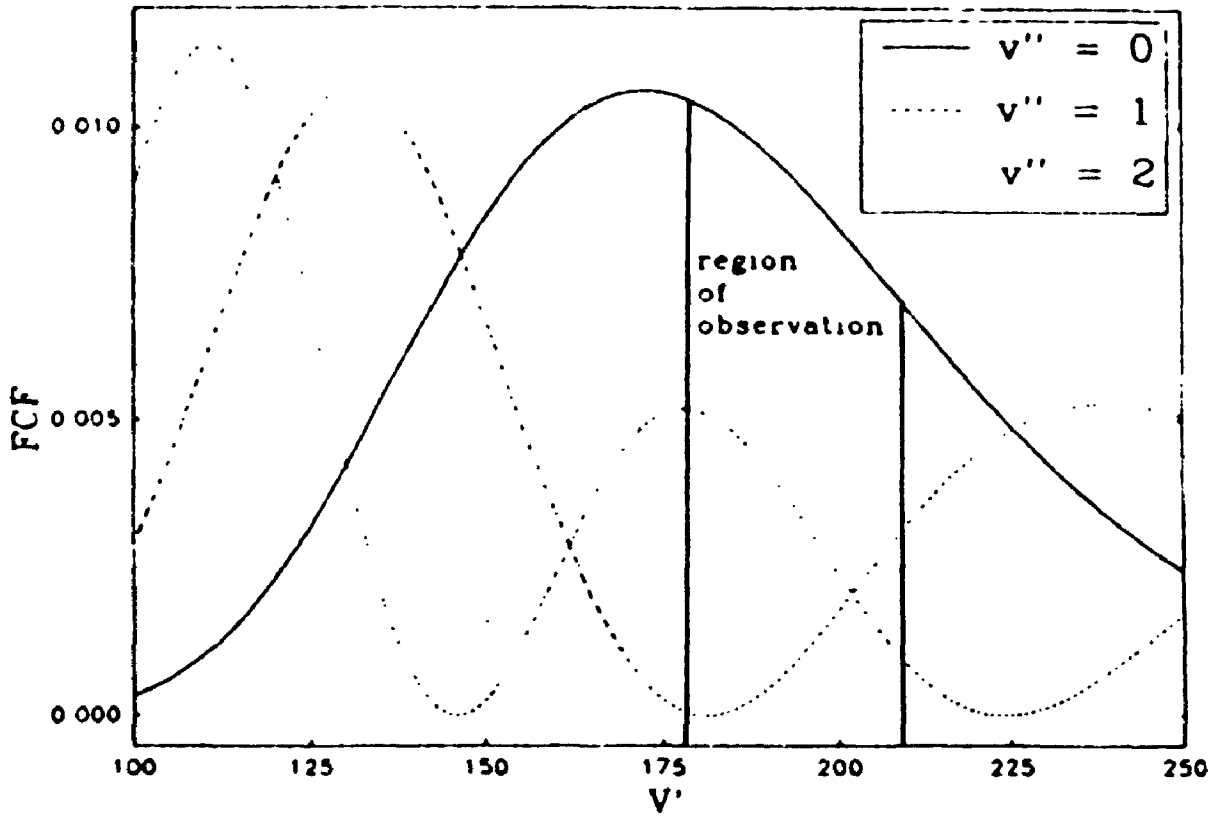

Fig. 4.5. Approximate Franck-Condon factors (FCFs) as a function of the E-state vibrational quantum number, v', for $100 \leq v' \leq 250$, for transitions originating from ground state vibrational levels v'' = 0, 1, and 2. The dark vertical lines bracket the region of observation in this work.

$$\nu^{ref.} \approx \nu_0 + \omega_e' (v' + 1/2) - \omega_e''/2 \qquad (^{79}Br^{35}Cl \text{ is the reference}) \qquad (4.5)$$

$$\nu^{i} \approx \nu_0 + \rho_i \omega_e' (v' + 1/2) - \rho_i \omega_e''/2. \qquad (4.6)$$

Therefore, the isotope shift between the two isotopomers is given by

$$\nu^{ref.} - \nu^{i} \approx (1-\rho_i)\omega_e' (v' + 1/2) - (1-\rho_i) \omega_e''/2 \qquad (4.7)$$

Since the excited state isotope shift is expected to be much greater than that for ground state, the ground state isotope shift can be neglected in Eq. 4.7. Eq 4.7 then simplifies to:

$$\nu^{ref.} - \nu^{i} \approx (1-\rho_i)\omega_e' (v' + 1/2) \approx (1-\rho_i) \Delta G'(v' + 1/2) \qquad (4.8)$$

where $\Delta G'$ is the excited state vibrational spacing whose mean value is about 55 cm^{-1}, as predicted by the NDE expansion. For the $^{81}Br^{35}Cl$ isotopomer, near $v' = 200$, $\nu^{ref} - \nu^{i} \approx$ 42 cm^{-1}, which is smaller than the vibrational interval. On the other hand, for $^{81}Br^{37}Cl$, the excited isotope shift is approximately 254 cm^{-1}, which is 4.6 times vibrational interval. This indicates that the vibrational numbering of the observed bands due to $^{79}Br^{35}Cl$ and $^{81}Br^{35}Cl$ in the same energy region are expected to be the same, while the relative vibrational numbering of the $^{79}Br^{35}Cl$ and $^{81}Br^{37}Cl$ bands are expected to differ by 4 to 5.

To establish the exact relative vibrational number of the isotopic bands within a given frequency interval it is important to consider the concept of crossovers. This has been shown to be an integral feature for the analysis of high vibrational levels in an ion-pair state potential energy curve [10, 15]. If the vibrational quantum numbers of the observed levels are sufficiently large, vibrational isotope shifts can equal and exceed the local vibrational spacings. To a first approximation, the vibrational level, v^0, where the isotope shift equals the vibrational spacing can be calculated according to [10]:

$$v^0 = \rho_i /(1 - \rho_i) \qquad (4.9)$$

where ρ_i for this work is defined as $[\mu(^{79}Br^{35}Cl)/\mu(^{81}Br^{37}Cl)]^{1/2}$. Therefore, the crossover vibrational level v^0 is calculated to ≈ 43; that is, the vibrational term value for level v^0 of $^{79}Br^{35}Cl$ will approximately equal that for level $v^0 + 1$ of $^{81}Br^{35}Cl$. Crossovers are also

expected for integer multiples of v^0 near v' = 86, 129, 172, and so on, with an additional unit increase in the relative numbering of the $^{81}Br^{37}Cl$ bands per v^0 interval (=δ). Crossovers, on the other hand, between bands of the $^{81}Br^{35}Cl$ and $^{79}Br^{35}Cl$ are not expected to occur until v' ≈ 263. The best relative numbering for the $^{79}Br^{35}Cl/^{81}Br^{37}Cl$ features, δ = 4, was chosen from the fit which produced the lowest standard deviation (≈ 4.8 cm^{-1}) [see Fig. 4.6(a)].

To decide on the best absolute vibrational numbering for the rotationally analyzed bands the isotopic band origins and unresolved bandhead frequencies, { υ_i }, were fitted to a mass-reduced Dunham expansion of the form (in cm^{-1}):

$$\upsilon_i = T'_e + \sum_n Y'_{n,0}\left[\rho_i(v'+1/2)\right]^n - \sum_m Y''_{m,0}\left[\rho_i(v''+1/2)\right]^m \qquad (4.10)$$

where T'_e is the electronic origin of the *E*-state, $\{Y'_{n,0}\}$ and $\{Y''_{m,0}\}$ are the *E*-state and *X*-state Dunham parameters, respectively, and ρ_i for this analysis = $[\mu(^{79}Br^{35}Cl)/\mu_i]^{1/2}$, where μ_i is the reduced mass of a particular BrCl isotopomer. In this way the standard mass dependence for the vibrational spacing were accounted for even though those spacings were quite irregular due to perturbations.

The set of excited *E*-state absolute vibrational quantum numbers was then varied in integer steps until the standard deviation of the fit was minimized. Each isotopic band observed in this thesis, labelled by its assigned vibrational transition and frequency, is represented by a horizontal line according to its transition energy in the overall energy level diagram of Fig. 4.7. Rotationally analyzed features are denoted by solid lines, while dashed lines refer to rotationally unresolved bands. The best fit was obtained when the lowest observed $^{79}Br^{35}Cl$ band was assigned to (172, 0) [see Fig. 4.6(b) and 4.7]. Although this vibrational assignment differs by -8 compared to the estimation of NDE expansion, the uncertainty in the Dunham vibrational numbering due to perturbations is at least that large.

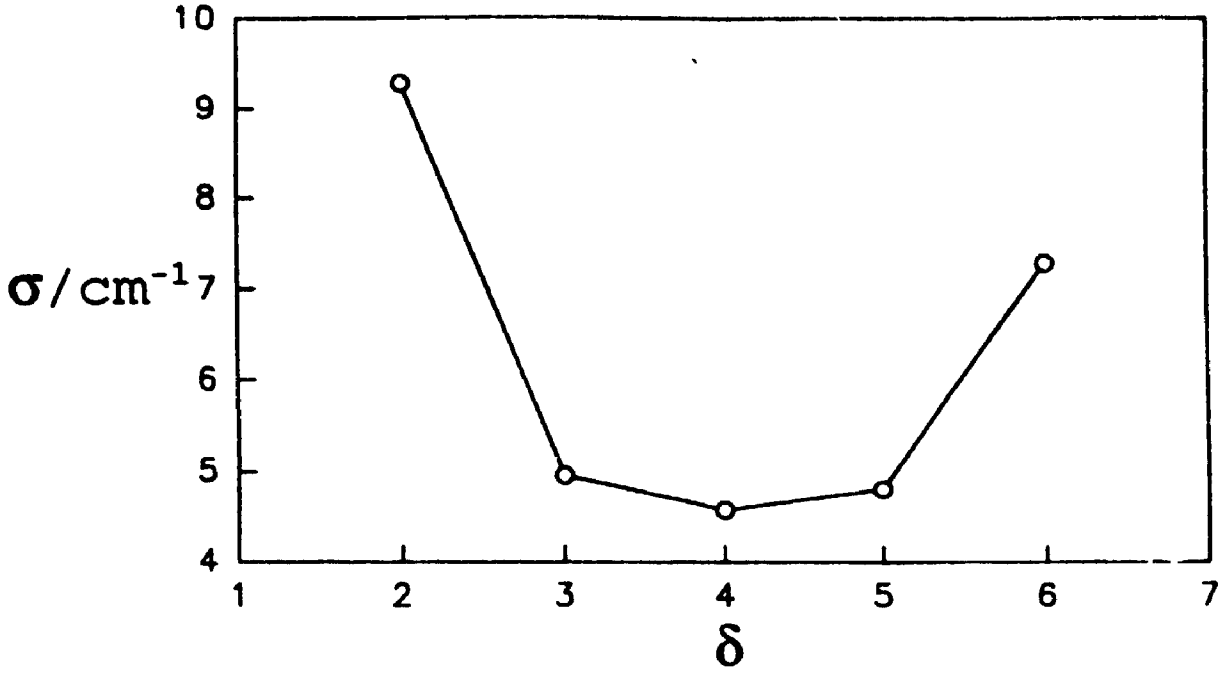

Fig. 4.6 a): The plot of standard deviation, σ, against the relative vibrational numbering, δ, for isotopic bands of BrCl.

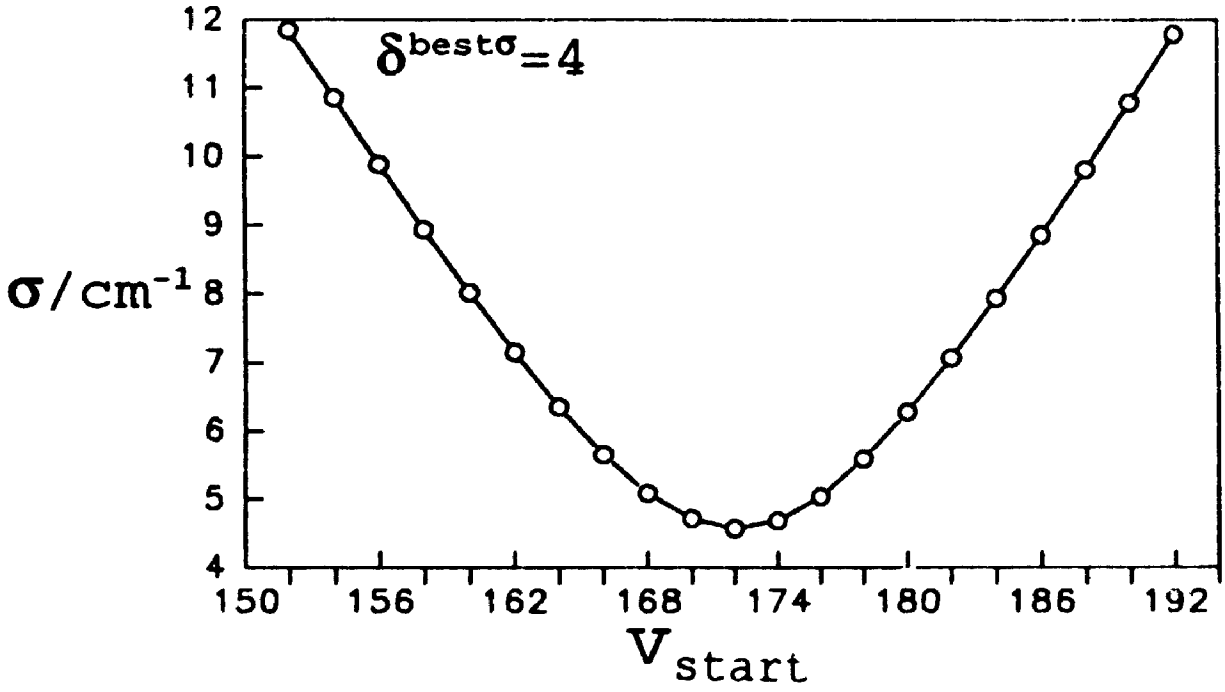

Fig. 4.6 b). Standard deviation, σ, versus the excited state vibrational quantum number of the lowest vibrational level observed for $E0^+ \leftarrow X0^+$ transition of $^{79}Br^{35}Cl$.

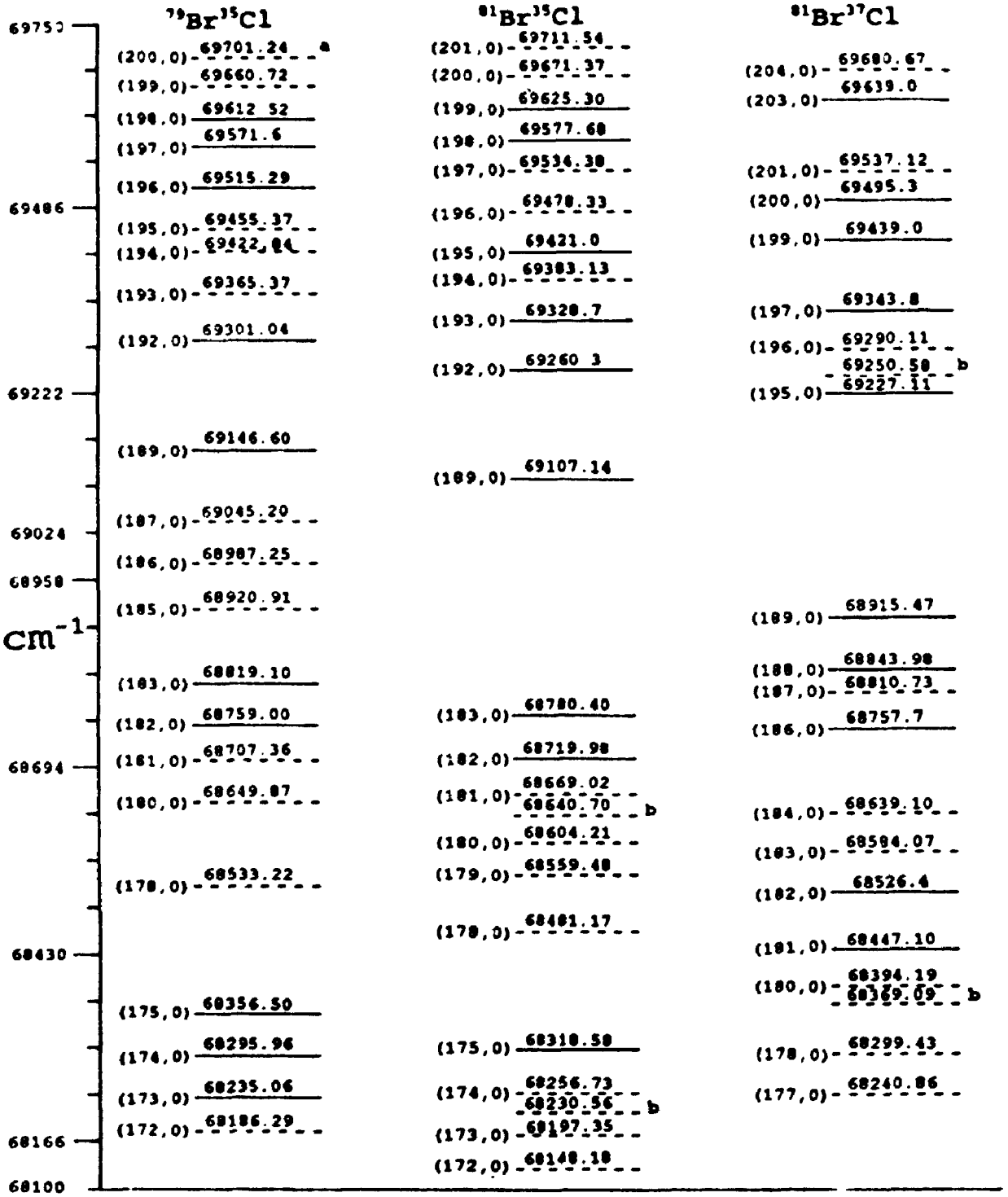

[a]Averaged band head measurements used for all dash lines
[b]Unknown bands not vibrationally assigned

Fig. 4.7. The energy level diagram of all bands observed in $E0^{+} \leftarrow X0^{+}$ transition Rotationally unresolved bands are indicated by the dashed lines and the frequencies reported are bandhead measurements. Rotationally resolved bands are indicated by the solid lines and the frequencies reported are band origins

4.2 Results and Analysis of Cl_2

Single isotopomer spectra of the $2^1\Sigma_u^+(v') \leftarrow X^1\Sigma_g^+(v'' = 0)$ transition of Cl_2 between ~78000 and 80100 cm^{-1} have been recorded, which were amenable to detailed spectroscopic analysis.

4.2.1 Spectra Calibration

The tunable ν_2 dye laser was frequency calibrated by using a small portion of its output to excite the optogalvanic spectrum of neon in an Fe/Ne hollow cathode lamp. The correct two-photon resonance, $4\nu_1$, in the four-wave difference mixing process was attained for each 2-X vibrational band by recording both TOF and fluorescence excitation spectra of the closest CO $A^1\Pi(v') \leftarrow X^1\Sigma^+(v''=0)$ transition, frequency-wise, in separate experiments. Specifically, spectra of the CO A ← X (10, 0), (11, 0), and (12, 0) bands were recorded to calibrate the Cl_2 2-X (1, 0), (2, 0), and (3, 0) bands, respectively. As for BrCl, the change to $4\nu_1$ in each spectral region was determined by comparing the VUV transition wavenumbers calculated using the literature Kr two-photon frequency with those tabulated for CO [2, 3]. It was found that corrections of -0.26 cm^{-1}, +0.26 cm^{-1}, and +0.47 cm^{-1} had to be added to the transition wavenumbers of the CO A ← X (10, 0), (11, 0), and (12, 0) bands, respectively, to bring them into agreement with the literature [3]. Therefore, the same corrections were used correspondingly to adjust the transition wavenumbers in the region of the Cl_2 2 - X (1, 0), (2, 0), and (3, 0) bands. The disagreements between our CO transition wavenumbers and the published results, and the dependence of the correction to the two-photon resonance on the generated VUV wavelength, are probably due to the particular phase-matching conditions which optimized the FWM process in each spectral region.

4.2.2 Vibrational Assignments

The band previously assigned to (0, 0) of Cl_2 between ~78060 and 78200 cm^{-1} is shown in Fig. 4.8. The laser-induced fluorescence spectrum in trace a) exhibits a triplet

due to the presence of three naturally occurring isotopomers of Cl_2 in the jet sample. The relative intensities of the bands forming the triplet are consistent with their natural abundances, but not in perfect agreement. Clearly, the mass assignment for each band is straightforward from the TOF data in traces b) -d).

Each component of the triplet is red-degraded indicating that the bond-length of the excited 2-state is longer than that of the ground state. In addition, rotational structure is partially resolved for all three isotopomers. That analysis will be described in Section 4.23.

The spacings of band heads, ν_h, between adjacent members of the triplet due to the vibrational isotope effect were anticipated to be similar since the mass differences between $^{35}Cl_2$ and $^{35}Cl^{37}Cl$, and between $^{35}Cl^{37}Cl$ and $^{37}Cl_2$, are both 2 amu. The measured isotope splittings are: ν_h ($^{35}Cl_2$) - ν_h ($^{35}Cl^{37}Cl$) =15.9 cm^{-1}, ν_h ($^{35}Cl^{37}Cl$) - ν_h ($^{37}Cl_2$) = 16.95 cm^{-1}. These results suggest that the excited state vibrational level is relatively unperturbed.

From the frequency ordering of the triplet by mass: ν_h ($^{35}Cl_2$) > ν_h ($^{35}Cl^{37}Cl$) > ν_h ($^{37}Cl_2$), the vibrational frequency of the excited state (ω'_e) must be larger than that of the ground state ($\omega''_e \approx 559.7$ cm^{-1} for $^{35}Cl_2$, Ref. 16). This is corroborated by Moeller *et al* who estimated the 2-state vibrational constants to be $\omega'_e = 1040$ cm^{-1} and $\omega_e x'_e = 42$ cm^{-1} [17]. By substituting these parameters and those for ground state [18] into a mass-reduced Dunham expansion, the isotope splittings, ν_h ($^{35}Cl_2$) - ν_h ($^{35}Cl^{37}Cl$) and ν_h ($^{35}Cl^{37}Cl$) - ν_h ($^{37}Cl_2$), were predicted to be ≈ 3, 15, 25, and 32 cm^{-1} for the (0, 0), (1, 0), (2, 0), and (3, 0) bands, respectively. The middle two numbers differ significantly from the (1, 0) splitting of 22 cm^{-1} and (2, 0) splitting of 36 cm^{-1} calculated by Tsukiyama *et al* [19]. However, their estimates of isotope shifts are not valid since they neglected the relatively large mass effect for v'' = 0 of the ground state. Based on the calculations of the isotope splittings from the published 2-state constants and our experimental observations, we believed that the accepted 2-state vibrational numbering should be increased by +1. This change is also supported by the measured isotope shifts of ~ 29 cm^{-1} and 37 cm^{-1} for those features assigned in the literature to (1, 0) and (2, 0), respectively.

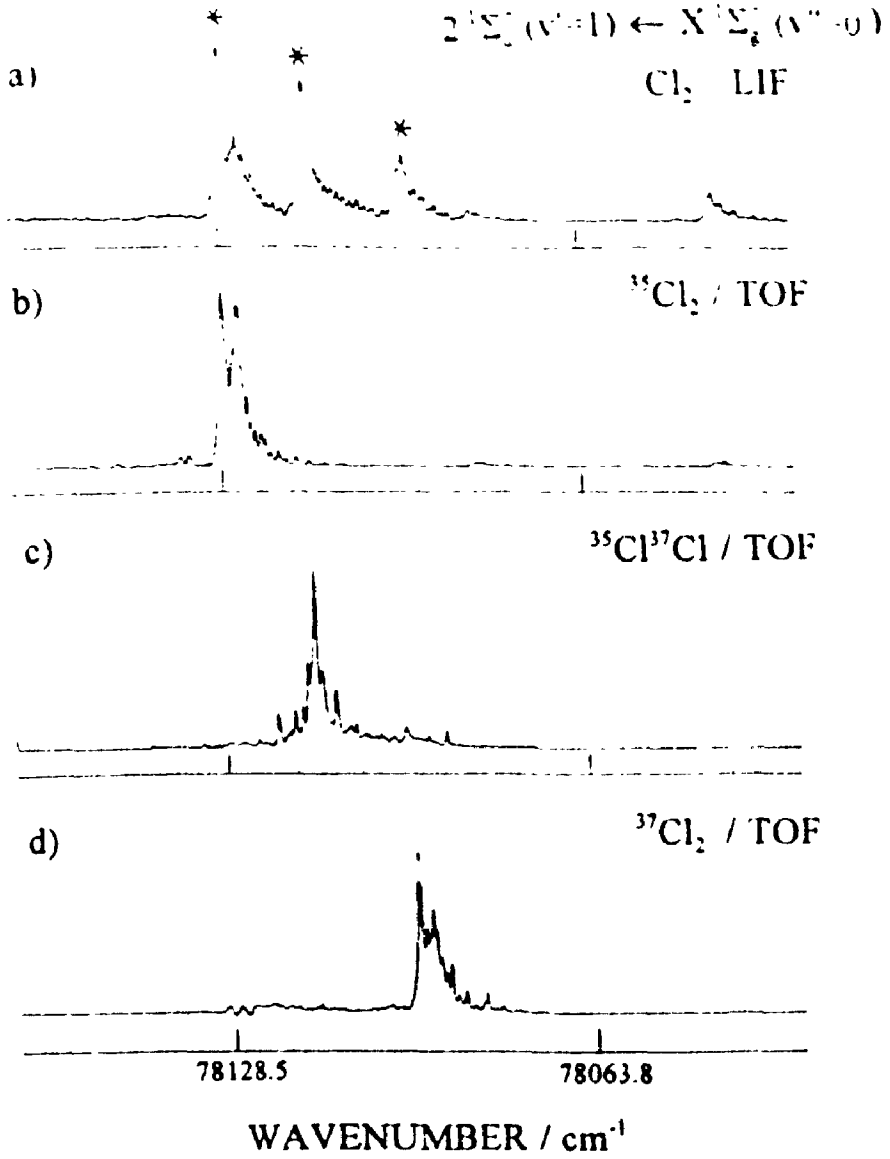

Fig. 4.8 VUV laser excitation spectrum of the $2\,^1\Sigma_u^+$ (v' = 1) ← $X\,^1\Sigma_g^+$ (v'' = 0) transition of Cl_2. (a) VUV laser-induced fluorescence excitation spectrum of a naturally abundant isotopic sample of Cl_2 The features marked with a star are those bands which have been assigned to isotopic components of the 2-X vibrational band The remaining features are unassigned. VUV laser/TOF mass spectrum of the (b) $^{35}Cl_2$, (c) $^{35}Cl^{37}Cl$, and (d) $^{37}Cl_2$ isotopomers.

For this reason, the vibrational band in Fig. 8 is now labeled as (v', v'') = (1, 0) instead of (v', v'') = (0, 0). Similarly, the other group bands, between ~ 78990 and 79080 cm^{-1} shown in Fig. 4.9, and ~ 79980 - 80090 cm^{-1} in Fig. 4.10, are reassigned to (2, 0) and (3, 0).

Unlike (1, 0), the (2, 0) and (3, 0) bands are not simple triplets in our laser induced fluorescence spectra, which is in excellent agreement with published results [19]. As a result, the measured isotope splittings and our choice of which bands actually belong to the 2-X transition could be viewed with suspicion. However, given that (1, 0) appears to be relatively uncontaminated, and that the measured isotope shifts for all three bands examined are in good agreement with predictions, we are confident that the vibrational reassignment is valid.

Additional groups of weaker red-shaded bands were observed between ~ 787050 and ~ 78080 cm^{-1}, ~ 79094 and ~ 78990 cm^{-1}, and ~ 80090 and ~ 79980 cm^{-1}. Although the origin of these extra bands remains uncertain, they do not appear to be 2-X hot bands or vibrational sequences. Since other strong transitions are not expected in this spectral region [20, 21], the large intensities associated with the extra features could be due to perturbations with $2^1\Sigma_u^+$.

The results of the mass analyses for the three reassigned (v', 0) bands of 2-state as well as all other observed bands between ~ 77917 and ~ 80300 cm^{-1} are listed in Table XXXVIII. Assigned isotopic 2-X transition wavenumbers were fitted to a mass-reduced Dunham expansion. When the new excited state numbering was used, the 2-state constants for $^{35}Cl_2$ were found to be T'_e = 77172 (252) cm^{-1}, ω'_e = 760.2 (22.3) cm^{-1}, and $\omega_e x'_e$ = -41.5 (4.5) cm^{-1}. The standard deviation of the fit was 6.2 cm^{-1}. This large uncertainty and the negative sign of the anharmonicity constant are attributed to perturbations. However, the standard deviation of the fit increased by a factor of ≥ 2 when the new 2-state v'-numbering was changed by $\pm$ 1, in support of our reassignment.

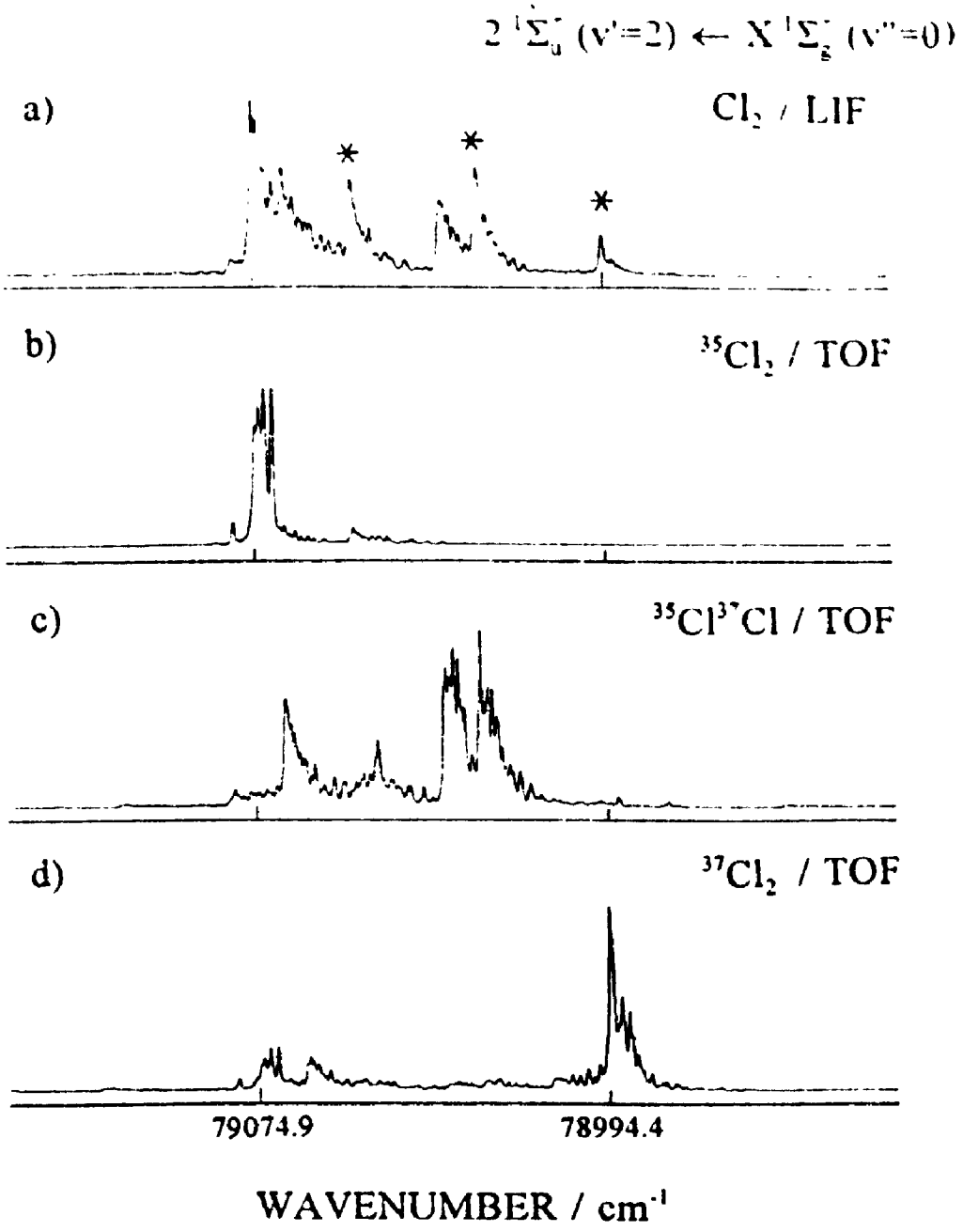

Fig. 4.9. VUV laser excitation spectrum of the $2^1\Sigma_u^+$ (v'=2) ← $X^1\Sigma_g^+$ (v''=0) transition of Cl_2. (a) VUV laser-induced fluorescence excitation spectrum of a naturally abundant isotopic sample of Cl_2. The features marked with a star are those bands which have been assigned to isotopic components of the 2-X vibrational band. the remaining features are unassigned. VUV laser/TOF mass spectrum of the (b) $^{35}Cl_2$, (c) $^{35}Cl^{37}Cl$, and (d) $^{37}Cl_2$ isotopomers.

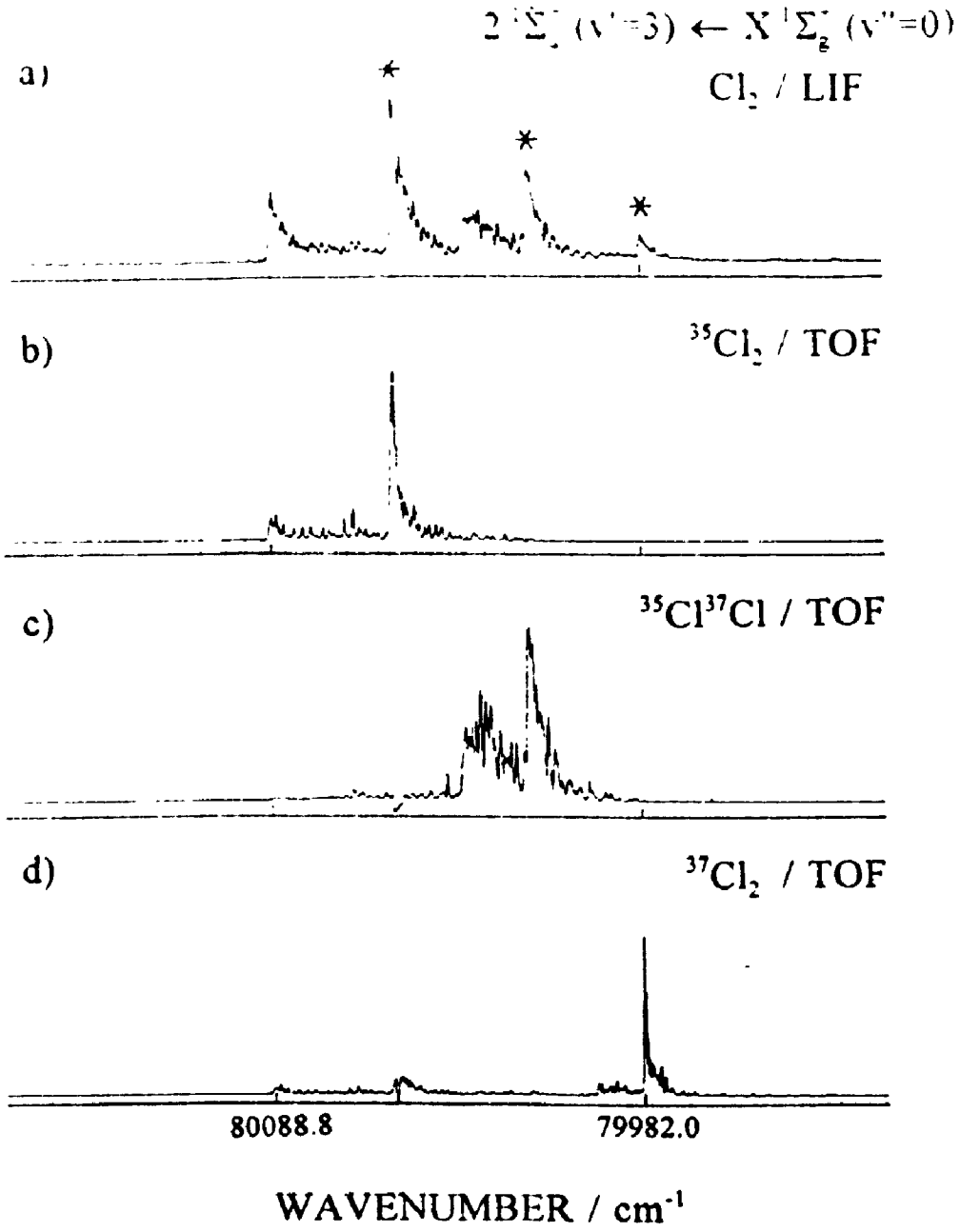

Fig. 4.10. VUV laser excitation spectrum of the $2\,^1\Sigma_u^+$ (v'=3) ← $X\,^1\Sigma_g^+$ (v"=0) transition of Cl_2 (a) VUV laser-induced fluorescence excitation spectrum of a naturally abundant isotopic sample of Cl_2. The features marked with a star are those bands which have been assigned to isotopic components of the 2-X vibrational band. the remaining features are unassigned. VUV laser/TOF mass spectrum of the (b) $^{35}Cl_2$, (c) $^{35}Cl^{37}Cl$, and (d) $^{37}Cl_2$ isotopomers.

Table XXXVIII. Excitation Wavenumber (in cm^{-1}) and Mass Assignment for All Bands in the region of the $2^1\Sigma_u^+$ (v' = 1, 2, 3) ← $X^1\Sigma_g^+$ (v'' = 0) Transitions of Cl_2.

Averaged excitation wavenumber/cm^{-1}	Mass assignment $^mCl^nCl(m, n)$	Transition
77917.05	37, 37	
77931.47	35, 35	
77946.47	35, 37	
77963.72	35, 35	
78001.37	35, 35	
78018.14	35, 37	
78036.20	35, 35	
78042.08	37, 37	
78082.06	35, 35	
78095.39	[a] **37, 37** 35, 37	$2^1\Sigma_u^+(v'=1) \leftarrow X^1\Sigma_g^+(v''=0)$
78112.34	35, 37	$2^1\Sigma_u^+(v'=1) \leftarrow X^1\Sigma_g^+(v''=0)$
78118.77	35, 37	
78128.24	35, 35	$2^1\Sigma_u^+(v'=1) \leftarrow X^1\Sigma_g^+(v''=0)$
78140.98	35, 35	
78461.73	37, 37	
78521.05	35, 35	
78578.44	35, 37	
78593.02	35, 35	
78640.98	35, 35	
78668.54	35, 35	
78713.39	35, 35	
78914.21	35, 35	
78992.40	35, 37	
78994.69	37, 37	$2^1\Sigma_u^+(v'=2) \leftarrow X^1\Sigma_g^+(v''=0)$
79023.30	35, 37	$2^1\Sigma_u^+(v'=2) \leftarrow X^1\Sigma_g^+(v''=0)$
79031.78	35, 37	
79047.94	35, 37	
79052.37	[a] **35, 35** 35, 37	$2^1\Sigma_u^+(v'=2) \leftarrow X^1\Sigma_g^+(v''=0)$
79064.50	[a] **37, 37** 35, 37	
79068.59	35, 37	
79075.13	35, 35	
79137.90	35, 35	
79149.59	37, 37	
79152.13	35, 37	
79176.10	37, 37	
79181.79	35, 37	

continued

continued

79186.47	37, 37	
79202.09	35, 37	
79205.60	35, 35	
79242.27	35, 37	
79265.02	35, 35	
79268.78	35, 37	
79285.76	35, 35	
79307.02	35, 35	
79680.07	37, 37	
79711.62	35, 37	
79727.66	35, 37	
79747.30	35, 35	
79759.01	35, 35	
79801.77	35, 37	
79818.46	35, 35	
79830.01	35, 35	
79859.48	35, 35	
79883.78	35, 35	
79982.43	37, 37	$2^1\Sigma_u^+(v'=3) \leftarrow X^1\Sigma_g^+(v''=0)$
80014.69	35, 37	$2^1\Sigma_u^+(v'=3) \leftarrow X^1\Sigma_g^+(v''=0)$
80033.99	35, 37	
80054.50	35, 35	$2^1\Sigma_u^+(v'=3) \leftarrow X^1\Sigma_g^+(v''=0)$
80089.32	35, 35	
80212.16	37, 37	
80252.20	35, 37	
80299.92	35, 35	

[a]If a feature is an overlap of bands involving different isotopomers, the mass assignment of the strongest component is indicated in boldface type.

The production of atomic $^{35}Cl^+$ and $^{37}Cl^+$ was monitored in TOF detection for all three (v', 0) transitions investigated in this work. The corresponding signals obtained were strong due to excited 2-state predissociation. Isotopic Cl^+ TOF and LIF excitation spectra of the (1, 0) band can be inspected in Fig. 4.11. A comparison of Fig. 8 with Fig. 11 clearly shows that the rotational line intensity distribution in the molecular TOF spectrum differs considerably from that in the atomic TOF data. Furthermore, only the rotational line intensity distributions in the atomic TOF spectra resemble those obtained in VUV LIF. A similar observation was noted for the (2, 0) band, while the rotational envelopes in the atomic and molecular TOF spectra of the (3, 0) band look basically the same.

The rotational line intensity distributions in the LIF and atomic TOF spectra are similar because they originate from the same first VUV excitation step. This interpretation is reasonable since the 2-state is known to be predissociated [22]. If instead, Cl^+ was produced after the production of Cl_2^+ by the (1+1) REMPI process, then the bands in both the atomic and molecular TOF spectra would be expected to look the same.

The unknown electronic state which predissociates the $2^1\Sigma_u^+$ ($v' = 1, 2, 3$) cannot itself dissociate to ground state atoms because the wavelength of the fundamental beams used in the four-wave mixing process and the generated VUV light were not short enough to ionize atomic Cl (ionization potential, IP(Cl) = 104591 cm^{-1}, Ref. 23). More likely, as shown in Fig. 4.12a, one or more electronic states that dissociate to Cl + Cl* $3p^4 4s$ (^4P, ^2P) between 71954.0 and 74861.24 cm^{-1} are responsible [24].

The unusual intensity distribution in the molecular TOF spectra cannot be rationalized by a regular (1 + 1) REMPI process where the second photon excites a transition from the 2-state into a smooth first ionization continuum of Cl_2. If this was the case, the rotational intensity distributions in molecular TOF spectra would be similar to that observed in LIF or atomic TOF detection. To account for this observed difference qualitatively, an additional resonance enhancement in the second step of the (1 + 1) REMPI process is proposed. Specifically, the second step of the ionization process must

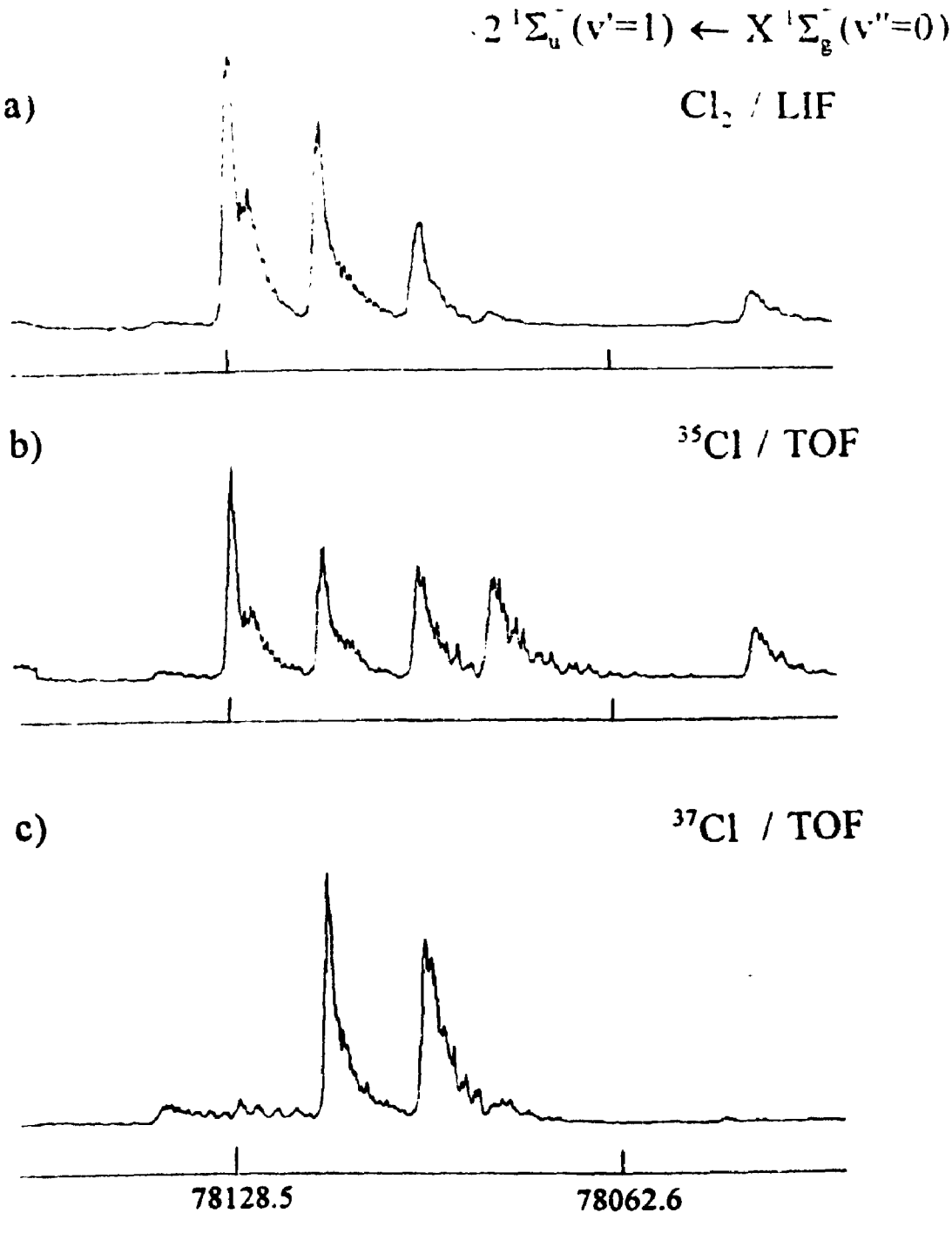

Fig. 4.11. VUV laser excitation spectrum of the $2^1\Sigma_u^+$ ($v' = 1$) $\leftarrow$ $X^1\Sigma_g^+(v'' = 0)$ transition of Cl_2. (a) VUV laser-induced fluorescence excitation spectrum of a naturally abundant isotopic sample of Cl_2. VUV laser/TOF mass spectrum of the (b) ^{35}Cl and (c) ^{37}Cl isotopes.

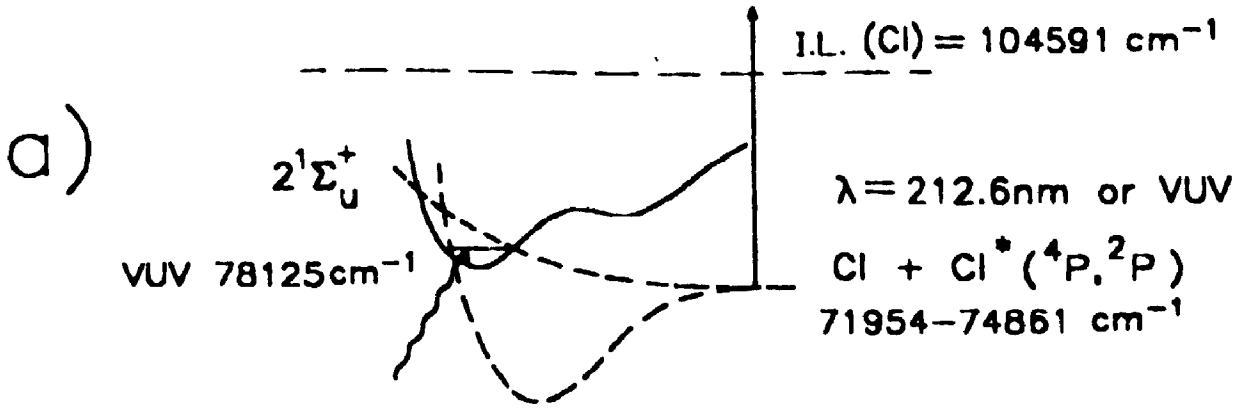

Fig. 4.12a. Schematic of the $2^1\Sigma_u^+$ state potential energy curve The rotational line intensity distribution obtained by detecting atomic Cl ions in TOF can be understood if v' = 1 of the 2-state is predissociated to produce an electronically excited Cl atom, which is subsequently ionized by either the UV fundamental used in the four-wave mixing process, or the generated VUV light itself A similar effect was found for VUV transitions to $2^1\Sigma_u^+$ (v' = 2, 3)

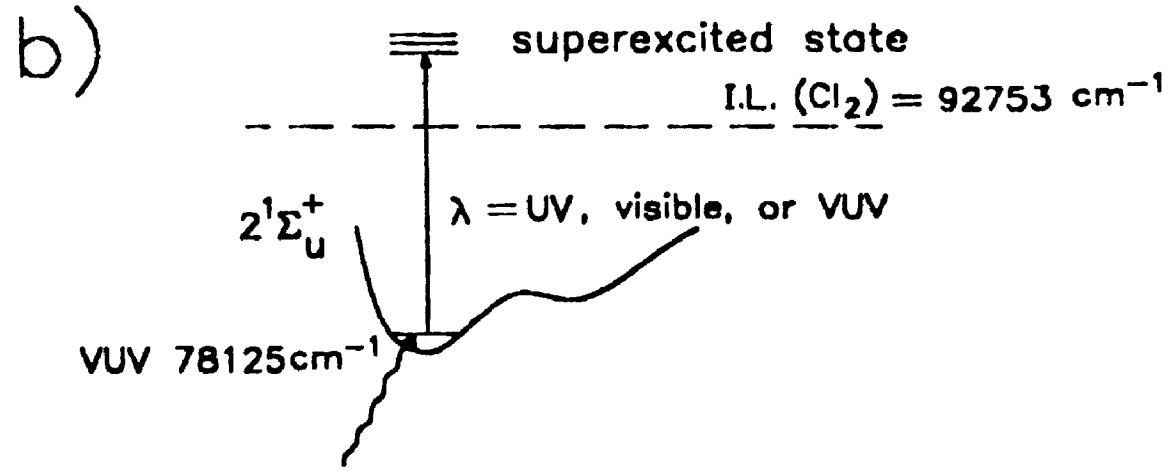

Fig. 4.12b. Schematic of the $2^1\Sigma_u^+$ state potential curve The unusual rotational line intensity distribution obtained by detecting molecular Cl_2 ions in TOF can be understood if the second step in the (1 + 1) REMPI excitation, using v' = 1 of the $2^1\Sigma_u^+$ state as an intermediate, accesses a superexcited state above the ionization limit of the molecule The location of the superexcited state is uncertain because both the UV and visible fundamentals used in the four-wave mixing process and/or the generated VUV itself are able to provide the second photon in the REMPI process. A similar effect was found for $2^1\Sigma_u^+$ (v' = 2) but not for $2^1\Sigma_u^+$ (v' = ?)

be accessing a superexcited state (shown in Fig. 4.12b). Superexcited states are electronic levels lying above the first ionization potential of the molecule, which belong to Rydberg series that converge to an excited state of the ion [25]. Although these states will be subject to autoionization, the superexcited state in this work must be relatively long-lived since the enhancement appears at rotational resolution. If the superexcited state were short-lived, having a large continuum-like bandwidth, this would produce an additional overall resonance enhancement, but the rotational distribution would then be determined by the 2-state. Under our experimental conditions, three possible REMPI schemes were operative for accessing superexcited states since each of the UV and visible fundamental beams ($2\nu_1$ and ν_2, respectively), and the generated VUV light, ($4\nu_1 - \nu_2$), can provide the second photon in the (1 + 1) multiphoton process. Unfortunately, it was not possible to deconvolute each individual contribution because the laser beams were not predispersed before exciting the molecular sample.

Since the molecular TOF spectra of the (3, 0) band were not influenced by additional resonant enhancement, three possible spectral regions where the superexcited state might be found could be determined. If the visible photon took part in the REMPI excitation, then the superexcited state should be located between ~ 107.8 nm, the first ionization limit of Cl_2 (92753 cm^{-1}, Ref. 23), and > 106.4 nm. If the UV photon was involved, then the superexcited state lies at shorter wavelengths between ~ 79.1 and > 78.7 nm. Finally, a two VUV photon excitation places the superexcited state between ~ 64.0 and > 62.5 nm.

Supports for selecting the first region between ~ 108 and 106 nm comes from the synchrotron work of Lee *at el* who found a strong feature between ~ 110 and ~ 106 nm, with a maximum near ~ 108 nm. which they assigned to a ungerade superexcited state [22]. The high fluorescence yield from that state suggests that it is long-lived. Of course, the superexcited state described in this thesis cannot be the same one (at least for the homonuclear isotopomers) due to the g/u selection rules. However, there is no reason to doubt that superexcited states of both parities lie in the same spectral region.

4.2.3. Rotational Analysis

The isotopically identified laser-induced fluorescence excitation spectra were used for rotational analysis because the rotational lines appeared better resolved and the additional resonance enhancement evident in TOF detection leading to the unusual intensity distributions was absent. The branch assignments were relatively straightforward since all bands observed were red-shaded, indicating that the *R* branches form the heads. However, only the *P* branches were rotationally resolved for the spectra recorded. The rotational quantum numbering of the *P* lines, *J*, was determined within ± 2 based on the expectation that an intensity alternation for $^{35}Cl_2$ and $^{37}Cl_2$ would result in odd *J P* lines which were 5/3 times stronger than the even *J* lines. The averaged transition wavenumbers of the assigned *P*(*J*) lines were then fitted to a Dunham expansion of the form given by Eq. 4.3. The rotational numbering was subsequently changed until an optimum fit was obtained. To confirm our rotational assignments, a computer program was written to simulate each isotopic Cl_2 2 (v') - X (v" = 0) transition.

First, an estimate for the rotational temperature of the sample was inputted. By assuming a Boltzmann distribution for the ground state (v" = 0) rotational level populations, the maximum population was expected to reside in $J"_{max}$, where $J"_{max}$ is the integer quantum number closest to that calculated from

$$J"_{max} = (k_B T/2B_0")^{1/2} - 1/2 \qquad (4.11)$$

Here, the Boltzmann constant, $k_B = 0.695\ cm^{-1}$, and $B_0"$ is given in units of cm^{-1}. *P* and *R* line transition wavenumbers were then calculated for J" values up to $10 \times J"_{max}$ using the 2-state rotational constants derived from the least-squares fits of the experimental data.

Each *P* and *R* line, centered at its own frequency, ν_0, was digitally broadened (typically with ≥ 100 points) over a specified frequency range corresponding to the whole band in question using a normalized Lorentzian lineshape function, g(ν), of the form:

$$g(\nu) = \Delta\nu/2\pi[(\nu-\nu_0)^2 + (\Delta\nu/2)^2] \qquad (4.12)$$

where Δν is the inputted width of the line (full width at half-maximum). Each lineshape function was multiplied by the appropriate Boltzmann factor, Hönl-London factor, and

intensity alternation factor (5 for odd J'', 3 for even J'') for the specific J'' level involved in the transition, and co-added to yield the simulated spectrum.

In the beginning, the inputted values of the spectral linewidth and rotational temperature were changed until the best simulation of the (1, 0) band of $^{35}Cl_2$ was achieved ($\Delta\nu$~ 0.7 cm^{-1} and T_{rot} ~ 15 Kelvin). These estimated values were then constrained in the simulations of the other bands. The final rotational J numbering was considered established when the least-squares fit produced a minimum standard deviation and the optimum simulation was achieved.

The generated VUV linewidth was also estimated to be ~ 0.7 cm^{-1} from spectral linewidth measurement of CO VUV fluorescence spectra used to calibrate of the two-photon resonance in the FWDM process. Although the Ci_2 levels are predissociated, it can be concluded that the predissociation rate is not fast enough to make a measurable contribution to the rotational linewidth. If that broadening contribution, $\Delta\nu_p$, could be measured, the predissociation rate, k_p, would then be calculated according to:

$$k_p = 2\,\pi\,\Delta\nu_p\,c \qquad (4.13)$$

where c is the speed of light in cm s^{-1}.

Although there was no intensity alternation in the TOF spectra for the $^{35}Cl^{37}Cl$ isotopomer, the rotational assignments for each band could be made by changing the J numbering of P lines in the Dunham least-square fits until the standard deviations were minimized and the simulations of the spectra were best.

The results of analyses for the (1, 0) band for all three Cl_2 isotopomers are presented in Figs. 4.13-15. The best simulations (b) not only predict the right positions of band heads, $R(J)^{head}$, but also reproduce most features of the spectra closely. Similarly, convincing rotational assignments and simulations for the (2, 0) band of $^{35}Cl_2$, and (3, 0) bands of $^{35}Cl_2$ and $^{35}Cl^{37}Cl$ can be found in Figs. 4.16-18.

Other strong bands observed in this spectral region and labelled as #1 through #7, were also rotationally analyzed. Again, their electronic assignments are uncertain at present. The standard deviations of these fits were reasonable, ranging between 0.02 and 0.26 cm^{-1}.

Transition wavenumbers for each analyzed band are tabulated in Tables XXXIX - LIV. Derived rotational constants are listed in Tables LV - LVII. The B values obtained, ranging from 0.06 to 0.22 cm^{-1}, are quite small compared to that for the ground state of Cl_2 (on the order of 0.24 cm^{-1}, Ref. 18) which is indicative of an ion-pair state, and not a Rydberg state ($B_v \sim 0.26\ cm^{-1}$ [26]).

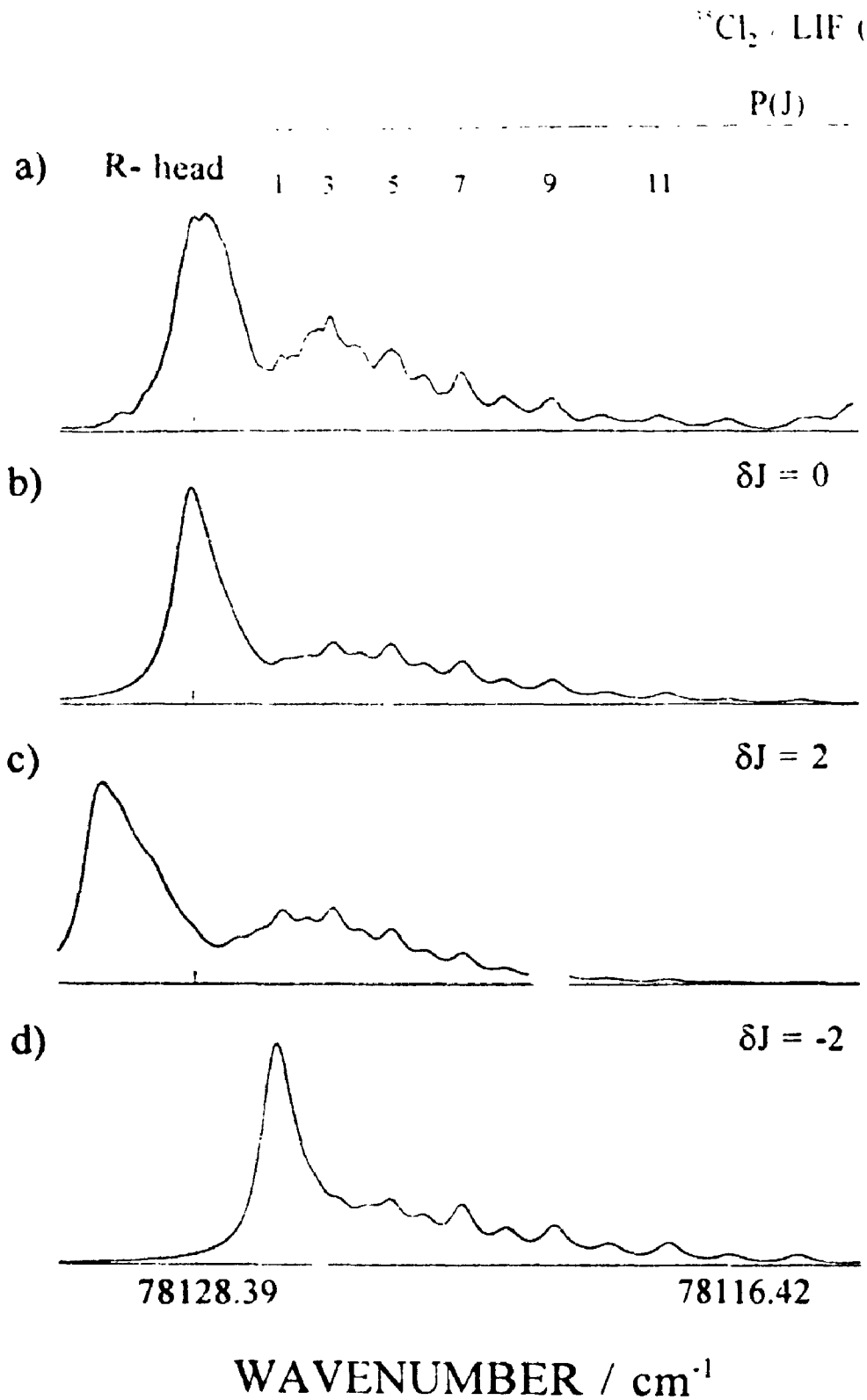

Fig. 4.13 a) A small portion of the LIF spectrum assigned to the $2^1\Sigma_u^+(v'=1) \leftarrow X^1\Sigma_g^+(v''=0)$ transition of $^{35}Cl_2$. b) The best simulation possible; $\delta J = 0$. c) The simulation obtained by changing the set $\{J\}$ by $\delta J = +2$ in the P branch. d) The simulation obtained by changing the set $\{J\}$ by $\delta J = -2$ in the P branch.

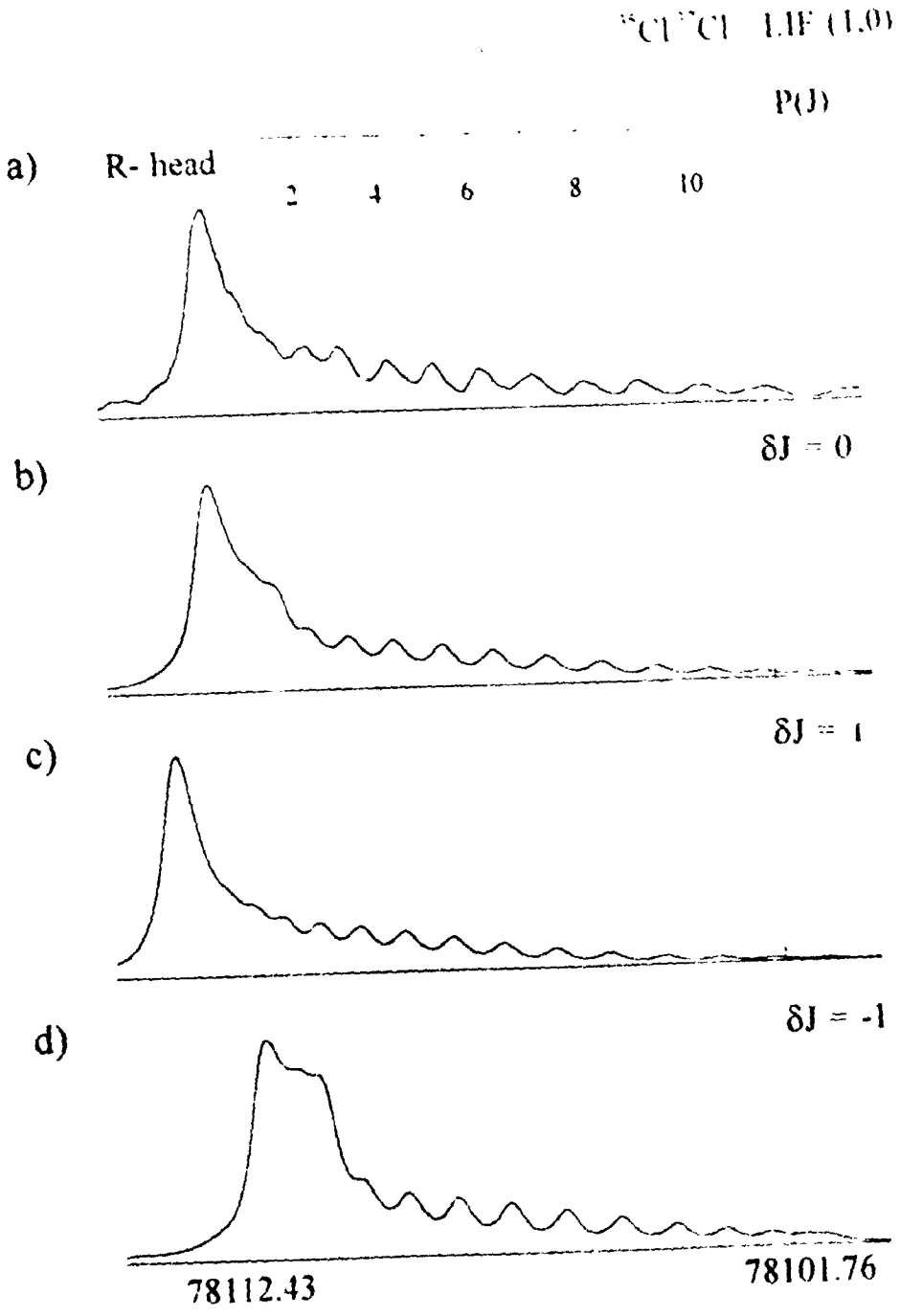

Fig. 4.14. a) A small portion of the LIF spectrum assigned to the $2^1\Sigma_u^+(v'=1) \leftarrow X^1\Sigma_g^+(v''=0)$ transition of $^{35}Cl^{37}Cl$. b) The best simulation possible; $\delta J = 0$. c) The simulation obtained by changing the set $\{J\}$ by $\delta J = +1$ in the P branch. d) The simulation obtained by changing the set $\{J\}$ by $\delta J = -1$ in the P branch

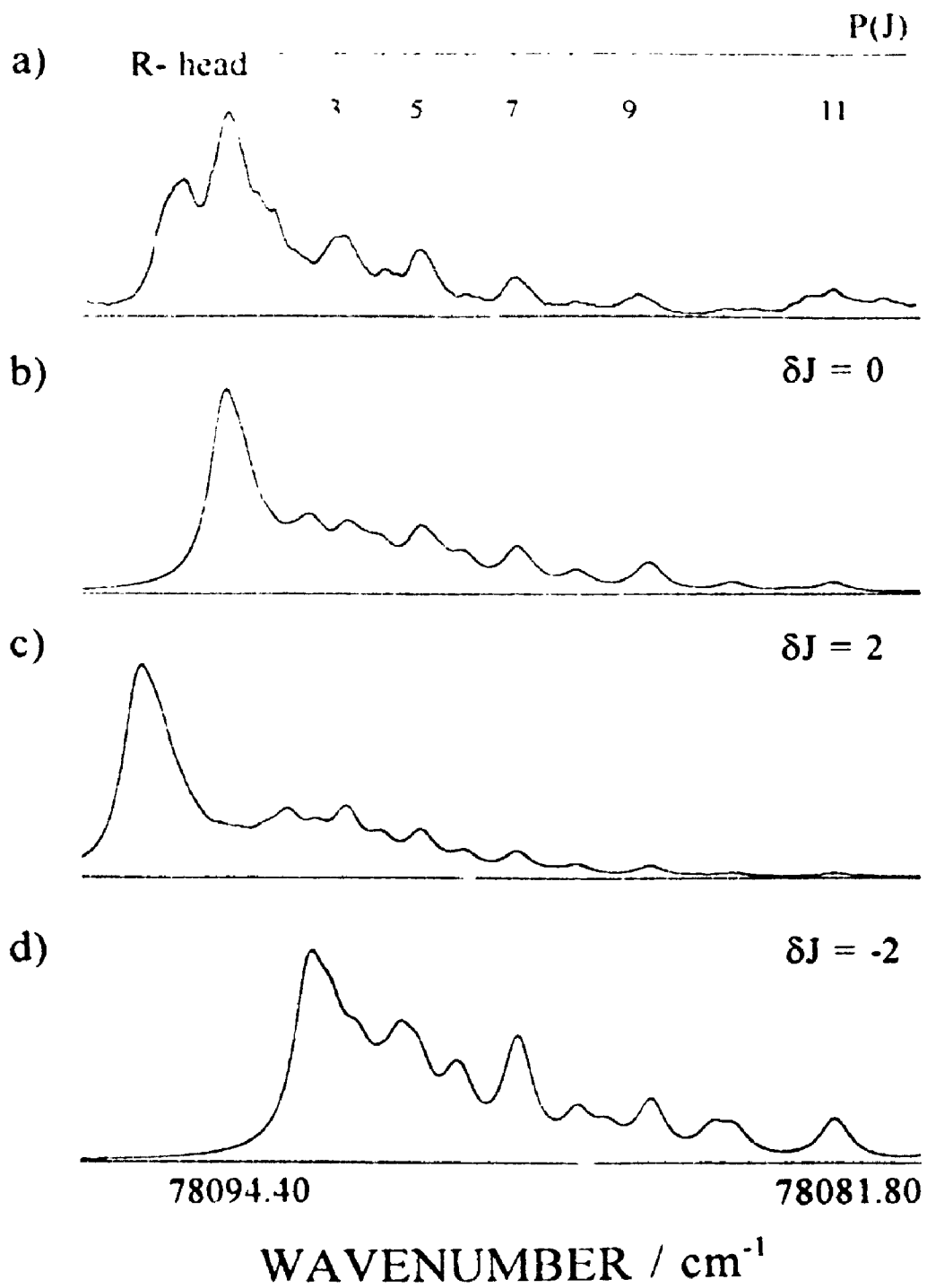

Fig. 4.15 a) A small portion of the LIF spectrum assigned to the $2^1\Sigma_u^+(v'=1) \leftarrow X^1\Sigma_g^+(v''=0)$ transition of $^{37}Cl_2$. b) The best simulation possible; $\delta J = 0$. c) The simulation obtained by changing the set $\{J\}$ by $\delta J = +2$ in the *P* branch. d) The simulation obtained by changing the set $\{J\}$ by $\delta J = -2$ in the *P* branch

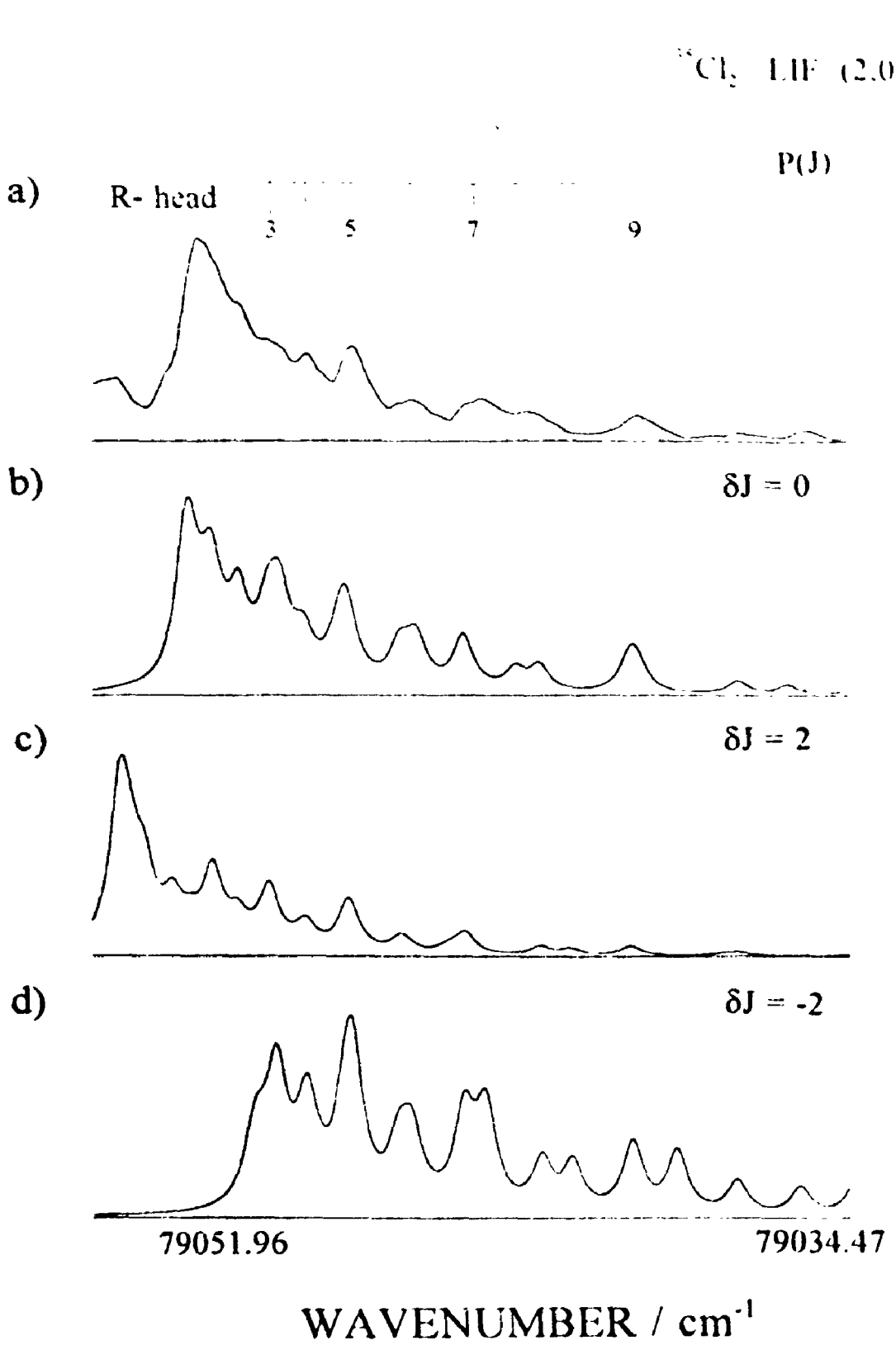

Fig. 4.16. a) A small portion of the LIF spectrum assigned to the $2^1\Sigma_u^+(v'=2) \leftarrow X^1\Sigma_g^+(v''=0)$ transition of $^{35}Cl_2$. b) The best simulation possible; δJ = 0. c) The simulation obtained by changing the set $\{J\}$ by δJ = +2 in the *P* branch. d) The simulation obtained by changing the set $\{J\}$ by δJ = -2 in the *P* branch.

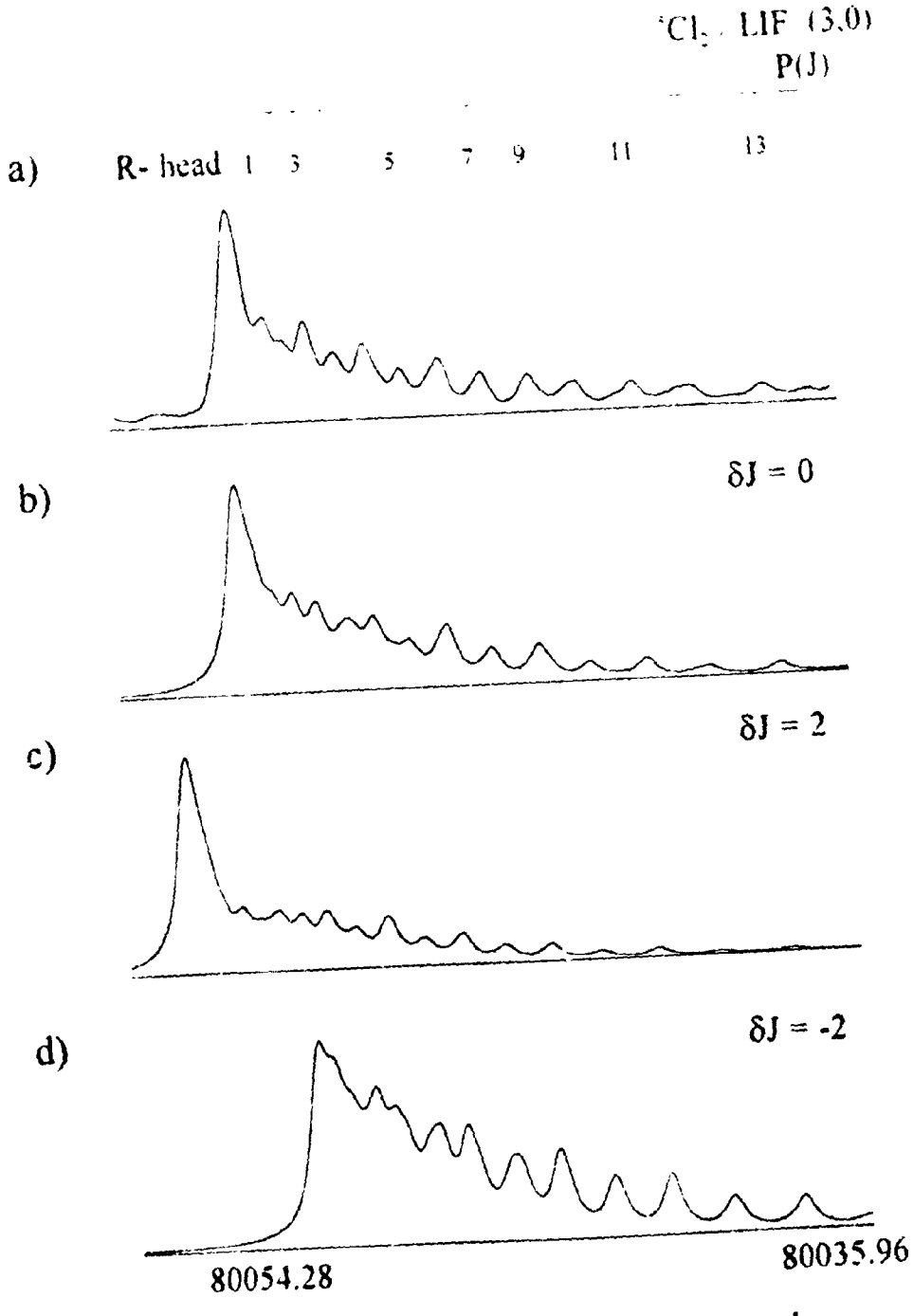

Fig. 4.17. a) A small portion of the LIF spectrum assigned to the $2^1\Sigma_u^+(v'=3) \leftarrow X^1\Sigma_g^+(v''=0)$ transition of $^{35}Cl_2$. b) The best simulation possible; $\delta J = 0$ c) The simulation obtained by changing the set $\{J\}$ by δJ = +2 in the *P* branch. d) The simulation obtained by changing the set $\{J\}$ by δJ = -2 in the *P* branch.

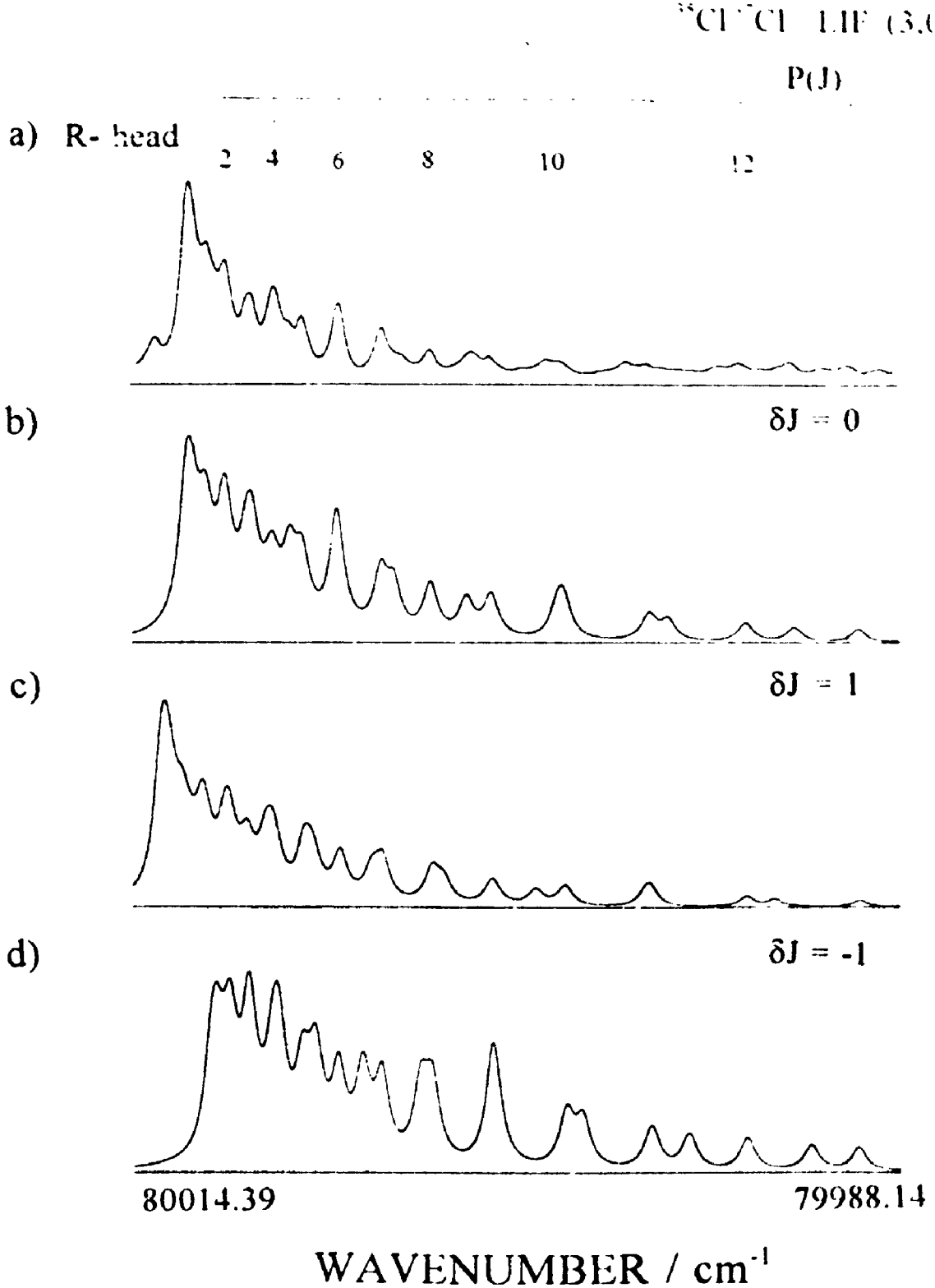

Fig. 4.18. a) A small portion of the LIF spectrum assigned to the $2^1\Sigma_u^+(v'=3) \leftarrow X^1\Sigma_g^+(v''=0)$ transition of $^{35}Cl^{37}Cl$ b) The best simulation possible; $\delta J = 0$. c) The simulation obtained by changing the set $\{J\}$ by $\delta J = +1$ in the P branch. d) The simulation obtained by changing the set $\{J\}$ by $\delta J = -1$ in the P branch.

Table XXXIX. Rotational assignments and transition wavenumbers (in cm^{-1}) for the *P* branch and calculated bandhead of the $2^1\Sigma_u^+(v'=1) \leftarrow X^1\Sigma_g^+(v''=0)$ transition of $^{35}Cl_2$.

J	*P*(*J*)	*R*(*J*)^{head}
1	78126.09(-2)[a]	
2	78125.63(5)	
3	78125.00(0)	
4	78124.38(3)	
5	78123.60(-4)	
6	78122.85(-2)	78128.39[b]
7	78121.99(-4)	
8	78121.11(3)	
9	78120.03(-1)	
10	78118.90(1)	
11	78117.65(6)	
12	78116.10(-4)	

[a]Observed-calculated residuals in units of 10^{-2} cm^{-1}.
[b]Predicted bandhead occurred at *R*(6).

Table XXXX. Rotational assignments and transition wavenumbers (in cm^{-1}) for the *P* branch and calculated bandhead of the $2^1\Sigma_u^+(v'=1) \leftarrow X^1\Sigma_g^+(v''=0)$ transition of $^{35}Cl^{37}Cl$.

J	*P*(*J*)	*R*(*J*)^{head}
2	78110.81(9)[a]	78112.44[b]
3	78110.01(3)	
4	78109.12(-1)	
5	78108.03(-11)	
6	78106.99(-8)	
7	78105.89(-3)	
8	78104.73(2)	
9	78103.56(9)	
10	78102.29(8)	
11	78100.91(-8)	

[a]Observed-calculated residuals in units of 10^{-2} cm^{-1}.
[b]Predicted bandhead occurred at *R*(2).

Table XXXXI. Rotational assignments and transition wavenumbers (in cm^{-1}) for the *P* branch and calculated bandhead of the $2^1\Sigma_u^+(v'=1) \leftarrow X^1\Sigma_g^+(v''=0)$ transition of $^{37}Cl_2$.

J	*P(J)*	$R(J)^{head}$
3	78091.75(10)[a]	78094.3[b]
4	78090.90(-5)	
5	78090.16(0)	
6	78089.12(-12)	
7	78088.15(-1)	
8	78086.91(0)	
9	78085.63(20)	
10	78083.57(-12)	
11	78081.65(1)	

[a]Observed-calculated residuals in units of 10^{-2} cm^{-1}.
[b]Predicted bandhead occurred at *R*(3).

Table XXXXII. Rotational assignments and transition wavenumbers (in cm^{-1}) for the *P* branch and calculated bandhead of the $2^1\Sigma_u^+(v'=2) \leftarrow X^1\Sigma_g^+(v''=0)$ transition of $^{35}Cl_2$.

J	*P(J)*	$R(J)^{head}$
1		79052.6[b]
2		
3	79050.20(5)[a]	
4	79049.16(1)	
5	79047.91(-3)	
6	79046.37(-9)	
7	79044.55(-12)	
8	79042.86(35)	
9	79039.70(-19)	
10	79036.78(2)	

[a]Observed-calculated residuals in units of 10^{-2} cm^{-1}.
[b]Predicted bandhead occurred at *R*(1).

Table XXXXIII. Rotational assignments and transition wavenumbers (in cm^{-1}) for the *P* branch and calculated bandhead of the $2^1\Sigma_u^+(v'=2) \leftarrow X^1\Sigma_g^+(v''=0)$ transition of $^{35}Cl^{37}Cl$.

J	*P(J)*	*R(J)*[head]
0		79023.6[b]
1		
2		
3	79021.09(-9)[a]	
4	79019.65(-29)	
5	79018.67(23)	
6	79016.94(26)	
7	79014.77(9)	
8	79012.35(-6)	
9	79009.69(-20)	
10	79007.17(6)	

[a]Observed-calculated residuals in units of 10^{-2} cm^{-1}.
[b]Predicted bandhead occurred at *R*(0).

Table XXXXIV. Rotational assignments and transition wavenumbers (in cm^{-1}) for the *P* branch and calculated bandhead of the $2^1\Sigma_u^+(v'=2) \leftarrow X^1\Sigma_g^+(v''=0)$ transition of $^{37}Cl_2$.

J	*P*(*J*)	*R*(*J*)^{head}
3	78992.34(4)[a]	78995.12[b]
4	78991.80(-1)	
5	78990.87(-1)	
6	78989.97(8)	
7	78988.92(2)	
8	78987.47(4)	
9	78985.65(10)	
10	78983.07(-10)	
11	78980.18(2)	

[a]Observed-calculated residuals in units of 10^{-2} cm^{-1}.
[b]Predicted bandhead occurred at *R*(3).

Table XXXXV. Rotational assignments and transition wavenumbers (in cm^{-1}) for the *P* branch and calculated bandhead of the $2^1\Sigma_u^+(v'=3) \leftarrow X^1\Sigma_g^+(v''=0)$ transition of $^{35}Cl_2$.

J	*P(J)*	$R(J)^{head}$
1	80053.63 (12)[a]	
2	80083.24(33)	
3	80052.14(-6)	80054.80[b]
4	80051.38(2)	
5	80050.41(-1)	
6	80049.31(-4)	
7	80048.09(-5)	
8	80046.75(-5)	
9	80045.22(-9)	
10	80043.74(7)	
11	80041.87(1)	
12	80039.99(12)	
13	80037.75(3)	
14	80035.22(-8)	

[a]Observed-calculated residuals in units of 10^{-2} cm^{-1}.
[b]Predicted bandhead occurred at *R*(3).

Table XXXXVI. Rotational assignments and transition wavenumbers (in cm^{-1}) for the *P* branch and calculated bandhead of the $2^1\Sigma_u^+(v'=3) \leftarrow X^1\Sigma_g^+(v''=0)$ transition of $^{35}Cl^{37}Cl$.

J	*P(J)*	*R(J)*[bead]
1		80014.85[b]
2	80013.41(12)[a]	
3	80012.39(-10)	
4	80011.46(-3)	
5	80010.32(4)	
6	80008.84(-2)	
7	80007.08(-7)	
8	80005.13(0)	
9	80002.78(4)	
10	79999.96(2)	
11	79996.63(-3)	
12	79992.89(8)	
13	79988.29(-5)	

[a]Observed-calculated residuals in units of 10^{-2} cm^{-1}.
[b]Predicted bandhead occurred at *R*(1).

Table XXXXVII. Rotational assignments and transition wavenumbers (in cm^{-1}) for the *P* branch and calculated bandhead of the $2^1\Sigma_u^+(v'=3) \leftarrow X^1\Sigma_g^+(v''=0)$ transition of $^{37}Cl_2$.

J	*P*(*J*)	*R*(*J*)^{head}
1	79982.08(31)[a]	79982.6[b]
2	79981.11(-1)	
3	79979.97(-32)	
4	79978.95(-31)	
5	79978.06(4)	
6	79976.81(22)	
7	79975.15(25)	
8	79973.20(21)	
9	79970.41(-40)	
10	79968.28(-6)	
11	79965.61(4)	
12	79962.51(5)	

[a]Observed-calculated residuals in units of 10^{-2} cm^{-1}.
[b]Predicted bandhead occurred at *R*(1).

Table XXXXVIII. Rotational assignments and transition wavenumbers (in cm^{-1}) for the *P* branch and calculated bandhead for band #1 near the $2^1\Sigma_u^+(v'=1) \leftarrow X^1\Sigma_g^+(v''=0)$ transition of $^{35}Cl_2$.

J	*P(J)*	$R(J)^{head}$
1		78084.76[b]
2		
3		
4		
5	78079.50(-59)[a]	
6	78077.95(-21)	
7	78076.02(7)	
8	78073.60(15)	
9	78071.00(34)	
10	78067.95(37)	
11	78064.53(31)	
12	78060.71(14)	
13	78056.53(-10)	
14	78051.93(-48)	

[a]Observed-calculated residuals in units of 10^{-2} cm^{-1}.
[b]Predicted bandhead occurred at *R*(1).

Table XXXIX. Rotational assignments and transition wavenumbers (in cm^{-1}) for the *P* branch and calculated bandhead for band #2 near the $2^1\Sigma_u^+(v'=1) \leftarrow X^1\Sigma_g^+(v''=0)$ transition of $^{35}Cl_2$.

J	*P*(*J*)	*R*(*J*)^{head}
0		78036.33[b]
1		
2		
3	78033.89(0)[a]	
4	78032.68(2)	
5	78031.18(-3)	
6	78029.54(-1)	
7	78027.71(3)	
8	78025.64(0)	
9	78023.45(0)	

[a]Observed-calculated residuals in units of 10^{-2} cm^{-1}.
[b]Predicted bandhead occurred at *R*(0).

Table L. Rotational assignments and transition wavenumbers (in cm^{-1}) for the *P* branch and calculated bandhead for band #3 near the $2^1\Sigma_u^+(v'=1) \leftarrow X^1\Sigma_g^+(v''=0)$ transition of $^{35}Cl_2$.

J	*P*(*J*)	*R*(*J*)^{head}
0		78001.87[b]
1		
2		
3	77999.15(19)[a]	
4	77997.48(4)	
5	77995.65(8)	
6	77993.37(2)	
7	77990.81(3)	
8	77987.54(-33)	
9	77984.46(-15)	
10	77980.79(-22)	
11	77977.09(3)	
12	77973.07(31)	

[a]Observed-calculated residuals in units of 10^{-2} cm^{-1}.
[b]Predicted bandhead occurred at *R*(0).

Table LI. Rotational assignments and transition wavenumbers (in cm^{-1}) for the *P* branch and calculated bandhead for band #4 near the $2^1\Sigma_u^+(v'=1) \leftarrow X^1\Sigma_g^+(v''=0)$ transition of $^{35}Cl_2$.

J	*P*(*J*)	*R*(*J*)^{head}
1	77962.60(-8)[a]	
2	77962.11(5)	77963.86[b]
3	77961.36(4)	
4	77960.44(-2)	
5	/7959.49(3)	
6	77958.30(-4)	
7	77957.14(4)	
8	77955.70(-2)	

[a]Observed-calculated residuals in units of 10^{-2} cm^{-1}.
[b]Predicted bandhead occurred at *R*(2).

Table LII. Rotational assignments and transition wavenumbers (in cm^{-1}) for the `` branch and calculated bandhead for band #5 near the $2^1\Sigma_u^+(v'=1) \leftarrow X^1\Sigma_g^+(v''=0)$ transition of $^{35}Cl_2$.

J	*P(J)*	*R(J)*[head]
1		78669.30[b]
2		
3	78666.92(5)[a]	
4	78665.79(9)	
5	78664.14(-13)	
6	78662.53(-3)	
7	78660.40(-14)	
8	78658.19(6)	
9	78655.60(23)	
10	78652.00(-13)	

[a]Observed-calculated residuals in units of 10^{-2} cm^{-1}.
[b]Predicted bandhead occurred at *R*(1).

Table LIII. Rotational assignments and transition wavenumbers (in cm^{-1}) for the *P* branch and calculated bandhead for band #6 near the $2^1\Sigma_u^+(v'=2) \leftarrow X^1\Sigma_g^+(v''=0)$ transition of $^{35}Cl_2$.

J	*P(J)*	$R(J)^{head}$
0		79036.89[b]
1		
2		
3	79304.61(16)[a]	
4	79303.13(-10)	
5	79301.79(3)	
6	79299.83(-21)	
7	79298.10(2)	
8	79295.94(7)	
9	79293.47(6)	
10	79290.68(-3)	

[a]Observed-calculated residuals in units of 10^{-2} cm^{-1}.
[b]Predicted bandhead occurred at *R*(0).

Table LIV Rotational assignments and transition wavenumbers (in cm^{-1}) for the *P* branch and calculated bandhead for band #7 near the $2^1\Sigma_u^+(v'=2) \leftarrow X^1\Sigma_g^+(v''=0)$ transition of $^{35}Cl_2$.

J	*P(J)*	$R(J)^{head}$
1		79285.82[b]
2		
3	79283.32(-24)[a]	
4	79282.22(-2)	
5	79280.89(25)	
6	79278.96(20)	
7	79276.54(-7)	
8	79274.06(-11)	

[a]Observed-calculated residuals in units of 10^{-2} cm^{-1}.
[b]Predicted bandhead occurred at *R*(1).

Table LV. Rotational constants (in cm^{-1}) for the analyzed vibrational bands of the $2^1\Sigma_u^+(v') \leftarrow X^1\Sigma_g^+(v''=0)$ transition of $^{35}Cl_2$.

(v', 0)	ν_0 (cm^{-1})	B'_v (cm^{-1})	$10^3 D'_v$ (cm^{-1})	σ^a (cm^{-1})
(1, 0)	78126.60 (21)	0.2188 (95)	0.079 (75)	0.04
(2, 0)	79052.11 (19)	0.17 (10)	0.4 (10)	0.19
(3, 0)	80053.99 (43)	0.187 (13)	0.051 (74)	0.08
near (1, 0) #1[b]	78669.0 (15)	0.134 (81)	0.27 (84)	0.16
near (1, 0) #2[b]	78084.5 (10)	0.125 (25)	0.13 (12)	0.09
near (1, 0) #3[b]	78036.09 (26)	0.118 (17)	-0.15 (21)	0.02
near (1, 0) #4[b]	78001.76 (80)	0.055 (30)	-0.11 (22)	0.10
near (1, 0) #5[b]	77963.16 (27)	0.1801 (95)	.....[c]	0.05
near (2, 0) #6[b]	79306.65 (76)	0.120 (15)	.....[c]	0.12
near (2, 0) #7[b]	79285.5 (19)	0.14 (15)	0.6 (23)	0.14

[a]Standard deviation of the least-squares fit.
[b]Unknown rotationally analyzed bands.
[c]Parameter not determined statistically.

Table LVI. Rotational constants (in cm^{-1}) for the analyzed vibrational bands of the $2^1\Sigma_u^+(v') \leftarrow X^1\Sigma_g^+(v''=0)$ transition of $^{35}Cl^{37}Cl$.

(v', 0)	ν_0 (cm^{-1})	B'_v (cm^{-1})	$10^3 D'_v$ (cm^{-1})	σ^a (cm^{-1})
(1, 0)	78111.80 (59)	0.170 (29)	-0.15 (26)	0.09
(2, 0)	79023.4 (13)	0.109 (27)	.....[b]	0.21
(3, 0)	80014.40 (42)	0.156 (15)	-0.297 (95)	0.08

[a]Standard deviation of the least-squares fit.
[b]Parameter not determined statistically.

Table LVII. Rotational constants (in cm^{-1}) for the analyzed vibrational bands of the $2^1\Sigma_u^+(v') \leftarrow X^1\Sigma_g^+(v''=0)$ transition of $^{37}Cl_2$.

(v', 0)	ν_0 (cm^{-1})	B'_v (cm^{-1})	$10^3 D'_v$ (cm^{-1})	σ^a (cm^{-1})
(1, 0)	78093.2 (10)	0.195 (46)	0.22 (39)	0.12
(2, 0)	78993.87 (19)	0.211 (23)	0.54 (21)	0.08
(3, 0)	79982.3 (14)	0.137 (63)	0.12 (49)	0.26

[a]Standard deviation of the least-squares fit.

4.3 References

[1]. G. R. Harrison, *M.I.T. tables*. Boston: Technology Press. M.I.T. 1939.

[2]. V. Kaufman and C. J. Humphreys, *J. Opt. Soc. Am.* **59**, 1614 (1969).

[3]. S. G. Tilford and J. D. Simmons, *J. Phys. Chem. Ref. Data* **1**, 147 (1972).

[4]. J. A. Coxon, *J. Mol. Spectrosc.* **50**, 142 (1974).

[5]. G. Herzberg, **Molecular Spectra and Molecular Structure**, 2nd edition, Van Norstrand Reinhold Co. 1950.

[6]. D. K. Chakraborty, P. C. Tellinghuisen, and J. Tellinghuisen, *Chem. Phys. Lett.*, **141**, 36 (1987).

[7]. Dr. R. H. Lipson's work. Dept. of Chem. U.W.O., 1994.

[8]. R. J. LeRoy and R. B. Bernstein, *J. Chem. Phys.*, **52**, 3869 (1970).

[9]. J. LeRoy and W. H. Lam, *Chem. Phys. Lett.*, **71**, 544 (1980).

[10]. R. H. Lipson and A. R. Hoy, *J. Chem. Phys.* **90**, 6821 (1989).

[11]. K. J. Jordan, R. H. Lipson, N. A. McDonald, and R. J. LeRoy, *J. Phys. Chem.*, **96**, 4778 (1992).

[12]. R. J. LeRoy, *Chemical Physics Research Report* **CP-425**, University of Waterloo, 1992.

[13]. J. Tellinghuisen and S. D. Henderson, *Chem. Phys. Lett.* **92**, 447 (1982).

[14]. R. J. LeRoy, *Chemical Physics Research Report* **CP-300**, University of Waterloo, 1991.

[15]. R. H. Lipson and A. R. Hoy, *Mol. Phys.*, **68**, 1311 (1989).

[16]. K. P. Huber, G. Herzberg, **Constants of Diatomic Molecules**; Van Nostrand Reinhold: New York, 1979.

[17]. T. Moeller, B. Jordan, P. Gürtler, G. Zimmerer, D. Haaks, J. Le Calvé, M. C. Castex, *Chem. Phys.* **76**, 295 (1983).

[18]. A. E. Douglas and A. R. Hoy, *Can. J. Phys.* **53**, 1965 (1975).

[19]. K. Tsukiyama, Y. Kurematsu, M. Tsukakoshi, A. Misu, T. Kasuya, *Chem. Phys. Lett.* **152**, 523 (1988).

[20]. S. D. Peyerimhoff, R. J. Buenker, *Chem. Phys.* **57**, 279 (1981).

[21]. F. Grein, S. D. Peyerimhoff, R. J. Buenker, *Can. J. Phys.*, **62**, 1928 (1984).

[22]. L. C. Lee, M. Suto, K. Y. Tang, *J. Chem. Phys.* **84**, 5277, 1986.

[23]. A. A. Radzig and B. M. Smirnov, **Reference Data on Atoms, Molecules, and Ions**; *Springer Verlag Series in Chemical Physics* **31**; Springer Verlag: Berlin, 1985.

[24]. C. E. Moore, Atomic Energy Levels, *Natl. Bur. Stand. Circ. (U.S.) I*, No. **467**, 1971.

[25]. H. Lefebvre-Brion, A. Suzor-Weiner, *Comments At. Mol. Phys.* **29**, 305 (1994).

[26]. J. C. D. Brand and A. R. Hoy, *Appl. Spectrosc. Rev.*, **23**, 285 (1987).

Chapter 5

Discussion and Conclusions

The previous Chapters have demonstrated the usefulness of the newly built apparatus for spectroscopic studies. By using the tunable, coherent and monochromatic VUV light source together with supersonic jet and time-of-flight mass spectroscopic techniques, vibrationally and rotationally resolved single isotopomer excitation spectra of small molecules were obtained.

5.1 The $E0^+ \leftarrow X0^+$ transition of BrCl

In this work, vibrationally and rotationally resolved ion-pair spectra of the $E0^+ \leftarrow X0^+$ transition of BrCl have been obtained for the first time. Our results demonstrate that the combination of FWM sources, jet cooling, and TOF mass detection can greatly facilitate the understanding of complex VUV spectra.

Rotational constants have been derived for 30 vibrational bands of three of the four naturally occuring BrCl isotopomers. However, the most striking observation is the perturbed nature of the $E0^+$ ion-pair state. As an example, the (192, 0) band of $^{79}Br^{35}Cl$ is shown in Fig. 5.1 where the intensity distribution of the rotational lines is seen to vary significantly. In light of the low temperatures associated with supersonic expansions, the perturbations are most likely homogeneous in nature. It is instructive to compare the results here with what is known about the analog systems of Br_2 and Cl_2 because the lowest energy single-photon accessible ion-pair states of both homonuclear halogens are also perturbed.

The first tier ion-pair state of Br_2, $D0_u^+$, interacts primarily with the second tier ion-pair state $F0_u^+$ [1, 2]. The F $\leftarrow$ X transition is inherently weak because in the molecular orbital picture it involves a two electron jump [3]. Most of its intensity in fluorescence excitation was found to be derived from the perturbation. Rydberg/ion-pair

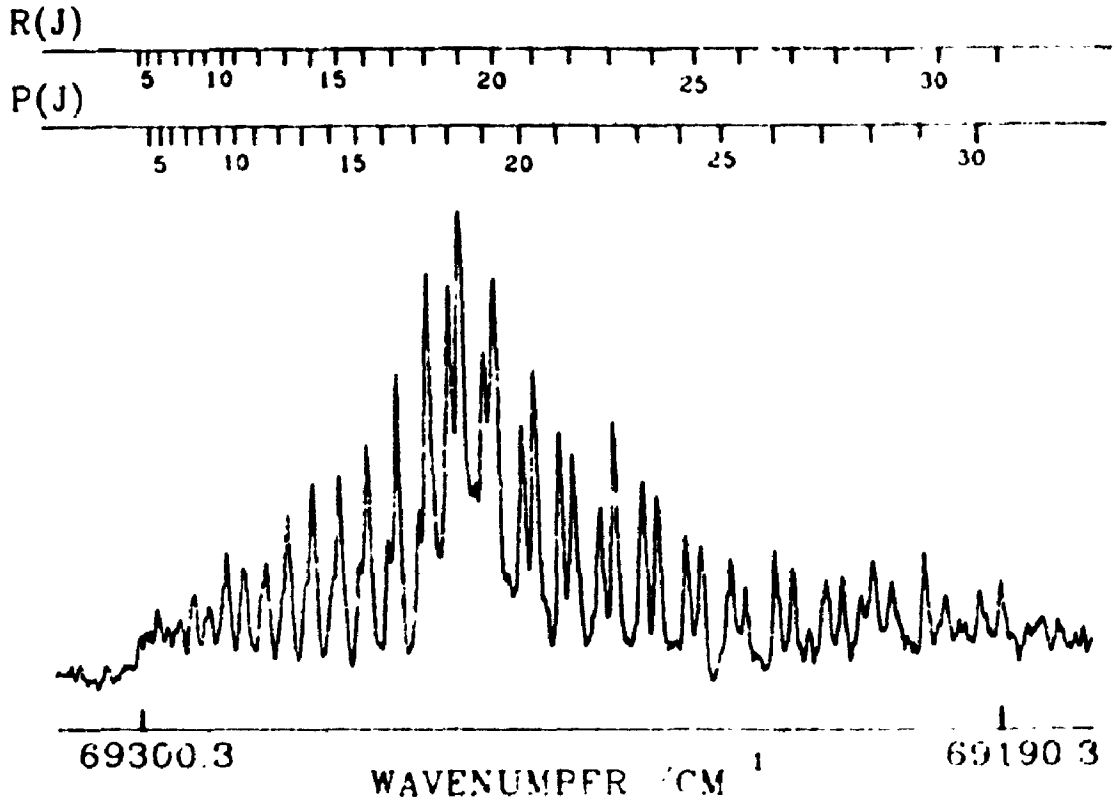

Fig. 5.1. A close-up of the vibrational band tentatively assigned to the (192, 0) member of the $E0^+ \leftarrow X0^+$ band system of $^{79}Br^{35}Cl$. The unusual intensity distribution is believed to be due to perturbations

state interactions are not significant because the former lie higher in energy.

The strongest VUV absorption for Cl_2 involves a third tier ion-pair state which dissociates to $Cl^+(^1D_g) + Cl^-(^1S_g)$. The spectrum is complex because of strong avoided crossings between the ion-pair state and the isoenergetic 4pπ Rydberg state. The resultant state, called $1\,^1\Sigma_u^+$, has a well-defined double well potential energy curve. Recent VUV laser spectra of blue-shaded vibrational bands localized in the short-bond length Rydberg minimum have confirmed this picture [4, 5]. Weaker unassigned red-shaded bands have also been observed in the laser spectra, which may be indicative of other ion-pair states in the same spectral vicinity.

While BrCl spectra exhibit some characteristics in common with those of the homonuclear species, the most prominent signature of interhalogen VUV excitation spectroscopy is an intensity modulation, which produces "dip resonances" as a result of ion-pair state/Rydberg state interactions [6, 7]. Some of the weaker features observed in this work which do not readily fit into the v'' = 0 progression may be hot bands or members of the $f0^+$ second tier ion-pair state [8]. The latter scenario could account for many of the perturbations.

The magnitude of the effective BrCl ion-pair state rotational constants and vibrational intervals are close to the predicted values, but do not change in a systematic way as a function of v'. Similar behavior was observed for Cl_2 [9]. There is no evidence, however, for blue-shaded Rydberg-like bands in our spectra and therefore, it is unlikely that the BrCl *E*-state potential curve has a double-minimum. Some of the weaker features were not rotationally analyzed. Nevertheless, their measured band heads were fitted into the v" = 0 progression. Although the vibrational numbering was established as best as possible, it should not be viewed as definitive due to the irregular nature of the band system.

There are five possible 0^+ valence states for each heteronuclear halogen which lie above their asymptotes and can interact with $E0^+$ [10, 11], while only the inner wing of the $B0_u^+$ valence state is available in the homonuclear case due to parity. This implies that a correct interpretation of the BrCl VUV spectrum may necessarily involve a

multistate deperturbation calculation. The spectroscopy of BrCl would certainly benefit from high quality *ab initio* calculations.

5.2 The $2^1\Sigma_u^+(v') \leftarrow X^1\Sigma_g^+(v''=0)$ transition of Cl_2

In this work, the first mass-resolved spectra of the $2^1\Sigma_u^+(v'= 1\text{-}3) \leftarrow X^1\Sigma_g^+(v'' = 0)$ transitions of Cl_2 were reported, where possible, the bands were rotationally analyzed. On the basis of measured vibrational isotope shifts, it is recommended that the currently accepted 2-state vibrational quantum numbering be increased by + 1.

An effort was made to locate the (0, 0) band of the 2 - X transition after the vibrational reassignment was done, but with no success in either LIF or atomic and molecular TOF detection. While it may be that the Franck-Condon factor for this transition is much smaller than those for the higher lying members of the (v', v'' = 0) progression, it seems more likely that there is a fast predissociation of v' = 0 by an additional electronic state which dissociates to ground state Cl atoms.

The rotational B'_v constants for $2^1\Sigma_u^+(v'= 1\text{-}3) \leftarrow X^1\Sigma_g^+(v'' = 0)$ transitions are smaller than that for the ground state, but do not decrease smoothly as v' increases from 1 to 3. In addition, as noted earlier, there are more vibrational bands observed between ~ 78000 and 80100 cm^{-1} than can be accounted for by transitions between the ground state and 2-state alone. It has been argued that the extra features belong to the $2^3\Pi_u(0_u^+) \leftarrow X^1\Sigma_g^+$ and/or $2^1\Pi_u(1_u) \leftarrow X^1\Sigma_g^+$ band systems [see Fig. 5.2, Ref. 12]

Transitions involving the $2^3\Pi_u(0_u^+)$ excited state (v' = 2 - 4) have now been recorded by Tsuchizawa *et al* [5] in fluorescence and mass-unresolved REMPI excitation using a VUV laser operating between 132.55 (~ 77012 cm^{-1}) and 129.85 nm (~ 75443 cm^{-1}). Each (v', 0) band was found to be undegraded, indicating an excited state equilibrium bond length very close to the ground state value.

The published $2^3\Pi_u(0_u^+)$ vibrational constants were used to predict transition wavenumbers at higher energies, but it proved difficult to make convincing state

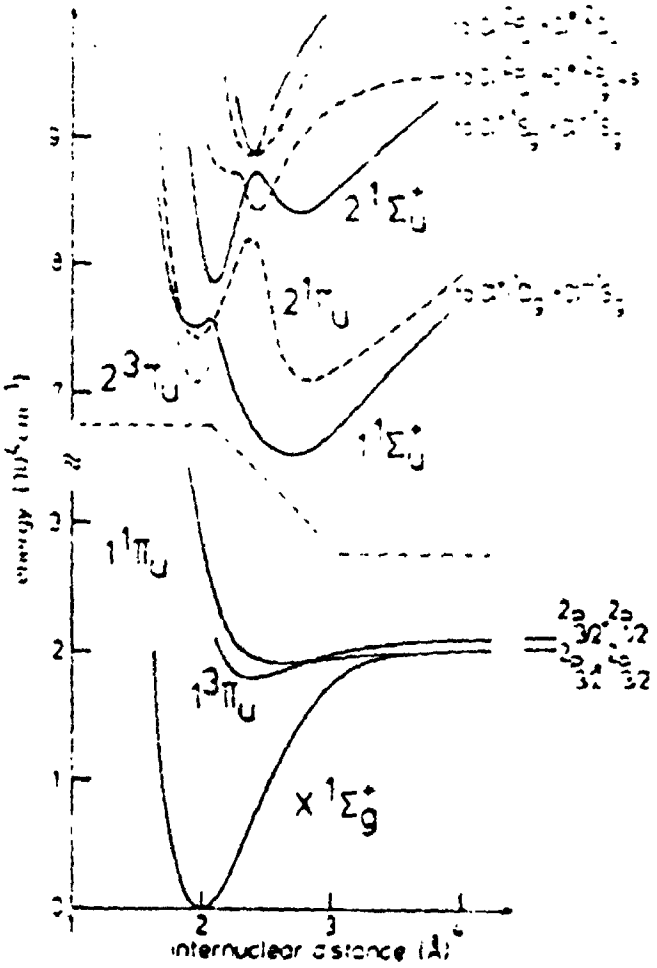

Fig. 5.2. Potential curves of Cl_2 (not complete). Lower part: experimental curves, upper part: ab initio calculations [12, 13], and dotted curves: diabatic potentials

assignments for the extra bands in our spectra on that basis. The problem may be related to the shape of the $2^3\Pi_u(0_u^+)$ potential energy curve. Like $2^1\Sigma_u^+$, the adiabatic $2^3\Pi_u(0_u^+)$ state is predicted to have a double minimum due to an avoided crossing between a 4pσ Rydberg state and an ion-pair state dissociating to $Cl^+(^3P_g) + Cl^-(^1S_g)$ [13, 14]. If the higher lying v'-levels have term energies greater than the barrier connecting the two diabatic potential energy curves, then the $2^3\Pi_u(0_u^+)$ vibrational wave functions will become delocalized in the ion-pair portion of the potential, leading to red-shaded bands as observed. However, as documented for the lower energy $1^1\Sigma_u^+ \leftarrow X^1\Sigma_g^+$ transition, vibrational spacings, particularly in the region of the avoided crossing, can be erratic [4, 5, 12, 15-16].

Although VUV transitions involving the $2^1\Pi_u(1_u)$ spin-orbit component (0_u^+ - 1_u spin-orbit splitting ~ 725 cm^{-1}, Ref. 17) cannot be ruled out, their intensities above the potential hump should be significantly lower than those involving $2^3\Pi_u(0_u^+)$ because of a strong $\Delta\Omega = 0$ "propensity" rule governing valence to ion-pair state transitions [8, 18]. The $2^3\Pi_u(2_u)$ component, of course, could not be accessed in our experiment due to single-photon selection rules.

Blue-shaded (v' = 0-4, 0) bands of the $2^1\Pi_u \leftarrow X^1\Sigma_g^+$ transition have been recorded in absorption between 74443 and 76897 cm^{-1} [12]. The adiabatic $2^1\Pi_u$ state is also predicted to have a double minimum, this time due to an avoided crossing between a 4pσ Rydberg state and a third tier ion-pair state dissociating to $Cl^+(^1D_g) + Cl^-(^1S_g)$. In the energy region under investigation, the potential is expected to be predominantly Rydberg-like in character, and therefore, the $\Delta\Omega = 0$ rule should not be that rigorous [13, 14]. Since none of the unassigned bands in this work are blue-shaded, and the rotational constants obtained for these bands are smaller compared to that for the ground state, it seems unlikely that they belong to the $2^1\Pi_u \leftarrow X^1\Sigma_g^+$ system. Moreover, *ab initio* calculations predict that $2^1\Pi_u$ couples only with the $2^3\Pi_u$ state through the spin-orbit

interaction [19]. If $2^1\Pi_u$ levels are being excited in our experiment, they cannot be responsible alone for the irregularities in the $2^1\Sigma_u^+$ spacings and intensities.

Gerade superexcited states appear to play a significant role in determining the rotational line intensity distribution of the molecular (1 + 1) REMPI-TOF spectra. As discussed above, single-photon synchrotron spectroscopy has clearly located a long-lived ungerade superexcited state of Cl_2 in the region just above the first ionization limit [20]. Cl_2 levels of a similar nature and parity have also been accessed via a (2 + 1) REMPI excitation through the $2^1\Pi_r$ Rydberg state [21, 22]. Although that excitation spectrum appeared completely regular with no evidence of strong adiabatic interactions, photoelectron spectra originating from the $2^1\Pi_g$ showed a strong deviation from normal Franck-Condon behavior which could only be rationalized by invoking superexcited states.

In general, superexcited states probed above their dissociation limits can competitively decay either through fluorescence, through autoionization, or by dissociation [23]. In the example above, the autoionization channel is dominant when REMPI excitation takes place through low v'-levels of the $2^1\Pi_g$ state while dissociation starts to compete at higher energies. The signature for the dissociative channel was strong photoelectron signals originating from electronically excited Cl atoms.

REMPI-photoelectron experiments have also been carried using the $2^1\Sigma_u^+$ state as the intermediate level [17, 21]. Again, a complicated photoelectron spectrum was obtained. In this case, however, the complexity was attributed to the mixed Rydberg-valence character of the 2-state. Removal of an electron from the 2-state diabatic Rydberg component produces Cl_2^+ in its $X^2\Pi_g$ ground state, while the diabatic ion-pair state is built upon an excited $^2\Sigma_g^+$ ion core. The presence of these ionic states in the photoelectron spectrum was ascribed to simultaneous (3 + 1) and (3 + 2) ionization. In view of the present results, superexcited states of both parities may also need to be considered to fully understand the photoelectron data. (3 + 1) REMPI could terminate on a gerade superexcited state near 96 nm while a (3 + 2) excitation could excite an ungerade superexcited state near 77 nm. The fact that no atomic signals were evident in the 2-state

photoelectron spectrum may simply mean that superexcited states, if accessed, were excited below their dissociation limits where autoionization dominates. Recently, a dispersive photoelectron spectrometer was added to the system, replacing the soalr-blind photomultiplier tube which was removed. It is hoped that our understanding of Cl_2 spectroscopy will be enhanced when experiments along this line are done in the near future.

5.3 Other Future Work

The combination of resonantly enhanced multiphoton ionization and time-of-flight mass spectrometry can be a useful analytical tool for detection of trace quantities of organic substances. This technique can allow a substance-selective or even an isomer-selective ionization of organic compounds, from complex matrices. Using this new approach, a fast and effective analysis of environmentally harmful pollutants such as chlorinated aromatic compounds can be performed which is not currently possible with conventional methods yet [24]. In general, a reflectron TOF mass spectrometer can be used to achieve a much higher resolution. It will be interesting and challenging to develop analytical and environmental applications with proper modifications of the existing apparatus.

5.4 References

[1]. R. H. Lipson, A. R. Hoy, and M. J. Flood, *Chem. Phys. Lett.* **149**, 155 (1988).

[2]. R. H. Lipson and A. R. Hoy, *J. Mol. Spectrosc.* **134**, 183 (1989).

[3]. R. S. Mulliken, *J. Chem. Phys.*, **55**, 288 (1971).

[4]. K. Yamanouchi, T. Tsuchizawa, J. Miyawaki, and S. Tsuchiya, *Chem. Phys. Lett.*, **156**, 301 (1989).

[5]. T. Tsuchizawa, K. Yamanouchi, and S. Tsuchiya, *J. Chem. Phys.*, **93**, 111 (1990).

[6]. A. J. Yencha, R. J. Donovan, A. Hopkirk, and D. Shaw, *J. Phys. Chem.*, **92**, 5523 (1988).

[7]. K. P. Lawley, E. A. Kerr, R. J. Donovan, A. Hopkirk, D. Shaw, and A. J. Yencha, *J. Phys. Chem.*, **94**, 6201 (1990).

[8]. J. C. D. Brand and A. R. Hoy, *Appl. Spectrosc. Rev.*, **23**, 285 (1987).

[9]. A. E. Douglas, *Can. J. Phys.*, **59**, 835 (1981).

[10]. R. H. Lipson and A. R. Hoy, *J. Chem. Phys.*, **90**, 6821 (1989).

[11]. R. H. Lipson and A. R. Hoy, *Mol. Phys.*, **68**, 1311 (1989).

[12]. T. Moeller, B. Jordan, P. Gürtler, G. Zimmerer, D. Haaks, J. LeCalvé, and M. C. Castex, *Chem. Phys.*, **76**, 295 (1983).

[13]. S. D. Peyerimhoff, R. J. Buenker, *Chem. Phys.*, **57**, 279 (1981).

[14]. T. Moeller, B. Jordan, P. Gürtler, D. Haaks, J. LeCalvé, and M. C. Castex, *Spectral Line Shapes* **2**, 597 (1983).

[15]. P. Wang, I. V. Okuda, S. S. Dimov, and R. H. Lipson, *Chem. Phys. Lett.*, **229**, 370 (1994).

[16]. J. Wörmer, T. Möller, J. Stapelfeldt, G. Zimmerer, D. Haaks, S. Kampf, J. LeCalvé, and M. C. Castex, *Z. Physik D* **7**, 383 (1988).

[17]. B. G. Koenders, D. M. Wieringa, K. E. Drabe, C. A. de Lange, *Chem. Phys.*, **118**, 113 (1987).

[18]. R. N. Zare and D. R. Herschbach, *J. Mol. Spectrosc.*, **15**, 462 (1965).

[19]. F. Grein, S. D. Peyerimhoff, R. J. Buenker, *Can. J. Phys.*, **62**, 1928 (1984).

[20]. L. C. Lee, M. Suto, K. Y. Tang, *J. Chem. Phys.*, **84**, 5277 (1986).

[21]. B. G. Koenders, C. A. de Lange, *Comments At. Mol. Phys.*, **24**, 119 (1990), and references within.

[22]. B. G. Koenders, S. M. Koeckhoven, G. J. Kuik, K. E. Drabe, C. A. de Lange, *J. Chem. Phys.*, **91**, 6042 (1989).

[23]. H. Lefebvre-Brion, A. Suzor-Weiner, *Comments At. Mol. Phys.*, **29**, 305 (1994).

[24]. R. Zimmermann, U. Boesl, C. Weickhardt, D. Lenoir, K.W. Schramm, E.W. Schlag, *Chemosphere*, **29**, 1877 (1994).